



RTK and PPP with Galileo and GPS

Nataliya Mishukova

Supervised by Dr.-Ing. Patrick Henkel

December 17, 2013

Submitted for the degree *Master of Science*
at the faculty *Bau Geo Umwelt*
at *Technische Universität München (TUM)*

Email: nataliya.mishukova@tum.de

Layout by L^AT_EX 2_ε

Declaration

This thesis is a presentation of my original research work. Wherever contributions of others are involved, every effort is made to indicate this clearly, with due reference to the literature, and acknowledgment of collaborative research and discussions.

Nataliya Mishukova

Munich, December 17th 2013

Acknowledgments

First and foremost I would like to thank my supervisor, Dr. Patrick Henkel, for the opportunity to do my Master's thesis under his supervision, for sharing the knowledge and encouraging me to come up with innovative solutions to the problems as they arose. Working with him allowed me to learn about the state of the art in satellite navigation from a brilliant mind, that I will be always grateful for.

I would like to thank Prof. Christoph Günther for being the one to introduce me to the satellite navigation during the first semester of the ESPACE Master's Program. His course gave me the inspiration to get more insight into this fascinating area and ultimately decide to work further in it after the graduation.

I would like to thank Juan Manuel Cardenas for the support and help throughout the thesis. His hard work was a good example for me.

I am grateful to Zhibo Wen for his considerable help with precise satellite orbit and clock determination, as well as for his advices and our technical discussions.

I am also thankful to Jean, Juan Carlos, Philipp and Naoya from ANAVS for the pleasure of working together. Their dedication and optimism was a huge support for me during the period of work on this thesis.

I would like to thank Prof. Reinel Rummel, Prof. Urs Hugentobler and all academic staff of ESPACE Master's Program for the hard work they do to manage and develop an international high-quality study program.

Finally, I would like to thank my family and Edgars Locmelis for all the support and care.

Abstract

Global Navigation Satellite Systems (GNSS) have revolutionized many aspects of science and every day life and allowed to realize applications which were unfeasible a few years ago. However, the accuracy of the positioning with GNSS is limited by uncertainties in the satellite code and phase biases, and code and phase multipath. The European GNSS Galileo offers dedicated signals to overcome the multipath shortcoming. Exploiting its full capability will improve the reliability of integer ambiguity resolution and provide the increased GNSS positioning accuracies. It will be demonstrated in this thesis by analyzing the reliability of widelane integer ambiguity resolution with Galileo in a static short-baseline relative positioning, as well as investigating the stability of the float ambiguity estimates in Real-Time Kinematic (RTK) positioning with 25 km kinematic baseline. In addition, the GPS and Galileo fixed phase residuals of Precise Point Positioning (PPP) for a kinematic receiver are compared. Moreover, a new method for the joint subset optimization and integer least-squares estimation of carrier phase cycle slips with the improved integer search is developed.

Nowadays, using the differential GPS techniques that employ a network of reference receivers, sub-meter or even centimeter-level positioning accuracy can be reached. When the network is not dense enough for the accuracy desired, the method of Virtual Reference Station (VRS) is used. In currently existing networks high-cost receivers are used, which poses a great obstacle in obtaining higher accuracies for civilian purposes and survey grade applications at affordable prices. This thesis will focus on enhancing the precision and reliability of GNSS based absolute user receiver position estimation using a network of low-cost GNSS receivers. A Virtual Reference Station method is developed for the particularities of such receivers. We also propose a PPP solution, which determines the absolute receiver position, ionospheric slant delays, ambiguities and biases from single frequency satellite-satellite single-difference measurements. As the estimation problem is ill-conditioned, we additionally include ionospheric a priori information to improve the conditioning and convergence of the estimates. The a priori information is a Gaussian distribution and consists of a mean value (Klobuchar, EGNOS) and a variance. The GNSS measurements and ionospheric a priori information are combined in a Maximum A Posteriori (MAP) estimation of the PPP solution. Thereby, we find an optimum trade-off between minimizing the measurement residuals and minimizing the ionospheric residuals.

Contents

Declaration	i
1. Introduction	1
1.1 Motivation and problem statement	1
1.2 Methodology	1
2. Fundamentals	3
2.1 Code and phase measurement models	3
2.2 Single-frequency linear combinations of code and phase measurements	4
2.3 Multi-frequency linear combinations of code and phase measurements	6
3. Precise positioning with Galileo	10
3.1 The European Global Navigation Satellite System Galileo	10
3.2 Galileo signals	12
3.3 Static short-baseline test	13
3.4 Kinematic long-baseline test	20
3.4.1 Long-range RTK with 25 km kinematic baseline	20
3.4.2 Precise Point Positioning	26
3.5 Joint subset optimization and integer least-squares estimation	28
4. Absolute positioning with a system of low-cost GPS receivers	35
4.1 The Virtual Reference Station method	35
4.2 Least-squares float solution of absolute position of a reference receiver	40
4.2.1 Modeling of tropospheric delay using the MOPS model	41
4.2.2 Estimation of a receiver position, carrier phase ambiguities and residual ionospheric delays	44
4.3 Corrections for single-difference code and phase measurements	58
4.4 Estimation of absolute position of a user receiver	63
5. Conclusions	66
List of Abbreviations	67

List of Figures	69
List of Tables	70
Bibliography	72

1. Introduction

1.1 Motivation and problem statement

The European GNSS Galileo offers signals with larger signal bandwidths than GPS and special modulation schemes to overcome the multipath, which is a main limiting factor for positioning accuracy in the urban environments. For example, the Alternate BOC (AltBOC) modulated E5 signal has a bandwidth of more than 50 MHz [1]. The impact of multipath on this signal is the lowest ever observed compared to all other available GNSS signals. In addition, it features a code tracking error five times lower than the BPSK(10) modulated GPS L5 signal [2]. The new signals and additional frequencies will improve the reliability of integer ambiguity resolution and provide higher positioning accuracies. With currently 4 Galileo satellites available, the estimation of the Galileo system capability is possible.

Nowadays, reliable and precise absolute positioning is possible with high-cost geodetic GNSS receivers, while low-cost systems mainly demonstrate a moderate absolute positioning performance. The carrier smoothing technique is a popular approach to reduce the code noise and multipath using low noise phase measurements without the need of an integer ambiguity resolution. Differential GPS techniques, that use a reference station with known coordinates to provide the sum of errors in the form of correction at the user receiver, allow to mitigate the atmospheric and orbital errors. The use of a regional network of reference stations instead of a single station allows modeling of the systematic errors. Though dense enough for good Differential GPS (DGPS), some national networks cannot provide density sufficient for precise RTK, especially in the periods of high atmospheric disturbance. The method of Virtual Reference Station (VRS) allows performing RTK positioning in reference station networks with distances as long as 40 km to the next reference station while providing the performance of short baseline positioning [3]. However, the method employs high-cost geodetic receivers. The motivation for this master's thesis is to develop the Virtual Reference Station concept for the network of low-cost receivers.

1.2 Methodology

Most of the algorithms for this master thesis were programmed in MATLAB and tested in various measurement campaigns. GPS and Galileo measurements for precise positioning with Galileo were collected using two geodetic NovAtel OEM628™ triple-frequency L-band GNSS receivers,

as well as Javad GrAnt and Novatel GPS-703-GGG triple-frequency Pinwheel™ high performance GNSS antennas. GPS measurements for precise absolute positioning with low-cost receivers were collected with two u-blox LEA 6T receivers as well as compact patch antennas from u-blox and Trimble. Some of the algorithms have been recently integrated into the Position and Attitude Determination (PAD) system of Advanced Navigation Solutions (ANAVS) GmbH.

The second chapter of the thesis provides the fundamentals necessary to proceed to precise positioning with geodetic and low-cost GNSS receivers, such as code and phase measurements models, as well as single-frequency and multi-frequency code and phase combinations used.

The third chapter of this thesis shows the results of the precise absolute and relative positioning with Galileo. The positioning algorithms applied to the measurements collected within the two different test campaigns are described. In addition, the benefits of Galileo system as well as its signal innovations are described. Finally, a new method for joint subset optimization and integer least-squares estimation in case of cycle slips is proposed.

The fourth chapter introduces a Virtual Reference Station (VRS) method and describes its adaptation for a system of low-cost single-frequency GNSS receivers. The method for precise absolute positioning of the reference station is described, which includes the estimation of position, ambiguities and soft-constrained residual combined ionospheric delays. Moreover, the interpolation method for the sum of errors derived from the raw single-difference code and phase measurements of reference stations is suggested. Final positioning accuracy on a decimeter level is expected.

The fifth chapter summarizes all the main concepts and results presented in the thesis, as well as provides the suggestions for the further development of these concepts.

2. Fundamentals

2.1 Code and phase measurement models

Absolute position determination with any GNSS is based on estimating signal propagation times from satellites to receivers. They are measured relative to a receiver generated code replica during the code tracking process [4]. The corresponding pseudoranges, which are equal to true ranges plus errors, are determined by multiplication of propagation times by the speed of light. Pseudoranges are modeled as measured at the receiver r from satellite k on any frequency m as described by Henkel [5]:

$$\begin{aligned} \rho_{r,m}^k(t_n) = & \|\vec{x}_r(t_n) + \Delta\vec{x}_{\text{ET},r}(t_n) - \vec{x}^k(t_n - \Delta t_n) - \Delta\vec{x}^k(t_n)\| + c(\delta\tau_r(t_n) - \delta\tau^k(t_n - \Delta t_n)) \\ & + m_{\text{T}}(\theta_r^k(t_n))T_{z,r}(t_n) + q_{1m}^2 I_{1,r}^k(t_n) + b_{r,m} + b_m^k \\ & + \Delta\rho_{\text{MP},r,m}^k(t_n) + \eta_{r,m}^k(t_n) \end{aligned} \quad (2.1)$$

with the time of signal reception t_n , the signal travel time Δt_n , the receiver position \vec{x}_r , the receiver position error due to the solid Earth tides $\Delta\vec{x}_{\text{ET},r}$, the satellite position \vec{x}^k , the satellite position error $\Delta\vec{x}^k$, the speed of light c in vacuum, the receiver clock offset $\delta\tau_r$, the satellite clock offset $\delta\tau^k$, the tropospheric zenith delay $T_{z,r}$ equal for all satellites, its corresponding mapping function $m_{\text{T}}(\theta_r^k)$ as a function of satellite elevation angle θ_r^k , the ionospheric slant delay $I_{1,r}^k$ of the first order on frequency f_1 , the ratio of carrier frequencies $q_{1m}^2 = \frac{f_1^2}{f_m^2}$, the receiver code bias $b_{r,m}$, the satellite code bias b_m^k , the code multipath error $\Delta\rho_{\text{MP},r,m}^k$ and the receiver code noise $\eta_{r,m}^k$. The first term denotes the true range r_r^k between satellite and receiver.

The tides generated by the Sun and Moon deform the shape of the Earth, causing so-called solid Earth tides. The tidal deformation can be divided into two parts: a periodic and a permanent (time-independent) part. The permanent tide is a function of observer's latitude only. The periodic radial and horizontal site displacements caused by tides of spherical harmonic degree and order (n, m) are characterized by the Love number h_{nm} and the Shida number l_{nm} that reflect the non-rigidity of the Earth. The effective values of these numbers weakly depend on receiver latitude and tidal frequency and need to be taken into account when a positioning accuracy of 1 mm is desired. However, only second degree tide and height correction terms are necessary for 5 mm precision [6].

Apart from code tracking, every GNSS receiver provides the second measurement type, achieved by carrier phase tracking. The received carrier phase is measured relative to the phase of a reference sinusoidal signal generated by the receiver clock. Using these measurements, a substantially higher positioning accuracy can be achieved. However, carrier phase is periodic, which results in the initial integer phase ambiguity not measured by the receiver. In order to benefit from the low noise level of the carrier phase measurements, these ambiguities has to be resolved. Carrier phase can be modeled similarly to pseudorange, i.e.[5]:

$$\begin{aligned} \lambda_m \varphi_{r,m}^k(t_n) &= \|\vec{x}_r(t_n) + \Delta\vec{x}_{\text{ET},r}(t_n) - \vec{x}^k(t_n - \Delta t_n) - \Delta\vec{x}^k(t_n)\| + c(\delta\tau_r(t_n) - \delta\tau^k(t_n - \Delta t_n)) \\ &\quad + m_{\text{T}}(\theta_r^k(t_n))T_{z,r}(t_n) - q_{1m}^2 I_{1,r}^k(t_n) + \lambda_m N_{u,m}^k + \Delta\varphi_{\text{PW},r}^k(t_n) + \Delta\varphi_{\text{PCO},r}^k \\ &\quad + \Delta\varphi_{\text{PCV},r}^k(t_n) + \beta_{r,m} + \beta_m^k + \Delta\varphi_{\text{MP},r,m}^k(t_n) + \varepsilon_{r,m}^k(t_n) \end{aligned} \quad (2.2)$$

with the wavelength of the m -th carrier signal λ_m , the carrier phase integer ambiguity $N_{r,m}^k$, the phase wind-up error $\Delta\varphi_{\text{PW},r}^k$, the receiver antenna phase center offset error $\Delta\varphi_{\text{PCO},r}^k$, the receiver antenna phase center variation error $\Delta\varphi_{\text{PCV},r}^k$, the receiver phase bias $\beta_{r,m}$, the satellite phase bias β_m^k and the phase noise $\varepsilon_{r,m}^k$ as additional terms. The ionospheric slant delay $I_{1,r}^k$ has to be subtracted from the true range instead of being added as for pseudorange.

2.2 Single-frequency linear combinations of code and phase measurements

Linear combinations of measurements are widely used in absolute and relative positioning to improve the reliability of integer ambiguity resolution, as they allow to reduce or eliminate range error terms. The simplest linear combinations are single-frequency linear combinations such as between-receiver and between-satellite differences of code and phase measurements.

The between-satellite single-difference (SD) code measurements on the frequency m are formed by taking a difference of the measurements of (2.1) at the receiver r from the reference satellite k , which is typically the satellite with highest elevation, and any other satellite l at the same epoch [4]:

$$\rho_{r,m}^{k,l} = \rho_{r,m}^k - \rho_{r,m}^l \quad (2.3)$$

$$\begin{aligned} &= (r_r^k - r_r^l) - c(\delta\tau^k - \delta\tau^l) + (m_{\text{T}}(\theta_r^k) - m_{\text{T}}(\theta_r^l))T_{z,r} + q_{1m}^2 (I_{1,r}^k - I_{1,r}^l) \\ &\quad + (b_m^k - b_m^l) + (\eta_{r,m}^k - \eta_{r,m}^l) \end{aligned} \quad (2.4)$$

where code biases include the error due to solid Earth tides and code noise includes multipath.

Single-difference carrier phase measurements are given by [4]:

$$\lambda_m \varphi_{r,m}^{k,l} = \lambda_m (\varphi_{r,m}^k - \varphi_{r,m}^l) \quad (2.5)$$

$$\begin{aligned} &= (r_r^k - r_r^l) - c(\delta\tau^k - \delta\tau^l) + (m_T(\theta_r^k) - m_T(\theta_r^l))T_{z,r} - q_{1m}^2(I_{1,r}^k - I_{1,r}^l) \\ &\quad + \lambda_m(N_{r,m}^k - N_{r,m}^l) + (\beta_m^k - \beta_m^l) + (\varepsilon_{r,m}^k - \varepsilon_{r,m}^l) \end{aligned} \quad (2.6)$$

where satellite phase biases include the errors due to solid Earth tides, as well as phase wind-up, antenna phase center offset and variation errors, and phase noise includes multipath. Under assumption that the measurements are taken at the same epoch, receiver clock offsets as well as receiver biases are eliminated by taking single difference of the measurements. On the other hand, the noise of single-difference measurements is increased by a factor of $\sqrt{2}$ with respect to the noise of individual measurements [7]. In the similar manner between-receiver single-difference code and phase measurements can be formed from the measurements of two receivers and any satellite in order to eliminate satellite clock offsets and biases.

We simplify the notation by writing between satellite single-difference measurements as $(\cdot)^{kl}$, i.e.

$$\rho_{r,m}^{kl} = r_r^{kl} - c\delta\tau^{kl} + q_{1m}^2 I_{1,r}^{kl} + T_r^{kl} + b_m^{kl} + \eta_{r,m}^{kl} \quad (2.7)$$

$$\lambda_m \varphi_{r,m}^{kl} = r_r^{kl} - c\delta\tau^{kl} - q_{1m}^2 I_{1,r}^{kl} + T_r^{kl} + \lambda_m N_{r,m}^{kl} + \beta_{r,m}^{kl} + \varepsilon_{r,m}^{kl} \quad (2.8)$$

In order to eliminate further errors common to two receivers, double-difference (DD) measurements from reference satellite k and any other satellite l at the user receiver u and a reference receiver r can be computed from Eq. (2.7) and Eq. (2.8) as follows [4]:

$$\rho_{ur,m}^{kl} = \rho_{u,m}^{kl} - \rho_{r,m}^{kl} \quad (2.9)$$

$$= r_{ur}^{kl} + q_{1m}^2 I_{1,ur}^{kl} + T_{ur}^{kl} + \eta_{ur,m}^{kl} \quad (2.10)$$

$$\lambda_m \varphi_{ur,m}^{kl} = \lambda_m (\varphi_{u,m}^{kl} - \varphi_{r,m}^{kl}) \quad (2.11)$$

$$= r_{ur}^{kl} - q_{1m}^2 I_{1,ur}^{kl} + T_{ur}^{kl} + \lambda_m N_{ur,m}^{kl} + \varepsilon_{ur,m}^{kl} \quad (2.12)$$

Formation of double-difference phase measurements simplifies integer ambiguity resolution, as receiver and satellite phase biases are canceled out and atmospheric errors are reduced. On the other hand, the noise of double-difference measurements is increased by a factor of 2 with respect to the noise of individual measurements [7].

2.3 Multi-frequency linear combinations of code and phase measurements

Multi-frequency linear combinations are formed from the individual, as well as single-difference and double-difference code and phase measurements on several frequencies taken at the same epoch. They allow to scale or eliminate certain pseudorange constituents, simplify integer ambiguity resolution by increasing the wavelength or reduce the noise of unambiguous code measurements.

We simplify the observation equations (2.1) and (2.2) by denoting all non-dispersive terms as ρ' :

$$\rho' = r_r^k - c(\delta\tau_r - \delta\tau^k) + T_r^k \quad (2.13)$$

and the sum of satellite and receiver biases is denoted as one term. Code measurements ρ_r^k and carrier phase measurements φ_r^k at the receiver r from any satellite k are linearly combined using coefficients α_1 and α_2 to create code-only and phase-only linear combinations.

The dispersive behavior of ionospheric delay proportional to the inverse of the square of carrier frequency $\frac{1}{f_m^2}$ enables its elimination (to the first order) by ionosphere-free (IF) linear combinations. Assuming that the measurements at receiver r from any satellite k on two frequencies f_1 and f_2 are given, the combination can be formed using the following coefficients α_1 and α_2 [5]:

$$\alpha_1 = \frac{f_1^2}{f_1^2 - f_2^2} \quad \alpha_2 = -\frac{f_2^2}{f_1^2 - f_2^2} \quad (2.14)$$

They are obtained from geometry preserving ($\alpha_1 + \alpha_2 = 1$) and ionosphere free ($\alpha_1 + q_{12}^2 \alpha_2 = 0$) constraints. For the code measurements of Eq. (2.1) ionosphere-free combination is given by:

$$\rho_{r,\text{IF}}^k = \alpha_1 \rho_{r,1}^k + \alpha_2 \rho_{r,2}^k \quad (2.15)$$

$$\begin{aligned} &= (\alpha_1 + \alpha_2)\rho' + \alpha_1 b_{r,1}^k + \alpha_2 b_{r,2}^k + \alpha_1 \eta_{r,1}^k + \alpha_2 \eta_{r,2}^k \\ &= \rho' + \alpha_1 b_{r,1}^k + \alpha_2 b_{r,2}^k + \alpha_1 \eta_{r,1}^k + \alpha_2 \eta_{r,2}^k \end{aligned} \quad (2.16)$$

For the phase measurements of Eq. (2.2) we obtain:

$$\lambda \varphi_{r,\text{IF}}^k = \alpha_1 \lambda_1 \varphi_{r,1}^k + \alpha_2 \lambda_2 \varphi_{r,2}^k \quad (2.17)$$

$$\begin{aligned} &= \rho' + \alpha_1 \left(\frac{c}{f_1} N_{r,1}^k + \varepsilon_{r,1}^k \right) + \alpha_2 \left(\frac{c}{f_2} N_{r,2}^k + \varepsilon_{r,2}^k \right) + \alpha_1 \beta_{r,1}^k + \alpha_2 \beta_{r,2}^k \\ &= \rho' + \frac{c}{f_1^2 - f_2^2} (f_1 N_{r,1}^k - f_2 N_{r,2}^k) + \alpha_1 \beta_{r,1}^k + \alpha_2 \beta_{r,2}^k + \alpha_1 \varepsilon_{r,1}^k + \alpha_2 \varepsilon_{r,2}^k \end{aligned} \quad (2.18)$$

The combination contains geometry, clock offsets, tropospheric delay, receiver and satellite biases, as well as ambiguities for phase. The noise of linear combination is amplified with respect to the noise of individual measurements.

The widelane (WL) linear combinations are particularly suitable for integer ambiguity resolution and search for small cycle slips, as it creates a signal with significantly longer wavelength as follows [4]:

$$\lambda_{\text{WL}}\varphi_r^k = \frac{f_1}{f_1 - f_2}\lambda_1\varphi_{r,1}^k - \frac{f_2}{f_1 - f_2}\lambda_2\varphi_{r,2}^k \quad (2.19)$$

$$= \rho' + \frac{f_1}{f_2}I_{1,r}^k + \frac{c}{f_1 - f_2}(N_{r,1}^k - N_{r,2}^k) + \frac{f_1\beta_{r,1}^k - f_2\beta_{r,2}^k}{f_1 - f_2} + \frac{f_1\varepsilon_{r,1}^k - f_2\varepsilon_{r,2}^k}{f_1 - f_2} \quad (2.20)$$

The large wavelength $\lambda_{\text{WL}} = c/(f_1 - f_2)$ reduces uncertainty in integer ambiguity resolution, but only in case the noise amplification of individual measurements is less than the increase of the wavelength.

The narrowlane (NL) linear combinations allow to reduce the phase measurement noise and are given by:

$$\varphi_{r,\text{NL}}^k = \frac{f_1}{f_1 + f_2}\varphi_{r,1}^k + \frac{f_2}{f_1 + f_2}\varphi_{r,2}^k \quad (2.21)$$

$$= \rho' - \frac{f_1}{f_2}I_{1,r}^k + \frac{f_1N_{r,1}^k + f_2N_{r,2}^k}{f_1 + f_2} + \frac{f_1\beta_{r,1}^k + f_2\beta_{r,2}^k}{f_1 + f_2} + \frac{f_1\varepsilon_{r,1}^k + f_2\varepsilon_{r,2}^k}{f_1 + f_2} \quad (2.22)$$

Both widelane and narrowlane combinations contain geometry, ionospheric and tropospheric delays, clock offsets, receiver and satellite biases, as well as ambiguities for phase.

Except for code-only and phase-only combinations, code-carrier linear combinations can be formed. The dual-frequency Melbourne-Wübbena linear combination, formed as the difference between the dual-frequency carrier phase widelane combination and dual-frequency code combination with coefficients according to the narrowlane (+1,+1) combination, is given by ([5], [8] and [9]):

$$\lambda_{\text{WL}}\varphi_{r,\text{MW}}^k = \left(\frac{f_1}{f_1 - f_2}\lambda_1\varphi_{r,1}^k - \frac{f_2}{f_1 - f_2}\lambda_2\varphi_{r,2}^k \right) - \left(\frac{f_1}{f_1 + f_2}\rho_{r,1}^k + \frac{f_2}{f_1 + f_2}\rho_{r,2}^k \right) \quad (2.23)$$

$$= \frac{c}{f_1 - f_2}(N_{r,1}^k - N_{r,2}^k) + \frac{f_1\varepsilon_{r,1}^k - f_2\varepsilon_{r,2}^k}{f_1 - f_2} - \frac{f_1\eta_{r,1}^k + f_2\eta_{r,2}^k}{f_1 + f_2} \quad (2.24)$$

It posses the large wavelength of widelane combination and eliminates non-dispersive part of the geometry and dispersive ionospheric delay. The widelane ambiguities, as well as satellite and receiver biases remain. The trade-off is the large noise that is given by the code measurements noise.

Henkel and Günther derived in [10] a group of multi-frequency code-carrier linear combinations which allow an arbitrary scaling of the geometry, an arbitrary scaling of the ionospheric delay and any preferred wavelength. The noise level of the combinations is of a few centimeters. Code ρ_r^k and carrier phase φ_r^k measurements at the user receiver r from any satellite k on multiple frequen-

cies M are linearly combined with the phase weight α_m and the code weight γ_m as follows:

$$\begin{aligned}
 \sum_{m=0}^M (\alpha_m \lambda_m \varphi_{r,m}^k + \gamma_m \rho_{r,m}^k) = & \left(\sum_{m=0}^M (\alpha_m + \gamma_m) \right) \rho' \\
 & - \left(\sum_{m=0}^M (\alpha_m - \gamma_m) q_{1m}^2 \right) I_{1,r}^k - \left(\sum_{m=0}^M \left(\frac{1}{2} \alpha_m - \gamma_m \right) q_{1m}^3 \right) I_{1,r}^{''k} \\
 & + \left(\sum_{m=0}^M (\alpha_m \lambda_m N_{r,m}^k) \right) + \left(\sum_{m=0}^M (\alpha_m (\beta_{r,m} + \beta_m^k) + \gamma_m (b_{r,m} + b_m^k)) \right) \\
 & + \left(\sum_{m=0}^M (\alpha_m \varepsilon_{r,m}^k + \gamma_m \eta_{r,m}^k) \right) \tag{2.25}
 \end{aligned}$$

where the ionospheric delay on the first frequency $I_{1,r}^k$ is presented as ionospheric delay $I_{1,r}^k$ of the first order and ionospheric delay $I_{1,r}^{''k}$ of the second order. The choice of the weights is determined by the level of constraints on each term on the right side of Eq. (2.25). The first term ρ' denotes the geometry term which can be scaled to any arbitrary value h_1 , i.e [10].

$$\sum_{m=0}^M (\alpha_m + \gamma_m) = h_1 \tag{2.26}$$

A geometry-free combination is obtained if $h_1 = 0$, geometry-preserving if $h_1 = 1$. In a similar way, the first order ionospheric delay $I_{1,r}^k$ can be scaled by any arbitrary value h_2 as follows [10]:

$$\sum_{m=0}^M (\alpha_m - \gamma_m) q_{1m}^2 = h_2 \tag{2.27}$$

where ionosphere-free combination corresponds to $h_2 = 0$, ionosphere-preserving to $h_2 = 1$. Second order ionospheric delay can be treated in the similar way.

The next term on the right side of Eq. (2.25) describes the linear combination of integer ambiguities which is equal to an integer ambiguity N_u^k times the wavelength λ_m of the linear combination. The corresponding phase weight is given by

$$\alpha_m = \frac{j_m \lambda}{\lambda_m} \tag{2.28}$$

where j_m is an integer weight.

The last term of eq. (2.25) describes the linear combination of phase and code noises. Its variance is given by:

$$\sigma^2 = \sum_{m=0}^M (\alpha_m^2 \sigma_{\varepsilon_{r,m}^k}^2 + \gamma_m^2 \sigma_{\eta_{r,m}^k}^2) \tag{2.29}$$

Taking into account all constraints, optimum α_m and γ_m are determined to maximize ambiguity discrimination D :

$$D = \frac{\lambda}{2\sigma} \quad (2.30)$$

Its maximization corresponds to the minimization of the probability of wrong fixing for a geometry-free, ionosphere-free linear combination. For the details on determination of the coefficients α_m and γ_m refer to [10], [11] and [12].

3. Precise positioning with Galileo

This chapter focuses on the evaluation of the Galileo system capability for precise absolute, as well as relative positioning. First, an introduction into the Galileo system is provided, including its innovations compared to GPS, current status and signals. Then, the first static short-baseline test is described. The noise level of double-difference Galileo E1-E5 code measurements is discussed and the reliability of widelane integer ambiguity resolution with double-difference E1-E5 code and phase measurements in terms of the ratio of the squared measurement residuals is presented. Afterwards, the second kinematic long-baseline test is described. The stability of the single-epoch float ambiguity estimation in RTK positioning with Melbourne-Wübbena linear combinations is demonstrated. In addition, the Galileo fixed phase residuals of integer-fixed widelane code-carrier combination and float-fixed narrowlane phase-only combination are compared. Moreover, we compare the fixed phase residuals of PPP with GPS and Galileo and observe an improved performance of Galileo even for the equal weighting of both measurements. Finally, the joint subset optimization and integer least-squares estimation in case of phase cycle slips for PPP and RTK with GPS and Galileo is presented.

3.1 The European Global Navigation Satellite System Galileo

Once fully operational, Galileo Walker constellation will include 30 satellites (27 operational and 3 spares) in Medium Earth Orbit (MEO) spread evenly around each of three orbital planes with inclination of 56° to the equator [4]. The inclination of Galileo orbital planes was chosen to provide a better coverage at high latitudes, especially for operation over northern Europe, an area poorly covered by GPS. The orbital revolution period of the Galileo satellite is 14 h 7 min.

Galileo is independent but fully interoperable with GPS and GLONASS [13], which will roughly double the number of satellites available for positioning at every moment in the future. This will allow more accurate and reliable position determination even in rather difficult environments such as big cities where high buildings can obscure signals from low-elevation satellites. Although similar to GPS, Galileo offers a few technical innovations not available to civilian users before. Table 3.1 summarizes most important of them according to Henkel [2].

Falcone et al. described the current status of the Galileo system in [14]. The deployed satellite constellation includes four satellites: Galileo PFM (PRN 11), Galileo FM2 (PRN 12), Galileo FM3 (PRN 19) and Galileo FM4 (PRN 20). At the moment its program is in In-Orbit Validation

Orbits	Altitude of 23200 km: ⇒ Ground track repetition period of 10 days (instead of 1 day for GPS) ⇒ Reduction of resonances due to periodic movement over areas with irregular gravitational field → less satellite maneuvers required
Satellites	H2 maser as satellite clock: ⇒ Improved stability over relevant time intervals ⇒ Improved estimation of satellite clock errors
Signals	- Three frequency bands with larger signal bandwidths: ⇒ Improved estimation and elimination of ionospheric delays of first and second order ⇒ Increased reliability of carrier phase integer ambiguity resolution - Binary Offset Carrier (BOC) modulation → power shift to the edges of spectrum: ⇒ Lower Cramer Rao bound ⇒ Improved code delay tracking and stronger multipath suppression - Composite BOC on E1, linear combination of BOC(1,1) and BOC(6,1) modulations: ⇒ Receivable signal for narrowband receivers ⇒ Low noise level and multipath for wideband receivers

Table 3.1: Innovations of Galileo [2]

(IOV) phase, which consists of qualifying the ground, space and user segments through continuous operation, as well as extensive in-orbit and on-ground tests.

The Galileo IOV satellites transmit modulated signals on all three carriers, as well as navigation messages for the following types of services: F/NAV corresponding to the Open Service (OS), I/NAV corresponding to the Safety of Life (SoL), and G/NAV corresponding to the Public Regulated Service (PRS). In the current configuration, the navigation message signal flags are set as follows:

- Signal Health Status flag is set to "Signal component is currently in test", indicating that validation testing is still going;
- Data Validity Status flag can be set to "Nominal" or "Working without guarantee" depending on when navigation data were last uploaded on-board of the satellites.

These flags are used by receivers to determine whether or not to track a satellite and include its range measurements and corresponding navigation data as valid input into the positioning algorithm. With four operational satellites present at the moment, Galileo-only position fix achievement and its performance depends on the location of receivers and the time of a test. Overall, the complete Galileo constellation is visible for maximum two to five hours per day depending on location [14].

3.2 Galileo signals

Each Galileo satellite transmits three independent Code Division Multiple Access (CDMA) signals, named E1, E5 and E6. The E5 signal is further sub-divided into two signals denoted E5a and E5b. Each signal supports one or more services planned to be provided by Galileo. Galileo carrier signal characteristics are presented in Table 3.2.

Signal	Carrier frequency (MHz)	Receiver reference bandwidth (MHz)	Modulation type (OS)
E1	1575,420	24,552	CBOC(6,1,1/11)
E5a	1278,750	20,460	BPSK(10)
E5b	1191,795	20,460	BPSK(10)
E5	1176,450	51,150	AltBOC(15,10)
E6	1207,140	40,920	BPSK(5) (CS)

Table 3.2: Galileo carrier signals [1]

A major difference of Galileo signals to the signals currently emitted by other GNSS is BOC (resp. AltBOC) modulation scheme and the large bandwidth employed for most of the signals [13]. The standard BOC modulation is a square subcarrier modulation. The baseband signal is multiplied by a rectangular subcarrier, which splits the spectrum of the signal into two parts, located on the left and the right side of the carrier frequency. Such modulation scheme presents several advantages as described in Table 3.1. The idea of alternate BOC (AltBOC) modulation is to perform the same process but multiplying the base band signal by a *complex* rectangular subcarrier. As a result, the signal spectrum is not split up, but only shifted to higher (or lower) frequencies [13]. Galileo E5 is generated by a special multiplexing that combines two signals (E5a and E5b) in a constant envelope, and then amplified through a very wideband amplifier [15]. The final bandwidth of the signal is 51.150 MHz [1]. For more details on the Galileo system signals design and BOC modulation refer to [7], [1] and [13].

The generation of combined E5 signal presents several advantages [13]:

- gain in precision due to shift of the signal power to the edges of the spectrum;
- low correlation losses, thermal noise and code multipath;
- optimization of the use of E5a and E5b signals: low-cost receivers can use a single band, whereas more complex receivers can operate in a dual mode single band mode (non-coherent reception of E5a and E5b signals) or in a coherent dual band mode (reception of E5 signal) to get advantages in term of performance.

3.3 Static short-baseline test

For the static short-baseline test a set-up of two test receivers was arranged at the Roof Laboratory of the Institute for Communications and Navigation of Technische Universität München (TUM) with a fixed baseline of 1.25 m (see Fig. 3.1). The skyplot plot of the Galileo satellites during the test is presented in Fig. 3.2 showing PRN 12 with the high elevation over 70° and PRN 11, PRN 19 and PRN 20 with elevations higher than 20° .



Figure 3.1: Static short-baseline test set-up. Crosses mark the positions of the test receivers

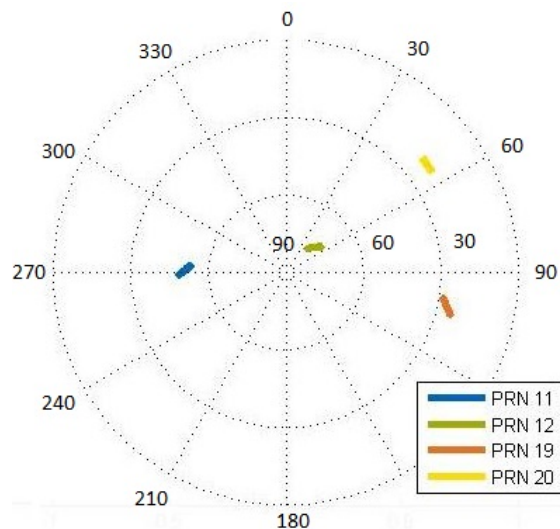


Figure 3.2: Skyplot Roof Laboratory of the Institute for Communications and Navigation of TUM

Single-epoch E1-E5 widelane integer ambiguity resolution for a baseline of 1.25 m with baseline length and height a priori information (as determined by GPS) was performed according to the following procedure:

1. Calculation of ionosphere-free combination $\rho_{1,IF}^k$ for code measurements of receiver 1 according to Eq. (2.15) with coefficients $\alpha_{E1} = 2.261$ and $\alpha_{E5} = -1.261$ determined according to Eq. (2.14).
2. Least-squares single-epoch estimation of the absolute position \vec{x}_{r_1} of receiver 1 from ionosphere-free code-only combination. Slant tropospheric delays T_1^k are estimated according to the blind MOPS model as described in the Section 4.2. The covariance matrix of ionosphere-free code combination is obtained by the estimation of the noise statistics with an exponential delay model [16]. The inverse of the covariance matrix provides the weighting matrix for the least-squares estimation. The final position of receiver 1 is obtained by the averaging of the results over time. For more details on the least-squares estimation refer to e.g. [7].
3. Computation of E1-E5 double-difference code measurements $\rho_{12,m}^{1k}$ according to Eq. (2.9), as well as double-difference E1-E5 phase measurements $\varphi_{12,m}^{1k}$ according to Eq. (2.11). PRN 12 was assumed to be the reference satellite as the one with the highest elevation. From E1-E5 double-difference phase measurements, the widelane combination $\lambda_{WL}\varphi_{12}^{kl}$ is calculated according to Eq. (2.19). Forming double differences eliminates both receiver and satellite biases, as well as clock offsets [10]. In addition, ionospheric and tropospheric effects are canceled on a short baseline. Moreover, the widelane combinations increases wavelength to $\lambda_{WL} = 75.2$ cm. This simplifies the resolution of the carrier phase integer ambiguities.
4. Estimation of noise statistics from a number of double-difference code measurements and widelane combination for the measurement covariance matrix [17].
5. Determination of single-epoch constrained least-squares float solution of the baseline vector and widelane ambiguities for every epoch, which takes a priori information about the horizontal baseline length and height into account.

The double-difference code as well as widelane combination measurements for every epoch in matrix-vector notation are given by:

$$\Psi = \begin{pmatrix} \rho_{12,E1}^{12} \\ \vdots \\ \rho_{12,E1}^{1K} \\ \rho_{12,E5}^{12} \\ \vdots \\ \rho_{12,E5}^{1K} \\ \lambda_{WL}\varphi_{12}^{12} \\ \vdots \\ \lambda_{WL}\varphi_{1K}^{1K} \end{pmatrix} = H_{\text{geo,L}}\xi_L + AN + \eta, \quad (3.1)$$

with the differential geometry matrix $H_{\text{geo,L}}$ and the baseline vector $\xi_L = R_L \vec{b}_{12}$ in the local East-North-Up frame, the transformation matrix R_L from the Earth-Centered, Earth-Fixed (ECEF) to ENU coordinate frame, the double-difference widelane ambiguities N , the mapping matrix A which maps the differential ambiguities into the measurements as well as measurement noise η . Considering the a priori knowledge about the height component z_L and the length $l_{\text{ap}} = 1.25$ m of the horizontal baseline $\xi_L = (x_L, y_L)^T$, the measurement model can be simplified to:

$$\begin{aligned}\tilde{\Psi} &= \Psi - H_{\text{geo,L}}^{(z)} z_L \\ &= H_{\text{geo,L}}^{(x,y)} \xi_L + AN + \eta \text{ with } \|\xi_L\| = l_{\text{ap}}\end{aligned}\quad (3.2)$$

We express the least-squares optimization (minimization) problem with a baseline length constraint as a Lagrange optimization, i.e. [18]

$$\min_{\xi_L, N, \mu} \left\| \Psi - H_{\text{geo,L}}^{(x,y)} \xi_L - AN \right\|_{\Sigma_{\Psi}^{-1}}^2 + \mu \cdot (\|\xi_L\|^2 - l_{\text{ap}}^2), \quad (3.3)$$

where μ is the Lagrange parameter. Introducing the vector of unknowns $\tilde{\xi}_L = (\xi_L^T, N^T)$, the combined geometry matrix $\tilde{H}_{\text{geo,L}} = (H_{\text{geo,L}}^{(x,y)}, A)$ and selection matrix $S = (1^{2 \times 2}, 0^{2 \times K-1})$, we reformulate the problem (3.3) as:

$$\min_{\tilde{\xi}_L, \mu} \left\| \tilde{\Psi} - \tilde{H}_{\text{geo,L}} \tilde{\xi}_L \right\|_{\Sigma_{\tilde{\Psi}}^{-1}}^2 + \mu \cdot (\|S \tilde{\xi}_L\|^2 - l_{\text{ap}}^2) \quad (3.4)$$

To find the constrained float solution of the baseline components and differential ambiguities, the partial derivative of the cost function of (3.8) with respect to $\tilde{\xi}_L$ is set to zero. Solving it for $\tilde{\xi}_L$ yields:

$$\hat{\tilde{\xi}}_L = (\tilde{H}_{\text{geo,L}}^T \Sigma_{\tilde{\Psi}}^{-1} \tilde{H}_{\text{geo,L}} + \mu S^T S)^{-1} \tilde{H}_{\text{geo,L}}^T \Sigma_{\tilde{\Psi}}^{-1} \tilde{\Psi} \quad (3.5)$$

The corresponding Lagrange parameter μ is determined by inserting Eq. (3.5) in the original equation of the constraint (3.8) and finding the root of the function

$$f(\mu) = \|S(\tilde{H}_{\text{geo,L}}^T \Sigma_{\tilde{\Psi}}^{-1} \tilde{H}_{\text{geo,L}} + \mu S^T S)^{-1} \tilde{H}_{\text{geo,L}}^T \Sigma_{\tilde{\Psi}}^{-1} \tilde{\Psi}\|^2 - l_{\text{ap}}^2 \quad (3.6)$$

As no closed solution of (3.6) exist, the root is found iteratively with the secant method. The estimate of μ on the (n+1)-th iteration is determined as:

$$\mu^{(n+1)} = \mu^{(n)} - \frac{f(\mu)}{f'(\mu)} \Big|_{\mu=\mu^{(n)}} \text{ with } \mu^{(0)} = 0 \quad (3.7)$$

6. Integer search for widelane double-difference integer ambiguities candidate vectors is performed.

The unconstrained least-squares minimization problem is given by:

$$\min_{\xi_L, N} \left\| \tilde{\Psi} - H_{\text{geo,L}}^{(x,y)} \xi_L - AN \right\|_{\Sigma_{\tilde{\Psi}}^{-1}}^2, \quad (3.8)$$

Decomposing (3.8) into two orthogonal terms, we get:

$$\begin{aligned} & \left\| \tilde{\Psi} - H_{\text{geo,L}}^{(x,y)} \xi_L - AN \right\|_{\Sigma_{\tilde{\Psi}}^{-1}}^2 \\ &= \left\| P_H(\tilde{\Psi} - H_{\text{geo,L}}^{(x,y)} \xi_L - AN) + P_H^\perp(\tilde{\Psi} - H_{\text{geo,L}}^{(x,y)} \xi_L - AN) \right\|_{\Sigma_{\tilde{\Psi}}^{-1}}^2 \\ &= \left\| P_H(\tilde{\Psi} - H_{\text{geo,L}}^{(x,y)} \xi_L - AN) \right\|_{\Sigma_{\tilde{\Psi}}^{-1}}^2 + \left\| P_H^\perp(\tilde{\Psi} - H_{\text{geo,L}}^{(x,y)} \xi_L - AN) \right\|_{\Sigma_{\tilde{\Psi}}^{-1}}^2 \\ &= \left\| P_H(\tilde{\Psi} - H_{\text{geo,L}}^{(x,y)} \xi_L - AN) \right\|_{\Sigma_{\tilde{\Psi}}^{-1}}^2 + \left\| (P_H^\perp \tilde{\Psi} - \bar{A}N) \right\|_{\Sigma_{\tilde{\Psi}}^{-1}}^2 \end{aligned} \quad (3.9)$$

where P_H^\perp is an orthogonal projector on the space H , $P_H + P_H^\perp = 1$ and $\bar{A} = P_H^\perp A$.

We multiply the measurement vector given by the model (3.2) by P_H^\perp :

$$\begin{aligned} P_H^\perp \tilde{\Psi} &= P_H^\perp (H_{\text{geo,L}}^{(x,y)} \xi_L + AN + \eta) \\ &= \bar{A}N + P_H^\perp \eta \end{aligned} \quad (3.10)$$

The least-squares optimization of the float solution of ambiguities N is written as follows:

$$\min_N \left\| P_H^\perp \tilde{\Psi} - \bar{A}N \right\|_{\Sigma_{\tilde{\Psi}}^{-1}}^2, \quad (3.11)$$

Consequently, the unconstrained float solution of N is given by:

$$\hat{N} = (\bar{A}^T \Sigma_{\tilde{\Psi}}^{-1} \bar{A})^{-1} \bar{A}^T \Sigma_{\tilde{\Psi}}^{-1} (P_H^\perp \tilde{\Psi}) \quad (3.12)$$

The projector $P_{\bar{A}}$ on the space \bar{A} is defined as:

$$P_{\bar{A}} = \bar{A} (\bar{A}^T \Sigma_{\tilde{\Psi}}^{-1} \bar{A})^{-1} \bar{A}^T \Sigma_{\tilde{\Psi}}^{-1} \quad (3.13)$$

where $P_{\bar{A}} \bar{A} = \bar{A}$.

Thus the second term of (3.9) can be decomposed into two orthogonal terms as:

$$\left\| P_{\bar{A}}^\perp (P_H^\perp \tilde{\Psi} - \bar{A}N) + P_{\bar{A}} (P_H^\perp \tilde{\Psi} - \bar{A}N) \right\|_{\Sigma_{\tilde{\Psi}}^{-1}}^2 = \left\| P_{\bar{A}}^\perp P_H^\perp \tilde{\Psi} \right\|_{\Sigma_{\tilde{\Psi}}^{-1}}^2 + \left\| \bar{A}(\hat{N} - N) \right\|_{\Sigma_{\tilde{\Psi}}^{-1}}^2 \quad (3.14)$$

where $P_{\bar{A}} + P_{\bar{A}}^\perp = 1$.

The first term of (3.9) can be re-written as follows:

$$\begin{aligned} \left\| P_H(\tilde{\Psi} - H_{\text{geo,L}}^{(x,y)}\xi_L - AN) \right\|_{\Sigma_{\tilde{\Psi}}^{-1}}^2 &= \left\| P_H(\tilde{\Psi} - AN) - P_H H_{\text{geo,L}}^{(x,y)}\xi_L \right\|_{\Sigma_{\tilde{\Psi}}^{-1}}^2 \\ &= \left\| H_{\text{geo,L}}^{(x,y)}(\check{\xi}_L(N) - \xi_L) \right\|_{\Sigma_{\tilde{\Psi}}^{-1}}^2 \end{aligned} \quad (3.15)$$

where the unconstrained fixed baseline estimate $\check{\xi}_L(N)$ is given by:

$$\check{\xi}_L(N) = (H_{\text{geo,L}}^T \Sigma_{\tilde{\Psi}}^{-1} H_{\text{geo,L}})^{-1} H_{\text{geo,L}}^T \Sigma_{\tilde{\Psi}}^{-1} (\tilde{\Psi} - AN) \quad (3.16)$$

Finally, (3.9) can be presented as combination of three different terms:

$$\left\| H_{\text{geo,L}}^{(x,y)}(\check{\xi}_L(N) - \xi_L) \right\|_{\Sigma_{\tilde{\Psi}}^{-1}}^2 + \left\| \bar{A}(\hat{N} - N) \right\|_{\Sigma_{\tilde{\Psi}}^{-1}}^2 + \left\| P_A^\perp P_H^\perp \tilde{\Psi} \right\|_{\Sigma_{\tilde{\Psi}}^{-1}}^2 \quad (3.17)$$

where the first term denotes the residuals of the baseline, second term - integer ambiguity residuals and third term - irreducible noise. The first term can be set to zero by choosing $\check{\xi}_L(N) = \xi_L$. The integer search for the ambiguities is based on the minimization of the second term and is performed with the unconstrained LAMBDA method of Teunissen, which includes decorrelation of the float ambiguities as a prerequisite of an efficient search ([19] and [20]). For each integer candidate vector the squared weighted sum of the measurement residuals is computed as

$$\left\| \tilde{\Psi} - H_{\text{geo,L}}\check{\xi}_L - A\check{N} \right\|_{\Sigma_{\tilde{\Psi}}^{-1}}^2 \quad (3.18)$$

The vector of candidates which minimizes the sum (3.18) is selected.

7. Fixing of E1-E5 widelane double-difference integer ambiguities \check{N} and determination of single-epoch least-squares fixed solution for the baseline vector $\check{\xi}_L$ using unambiguous double-difference widelane phase combination measurements $\lambda_{\text{WL}}\tilde{\varphi}_{12}^{kl}$.

The double-difference Galileo E1-E5 code measurements are presented in Fig. 3.3 and Fig. 3.4 respectively. The standard deviation of the double-difference code measurements between two test receivers and satellites PRN 11 and PRN 12 over a minute is $\sigma_{\text{E1}}^{(11,12)} = 20.6$ cm on E1 and $\sigma_{\text{E5}}^{(11,12)} = 4.7$ cm on E5. As the noise of double difference measurements is increased by about a factor of 2 with the respect to the noise of individual measurements under assumption of equal individual measurement noise, the corresponding individual measurements noise is $\sigma_{\text{E1}}^{11}(E = 50^\circ) = 10.3$ cm on E1 and $\sigma_{\text{E5}}^{11}(E = 50^\circ) = 2.3$ cm on E5. This result demonstrates that the Galileo signals design represent clear advantage in terms of code noise reduction. In addition, the coherent reception of broadband E5 signal must be performed to fully benefit from its low code noise. It opens new possibilities for the precise positioning with low-cost single-frequency GNSS receivers.

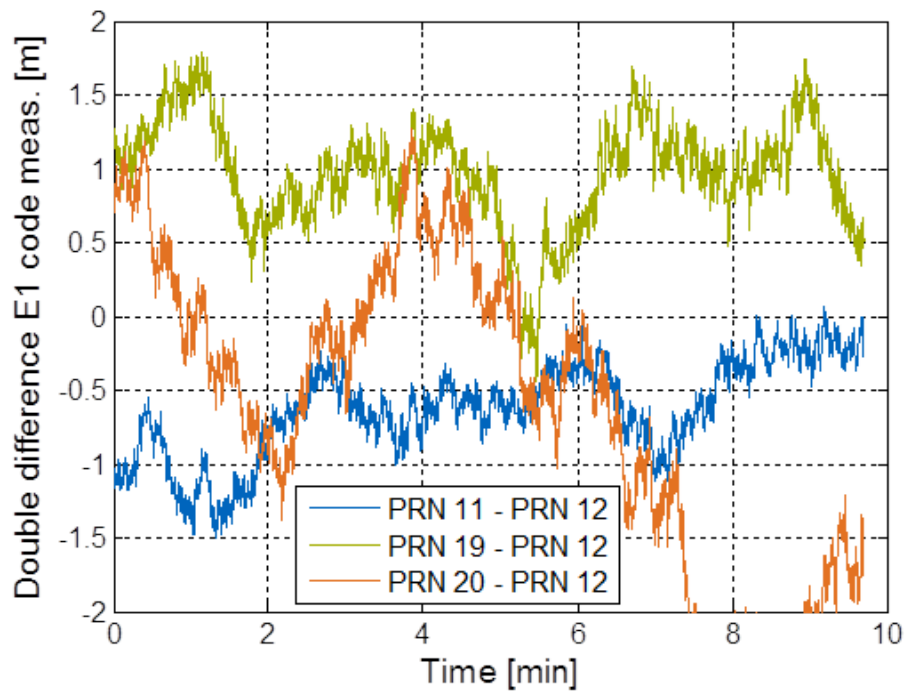


Figure 3.3: Double-difference E1 Galileo code measurements

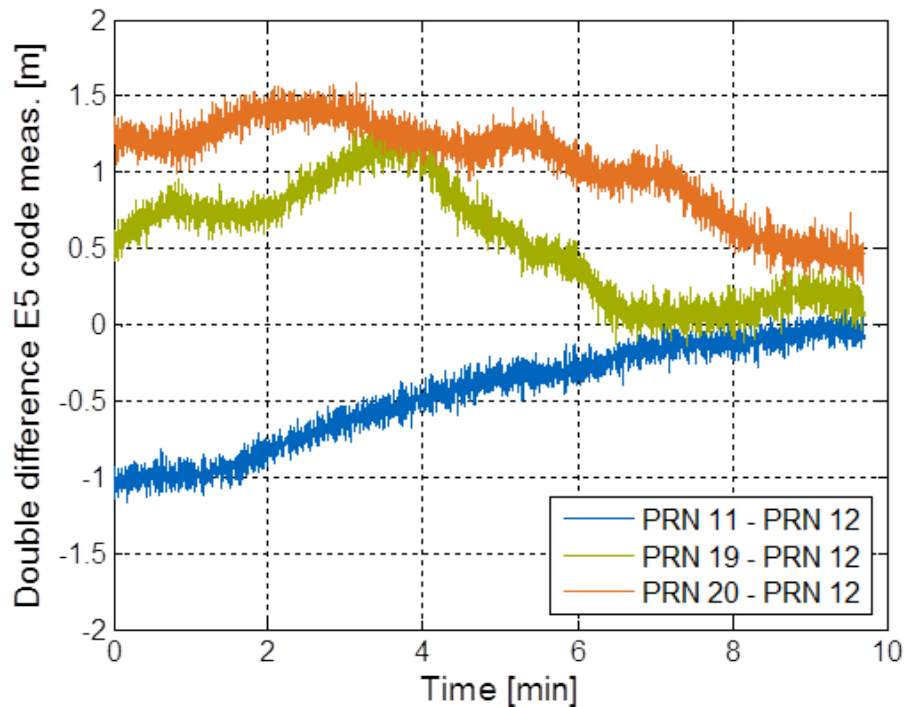


Figure 3.4: Double-difference E5 Galileo code measurements

The ratio of the squared weighted sum of the measurement residuals of the second best integer candidates vector \check{N}_2 to the best integer candidates vector \check{N}_1 of the integer ambiguity search is computed as follows:

$$r = \frac{\left\| \tilde{\Psi} - H_{\text{geo,L}} \check{\xi}_L - A \check{N}_2 \right\|_{\Sigma_{\tilde{\Psi}}^{-1}}^2}{\left\| \tilde{\Psi} - H_{\text{geo,L}} \check{\xi}_L - A \check{N}_1 \right\|_{\Sigma_{\tilde{\Psi}}^{-1}}^2} \quad (3.19)$$

The typical ratio for L1-L2 integer ambiguity resolution is 1-2. Therefore additional information has to be used for reliable selection of integer candidates, e.g. the difference between the length of the baseline estimate and the a priori known baseline. Based on this approach, the Maximum A posteriori estimator was developed by Henkel et al., that combines both error norms for integer ambiguity resolution [18]. The ratio of the integer search of E1-E5 widelane double-difference integer ambiguity resolution is presented in Fig. 3.5, taking values between 20 and 220. This considerably simplifies the selection of the correct candidate for integer ambiguity based on the squared weighted sum of the measurement residuals. Note that each of the 1600 independent ambiguity resolutions performed for this test was correct. It demonstrates that the integer ambiguity resolution with Galileo E1-E5 signals is extremely reliable. The phase residuals of E1-E5 constrained fixed solution are presented in Fig. 3.6. The residuals are in the order of a few centimeters, that is a good indicator of correct ambiguity fixing. Offset and drifts observed are attributed to interferences and multipath.

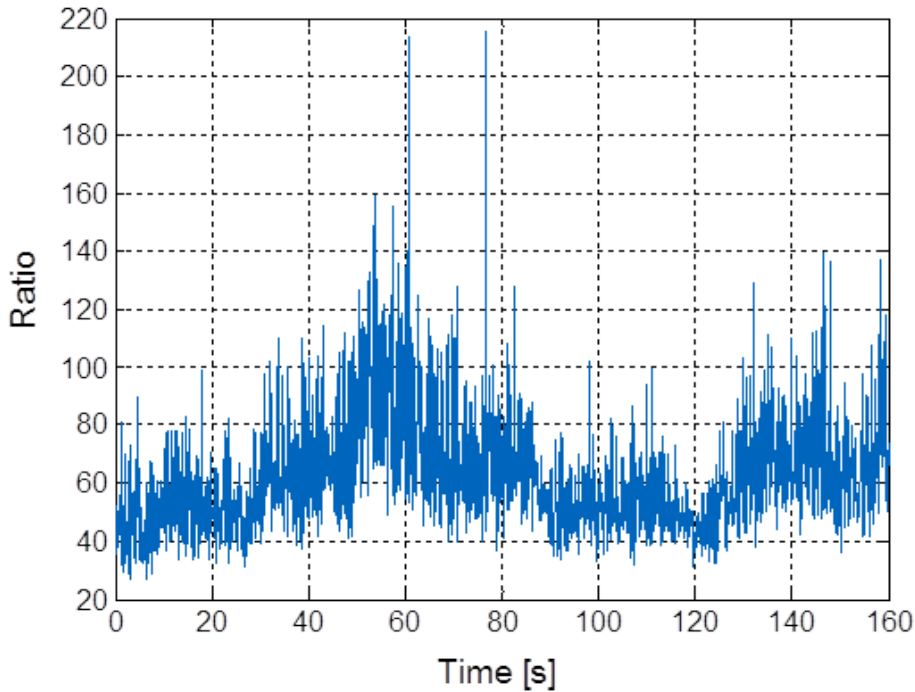


Figure 3.5: Error norm ratio of integer LAMBDA search

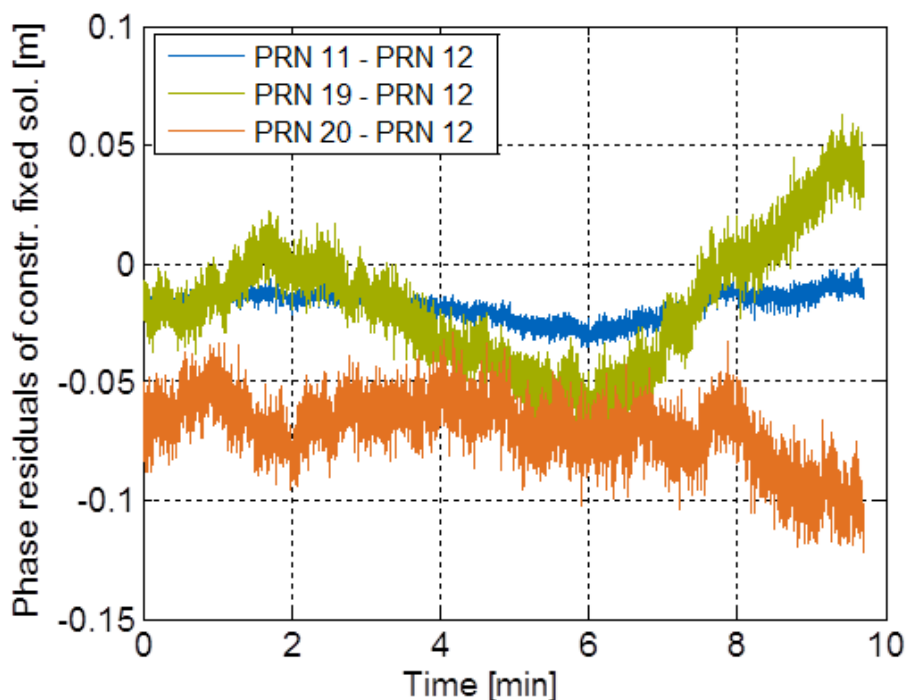


Figure 3.6: Phase residuals of E1-E5 constrained fixed solution

3.4 Kinematic long-baseline test

For the kinematic long-baseline test, one test receiver was arranged at the Roof Laboratory of the Institute for Communications and Navigation of TUM, while another test receiver was mounted in a car. The mobile test was performed in the urban area of Maisach, Germany, with baseline length of about 25 km (see Fig. 3.7). The visibility plot of Galileo satellites during the test is presented in Fig. 3.8, showing PRN 12 and PRN 19 with high elevations over 70° and PRN 11 with elevation higher than 40° . PRN 20 was not available at the time of the test due to a two weeks transmission outage.

3.4.1 Long-range RTK with 25 km kinematic baseline

For long-range RTK with 25 km kinematic baseline ambiguity resolution with three different linear combinations was performed: the Melbourne-Wübbena linear combination, the code-carrier widelane linear combination and the phase-only narrowlane linear combination.

Single-epoch L1-L2 and E1-E5 widelane ambiguity resolution with Melbourne-Wübbena linear combination was performed using measurements from Galileo and GPS jointly according to the following procedure:



Figure 3.7: Mobile long-baseline test set-up

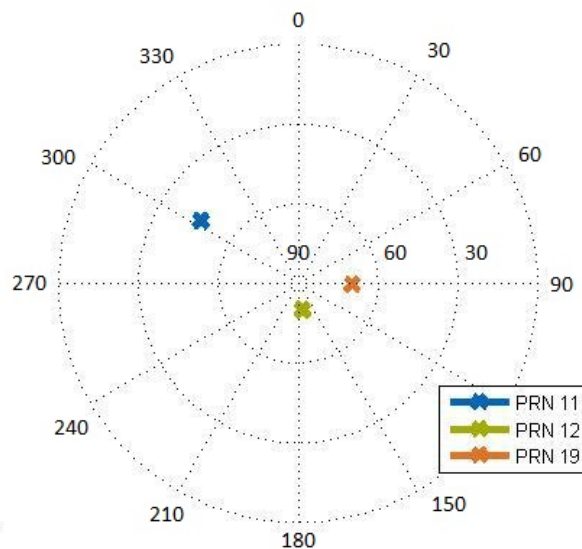


Figure 3.8: Skyplot Roof Laboratory of the Institute for Communications and Navigation of TUM

1. Calculation of ionosphere-free combination $\rho_{1,IF}^k$ for code measurements of the receiver 1 according to Eq. (2.15) with coefficients $\alpha_{L1} = 2.546$ and $\alpha_{L2} = -1.546$ for GPS L1-L2 and $\alpha_{E1} = 2.261$ and $\alpha_{E5} = -1.261$ for Galileo E1-E5 determined according to Eq. (2.14).
2. Least-squares single-epoch estimation of absolute position of receiver 1 from ionosphere-free code-only combination as described in Section 3.3. The final position of the receiver 1 is obtained by the averaging of the result over time.

3. Computation of L1-L2 and E1-E5 double-difference $\rho_{12,m}^{kl}$ code measurements according to Eq. (2.9) and double-difference $\varphi_{12,m}^{kl}$ phase measurements according to Eq. (2.11). From double-difference measurements the Melbourne-Wübbena linear combination was computed according to Eq. (2.23). The double-difference eliminates receiver and satellite clock offsets, as well as biases. The Melbourne-Wübbena combination increases the wavelength to $\lambda_{WL} = 86.2$ cm for GPS L1-L2 and $\lambda_{WL} = 75.2$ cm for Galileo E1-E5. It contains only widelane double-difference ambiguities and code noise, and thus assumes a constant value for time intervals without cycle slips.
4. Determination of the unconstrained single-epoch least-squares float solution for the baseline components \hat{b}_{12} and widelane double-difference ambiguities $\hat{N}_{12,WL}^{kl}$.

A comparison of L1-L2 and E1-E5 widelane ambiguities is presented in Fig. 3.9 and Fig. 3.10. The mean value for each ambiguity was calculated and subtracted for the ease of comparison.

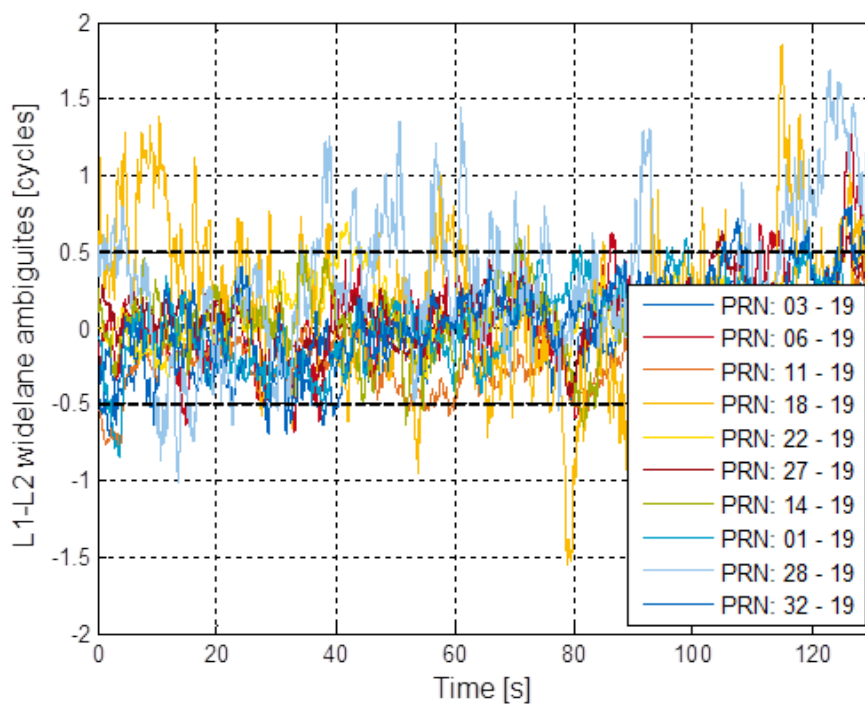


Figure 3.9: GPS L1-L2 double-difference widelane ambiguities

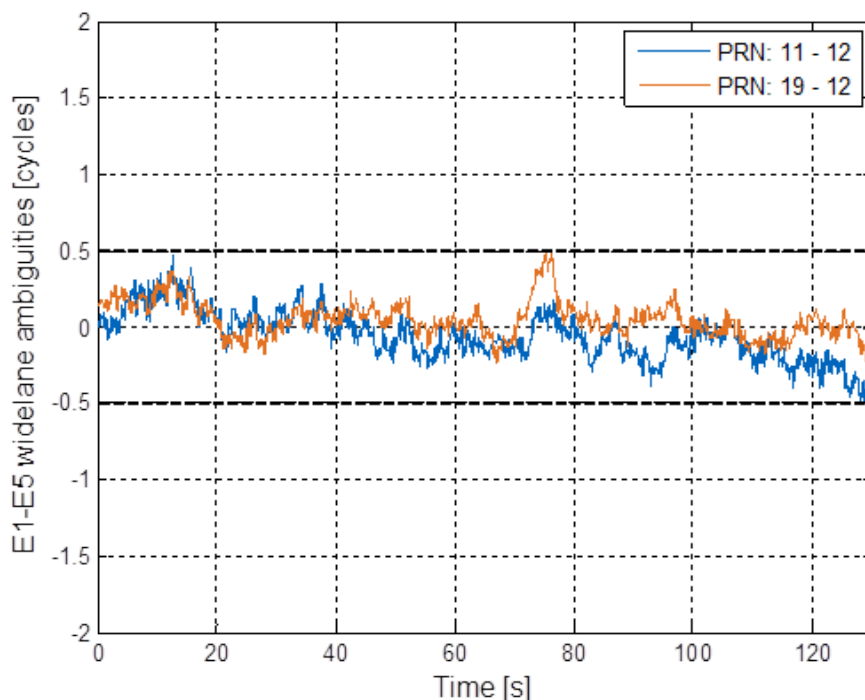


Figure 3.10: Galileo E1-E5 double-difference widelane ambiguities

Ambiguity resolution with the Melbourne-Wübbena combination is determined by the code noise of individual measurements. Galileo E1-E5 widelane double-difference ambiguities vary between ± 0.5 cycles, while for GPS L1-L2 ambiguities the variation reaches values of ± 2 cycles. It demonstrates that Galileo E1-E5 ambiguity resolution for RTK with the Melbourne-Wübbena combination is more accurate and reliable, benefiting from lower code noise of Galileo signals. The use of Galileo E1-E5 signals will reduce the initialization time for RTK.

Single-epoch E1-E5 ambiguity resolution with the code-carrier widelane linear combination and phase-only narrowlane linear combination is performed using the Galileo measurements according to the following procedure:

1. Calculation of ionosphere-free combination $\rho_{1,IF}^k$ for code measurements of receiver 1 according to Eq. (2.15) with coefficients $\alpha_{E1} = 2.261$ and $\alpha_{E5} = -1.261$ determined according to Eq. (2.14).
2. Least-squares single-epoch estimation of absolute position of receiver 1 from ionosphere-free code combination as described in Section 3.3. The final position of the receiver 1 is obtained by the averaging of the result over time.
3. Computation of E1-E5 double-difference code measurements $\rho_{12,m}^{kl}$ according to Eq. (2.9) and double-difference phase measurements $\varphi_{12,m}^{kl}$ according to Eq. (2.11). Geometry-preserving, ionosphere-free code-carrier widelane combination of minimum noise amplification with

wavelength of $\lambda = 3.092$ m is computed from E1-E5 double-difference code and phase measurements according to Eq. (2.25) with the following coefficients:

$$\begin{aligned}\alpha_{E1} &= 16.25 & \alpha_{E5} &= -12.29 \\ \gamma_{E1} &= 0.08 & \gamma_{E5} &= -3.04\end{aligned}$$

Coefficients were determined from the following criteria as described in Section 2.3:

- geometry-preserving constraint ($h_1 = 1$);
- ionosphere-free constraint ($h_2 = 0$);
- integer ambiguity coefficients $j_{E1} = 1$ and $j_{E5} = -1$;
- phase noise $\sigma_\varphi = 1$ mm, code noise $\sigma_{\rho,E1} = 11.14$ cm on E1 and code noise $\sigma_{\rho,E5} = 1.95$ cm on E5 [10];
- minimization of the noise variance of the E1-E5 code-carrier combination.

The geometry-preserving, ionosphere-free phase-only combination $\varphi_{12,IF}^k$ of minimum noise amplification is computed from E1-E5 double-difference phase measurements according to Eq. (2.15).

4. Determination of unconstrained least-squares single-epoch float solution for the baseline components \hat{b}_{12} as well as ambiguities \hat{N}_{12}^{kl} . A priori information on height component is taken as computed from GPS measurements.
5. Ambiguity fixing and computation of least-squares single-epoch fixed solution from unambiguous measurement combinations. Large wavelength of widelane code-carrier combination simplifies integer ambiguity resolution, so the float ambiguities are rounded to the nearest integer values and fixed. Phase-only combination possesses lower noise, therefore ambiguities are fixed to the real float values in order to allow absorption of unconsidered measurement errors.

Double-difference residuals of integer-fixed E1-E5 widelane code-carrier combination and real-fixed E1-E5 phase-only combination are presented in Fig. 3.11 and Fig. 3.12. Residuals of integer-fixed are in the order of 1 m, while real-fixed only in the order of 1 cm due to low noise of phase measurements.

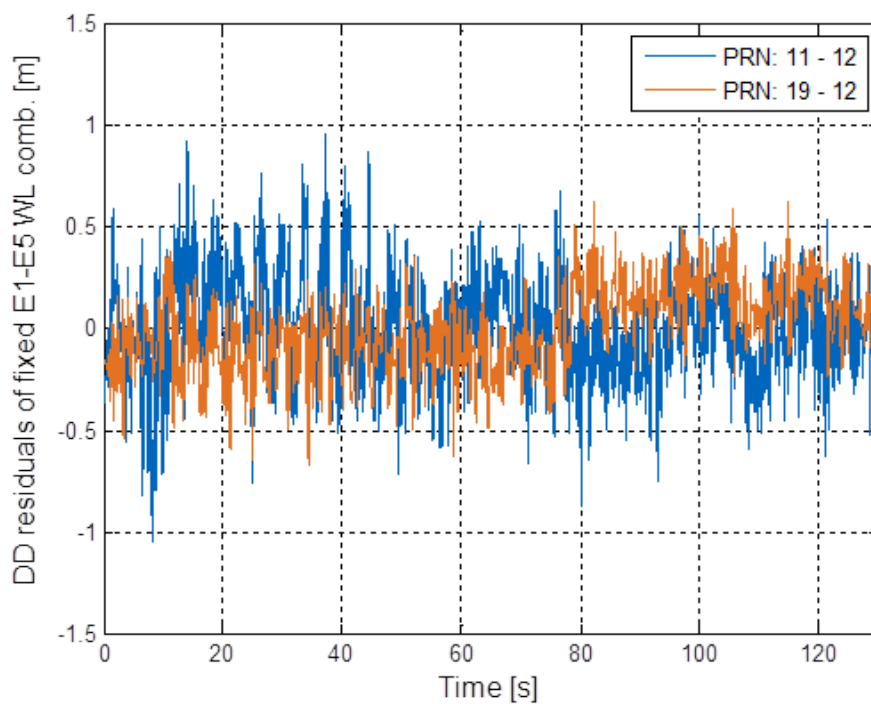


Figure 3.11: Residuals of integer-fixed E1-E5 wide-lane code-carrier combination

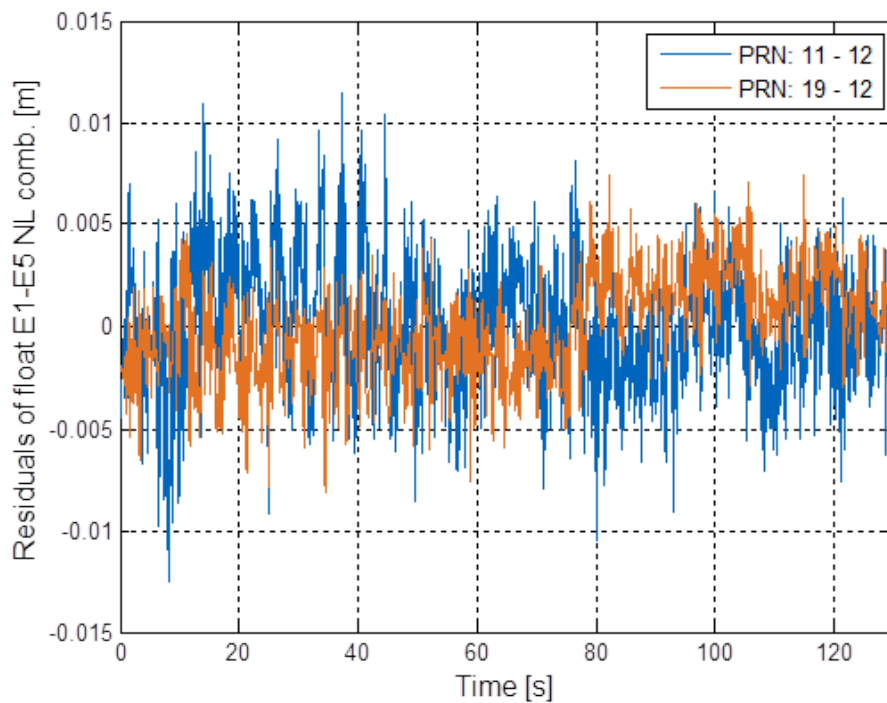


Figure 3.12: Residuals of real-fixed E1-E5 narrow-lane phase-only combination

3.4.2 Precise Point Positioning

The traditional Precise Point Positioning scheme is based on Laurichesse's model [21], while we adapt a different approach. The absolute kinematic position of the mobile receiver 2 was estimated for every epoch without any corrections using measurements from Galileo and GPS jointly according to the following procedure:

1. Calculation of ionosphere-free combination $\rho_{2,\text{IF}}^k$ for code measurements and $\varphi_{2,\text{IF}}^k$ for phase measurements of receiver 2 according to Eq. (2.15) with coefficients $\alpha_{L1} = 2.546$ and $\alpha_{L2} = -1.546$ for GPS L1-L2 and $\alpha_{E1} = 2.261$ and $\alpha_{E5} = -1.261$ for Galileo E1-E5 determined according to Eq. (2.14).
2. Least-squares single-epoch estimation of the absolute three-dimensional position \hat{x}_{r_2} of the receiver 2, receiver clock offsets $\delta\hat{t}_{2,\text{GPS}}$ for GPS and $\delta\hat{t}_{2,\text{Galileo}}$ for Galileo, as well as float ambiguities \hat{N}_2^k using ionosphere-free code-only and phase-only combinations. Slant tropospheric delays \hat{T}_2^k are modeled according to blind MOPS model as described in Section 4.2. Covariance matrix of ionosphere-free code and phase combinations is obtained by the estimation of the combinations statistics with an exponential delay model [16]. The inverse of the covariance matrix provides weighting matrix for the least-squares solution [4].
3. Averaging of the float ambiguities \hat{N}_2^k and fixing to real float values to allow absorption of satellite and receiver biases, as well as errors such as tropospheric, satellite clock and orbit modeling errors.
4. Determination of fixed least-squares solution for three-dimensional receiver position \check{x}_2^k , as well receiver clock offsets $\delta\check{t}_{2,\text{GPS}}$ for GPS and $\delta\check{t}_{2,\text{Galileo}}$ for Galileo using unambiguous ionosphere free phase-only combination $\lambda\check{\varphi}_{2,\text{IF}}^k$.

GPS fixed phase residuals are presented in Fig. 3.13. The float ambiguities at every epoch were averaged over all epochs processed and fixed to the resulting float values. After ambiguity fixing the drift of the residuals up to 3 cm/min is observed, that results from the accumulation of float ambiguities combined with unconsidered errors and biases with time and consequent low weight given to the new values.

To avoid such a case, a different approach of float ambiguity averaging over only last 200 epochs was used. The resulting GPS and Galileo fixed phase residuals are presented in Fig. 3.14 and Fig. 3.15. The GPS fixed phase residuals GPS are in order of ± 4 cm, while Galileo residuals are in the order of ± 1 cm. Galileo E1 and E5 signals possess a lower measurement noise and are less prone to multipath, that is beneficial for PPP without error compensation.

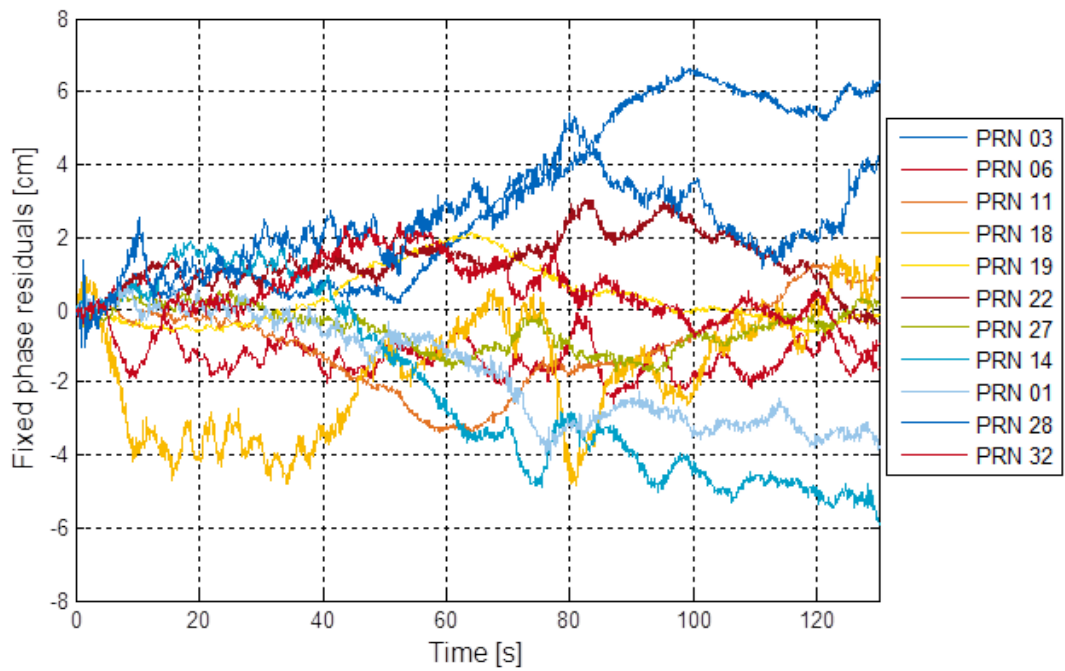


Figure 3.13: GPS fixed phase residuals with ambiguities averaged over all epochs

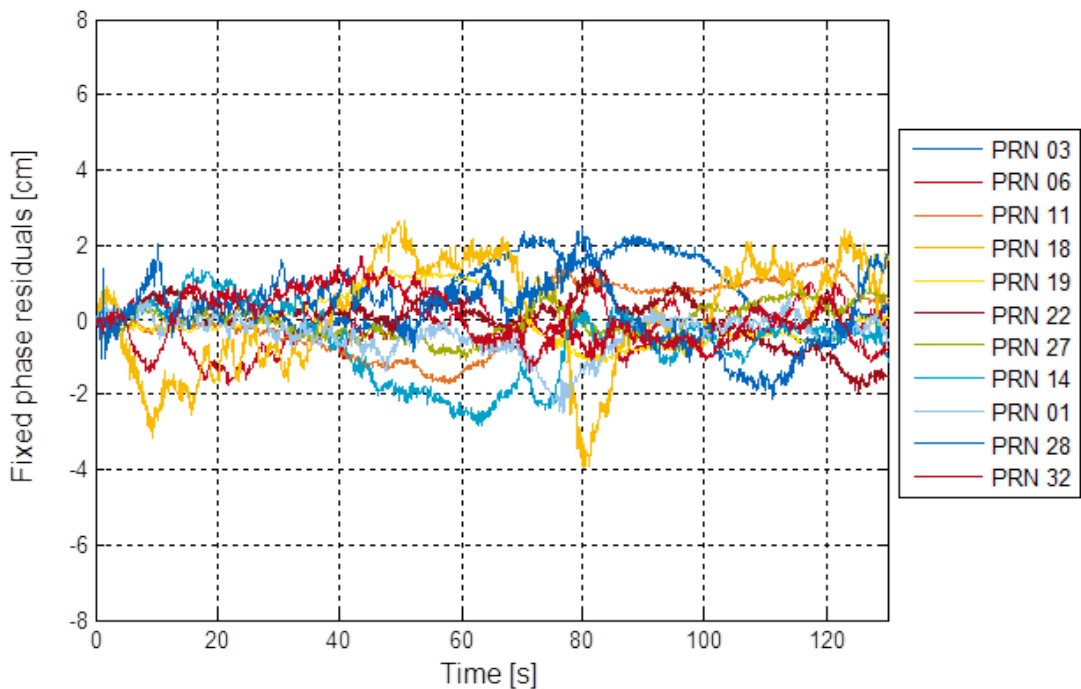


Figure 3.14: GPS fixed phase residuals with ambiguities averaged over last 200 epochs

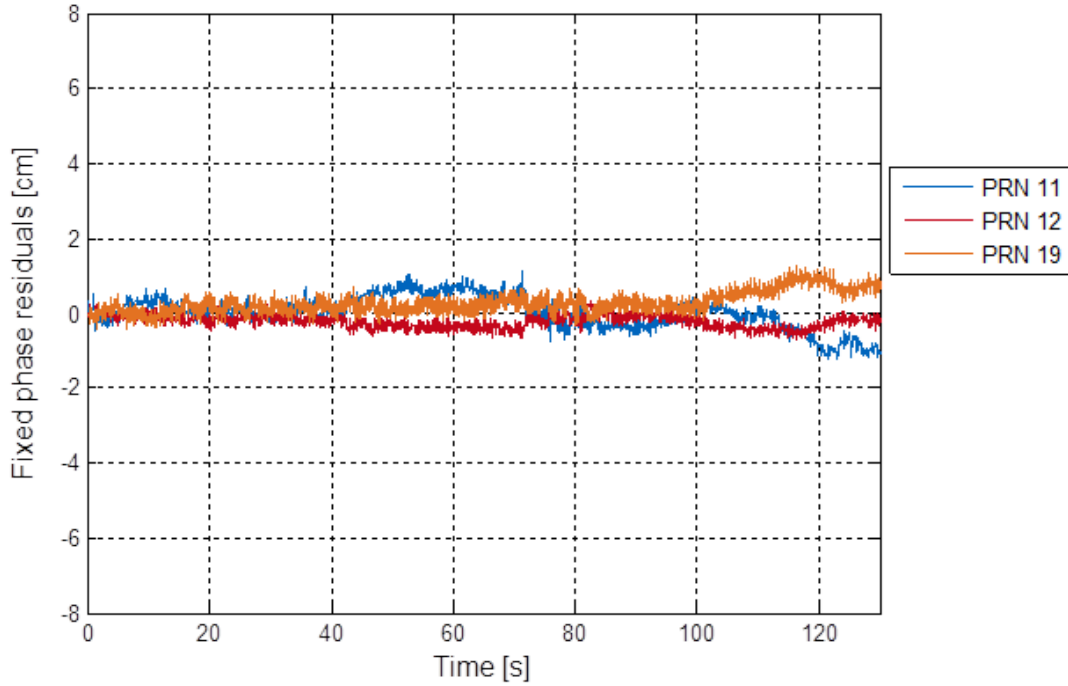


Figure 3.15: Galileo fixed phase residuals with ambiguities averaged over last 200 epochs

3.5 Joint subset optimization and integer least-squares estimation

Cycle slips are carrier phase jumps of $n \cdot \frac{\lambda}{2}$ caused by deep power fades due to multipath and/or signal shadowing that occurs for receivers moving in urban areas. For the real-time kinematic applications such as PPP and RTK instantaneous cycle slip detection and correction is required to reach the desired positioning accuracy. The subset of ambiguities with cycle slips, as well as the cycle slip values itself must be determined for the integer ambiguity fixing. As joint subset selection and integer least-squares estimation solely based on minimizing the Sum of Squared Errors (SSE) shows poor performance, a new approach is required.

We model time differences between code and carrier phase measurements of all visible satellites as:

$$\Psi = H\Delta\xi + A(s)\Delta N(s) + \eta, \quad (3.20)$$

with the geometry matrix H , change of the receiver position and receiver clock offset $\Delta\xi$ between two subsequent epochs, subset s of phase measurements being simultaneously affected by cycle slips, integer cycle slips $\Delta N(s)$ for the phase measurements of the subset and the mapping matrix $A(s)$ for the mapping of the ambiguity cycle slips into the measurement space as well as the mea-

surement noise η . The least-squares estimation of $\Delta\xi$, $\Delta N(s)$ and the subset s is given by:

$$\begin{aligned} & \min_{\Delta\xi, \Delta N(s), s} \|\Psi - H\Delta\xi - A(s)\Delta N(s)\|_{\Sigma_{\Psi}^{-1}}^2 = \\ & \min_s \left(\min_{\Delta\xi, \Delta N(s)} \|\Psi - H\Delta\xi - A(s)\Delta N(s)\|_{\Sigma_{\Psi}^{-1}}^2 \right) \end{aligned} \quad (3.21)$$

The minimization requires for each subset s a search for all integer candidate vectors inside a predefined search space volume χ^2 with integer decorrelation that fulfill the criterion [22]

$$\min_{\Delta\xi} \left(\|\Psi - H\Delta\xi - A(s)\Delta N(s)\|_{\Sigma_{\Psi}^{-1}}^2 \right) \leq \chi^2 \quad (3.22)$$

The subset and cycle slip values of minimum squared residuals are selected.

The squared error norm of (3.21) was decomposed by Teunissen in [22] into three orthogonal terms:

$$\begin{aligned} & \|\Psi - H\Delta\xi - A(s)\Delta N(s)\|_{\Sigma_{\Psi}^{-1}}^2 = \\ & \|\Delta\hat{N}(s) - \Delta N(s)\|_{\Sigma_{\hat{N}}^{-1}}^2 + \|\Delta\check{\xi}(\Delta N(s)) - \Delta\xi\|_{\Sigma_{\xi_{12}}^{-1}}^2 + \|P_{\bar{A}}^{\perp} P_H^{\perp} \Psi\|_{\Sigma_{\Psi}^{-1}}^2 \end{aligned} \quad (3.23)$$

where P_H^{\perp} is an orthogonal projector on the space of H and $\bar{A} = P_H^{\perp} A$ and the float solution of the cycle slips assuming subset s_i given by

$$\Delta\hat{N}(s_i) = ((\bar{A}(s_i))^T \Sigma_{\Psi}^{-1} \bar{A}(s_i))^{-1} (\bar{A}(s_i))^T \Sigma_{\Psi}^{-1} \Psi \quad (3.24)$$

The first term of (3.23) denotes cycle slip residuals, the second term velocity and clock drift residuals and the third term includes the irreducible noise. For sequential fixing, the probability of a wrong fixing can be derived analytically as:

$$P_{wf} = 1 - P_s = 1 - \prod_{k=1}^K \int_{-0.5}^{0.5} \frac{1}{\sqrt{2\pi\sigma_{\Delta\hat{N}^k|1,\dots,k-1}^2}} e^{-\frac{\varepsilon_{\Delta\hat{N}^k|1,\dots,k-1}^2}{2\sigma_{\Delta\hat{N}^k|1,\dots,k-1}^2}} d\varepsilon_{\Delta\hat{N}^k|1,\dots,k-1} \quad (3.25)$$

The minimum and maximum probabilities of wrong fixing over all subsets are shown in Fig. 3.16. Increase of subset length over 7 results in a considerable increase of minimum probability of wrong fixing among all subsets due to dependency on code measurements.

Applying the triangular LDL^T decomposition as defined in [22] to the first term gives:

$$\|\Delta\hat{N}(s) - \Delta N(s)\|_{\Sigma_{\hat{N}}^{-1}}^2 = \sum_{l=1}^K \left(\Delta N^l(s) - \Delta\hat{N}^{l|1,\dots,l-1}(s) \right)^2 / \sigma_{\Delta\hat{N}^{l|1,\dots,l-1}}^2 \quad (3.26)$$

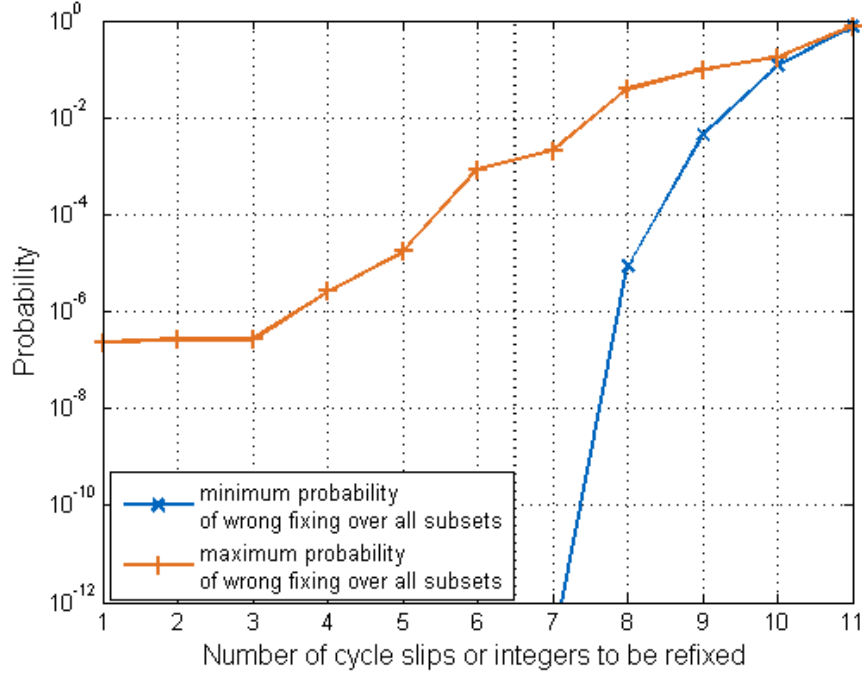


Figure 3.16: Probability of a wrong fixing over all subsets

where $\Delta\hat{N}^{l1,\dots,l-1}(s)$ is the float cycle slip and $\sigma_{\Delta\hat{N}^{l1,\dots,l-1}}^2$ is the variance of the float cycle slips. Combining (3.22), (3.23) and (3.26), the criterion of the integer search becomes

$$\begin{aligned} & \left(\Delta N_{12}^k(s) - \Delta\hat{N}_{12}^{k1,\dots,k-1}(s) \right)^2 / \sigma_{\Delta\hat{N}_{12}^{k1,\dots,k-1}}^2 \\ & \leq \chi^2 - \|P_{\bar{A}}^\perp P_H^\perp \Psi\|_{\Sigma_{\Psi}^{-1}}^2 - \sum_{l=1}^{k-1} \frac{\left(\Delta N_{12}^l(s) - \Delta\hat{N}_{12}^{l1,\dots,l-1}(s) \right)^2}{(\sigma_{\Delta\hat{N}_{12}^{l1,\dots,l-1}})^2} \end{aligned} \quad (3.27)$$

The statistics of the float solution are given by the bias $b_{\Delta\hat{N}(s_i)}$ and the covariance matrix $\Sigma_{\Delta\hat{N}(s_i)}$ that follows from (3.24), i.e.:

$$b_{\Delta\hat{N}(s_i)} = \left((\bar{A}(s_i))^T \Sigma_{\Psi}^{-1} \bar{A}(s_i) \right)^{-1} (\bar{A}(s_i))^T \Sigma_{\Psi}^{-1} A(\bar{s}) \Delta N(\bar{s}) - \Delta N \quad (3.28)$$

$$\Sigma_{\Delta\hat{N}(s_i)} = \left((\bar{A}(s_i))^T \Sigma_{\Psi}^{-1} \bar{A}(s_i) \right)^{-1} \quad (3.29)$$

Note that if the bias $b_{\Delta\hat{N}(s_i)}$ is close to an integer for $s_i \neq \bar{s}$, then it does not affect the sum of squared residuals given by

$$\min_{\Delta\xi, \Delta N(s_i)} \|\Psi - H\Delta\xi - A(s_i)\Delta N(s_i)\|_{\Sigma_{\Psi}^{-1}}^2 \quad (3.30)$$

As a consequence, the reliability of

$$\min_{\Delta\xi, \Delta N(s_i)} \|\Psi - H\Delta\xi - A(s_i)\Delta N(s_i)\|_{\Sigma_\Psi^{-1}}^2 \quad (3.31)$$

is then of comparable level to the reliability of

$$\min_{\Delta\xi, \Delta N(\bar{s})} \|\Psi - H\Delta\xi - A(\bar{s})\Delta N(\bar{s})\|_{\Sigma_\Psi^{-1}}^2 \quad (3.32)$$

If the ambiguities of a subset s_i refer to satellites of higher elevation than the ambiguities of \bar{s} , then it is likely to choose the wrong subset.

To solve this problem, we exploit that $\bar{A}(s_i) = P_H^\perp A(s_i)$ depends on the geometry matrix H and vary it by using subset of measurements. From a set of the measurements from K satellites available we exclude ones from the satellite l . Then the Sum of Squared Errors for each remaining subset s_i of ambiguities is given by:

$$\text{SSE}(s_i, l) = \min_{\Delta\xi} \|\Psi_{\forall k \setminus l} - H_{\forall k \setminus l} \Delta\xi - A_{\forall k \setminus l}(s_i) \Delta \check{N}(s_i)\|_{\Sigma_\Psi^{-1}}^2 \quad \forall l, \forall s_i \quad (3.33)$$

where the fixed integer cycle slip estimate is given by

$$\Delta \check{N}(s_i) = \min_{\Delta N(s_i)} \|P_H^\perp (\Psi - A(s_i) \Delta N(s_i))\|_{\Sigma_\Psi^{-1}}^2 \quad (3.34)$$

The selection of the final subset is based on the criteria

$$\check{s} = \min_{s_i} \left(\max_l (\text{SSE}(s_i, l)) \right) \quad (3.35)$$

The probability of wrong subset selection based on improved subset search is decreased in comparison to the search of subset based on minimum Sum of Squared Errors as shown in Fig. 3.17.

Using the new approach for ambiguity refixing after cycle slip occurs, the extended measurements collected within the long-baseline test by the mobile receiver were processed according to the algorithm described in Subsection 3.4.2. The estimated ambiguities together combined with phase biases are presented in Fig. 3.18.

To analyze the bias stability, maximum bias changes within the 5 min (Fig. 3.19), 1 min (Fig. 3.20) and 1 s (Fig. 3.21) were computed. The Fig. 3.21 demonstrates the stability of Galileo ionosphere-free phase biases over short time periods, i.e. a stability of 0.5 cm/s is achievable.

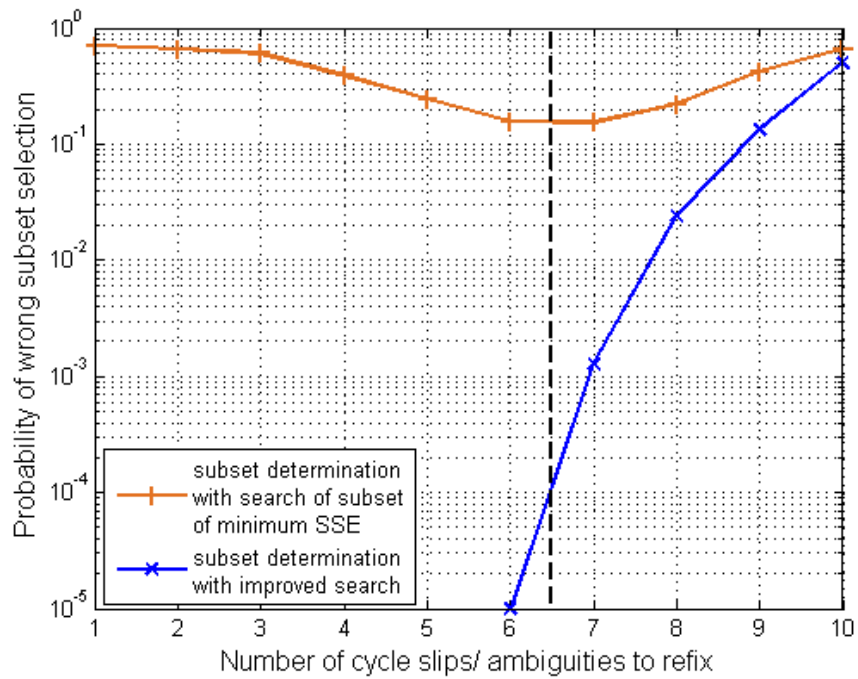


Figure 3.17: Probability of a wrong subset selection for two types of search

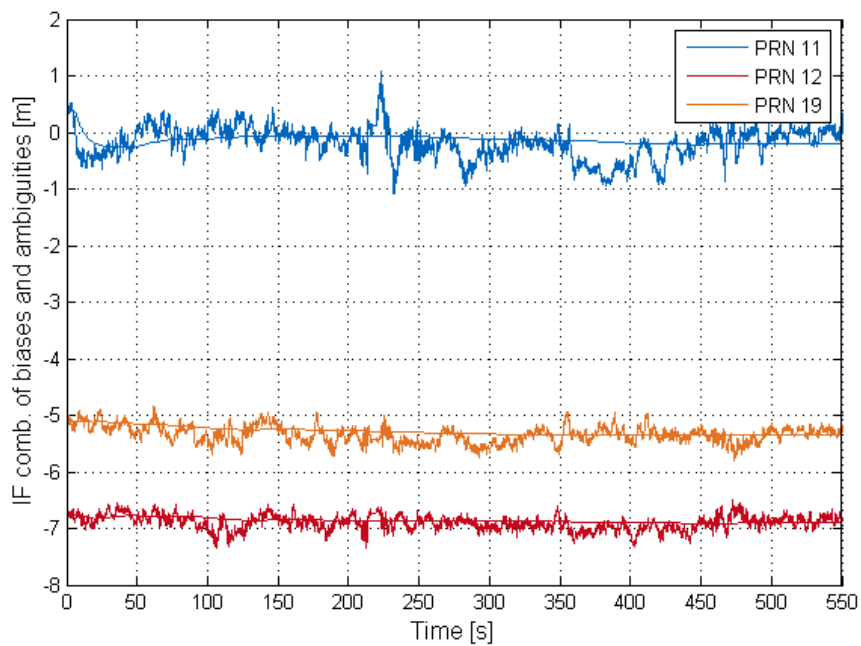


Figure 3.18: Galileo IF ambiguities and biases

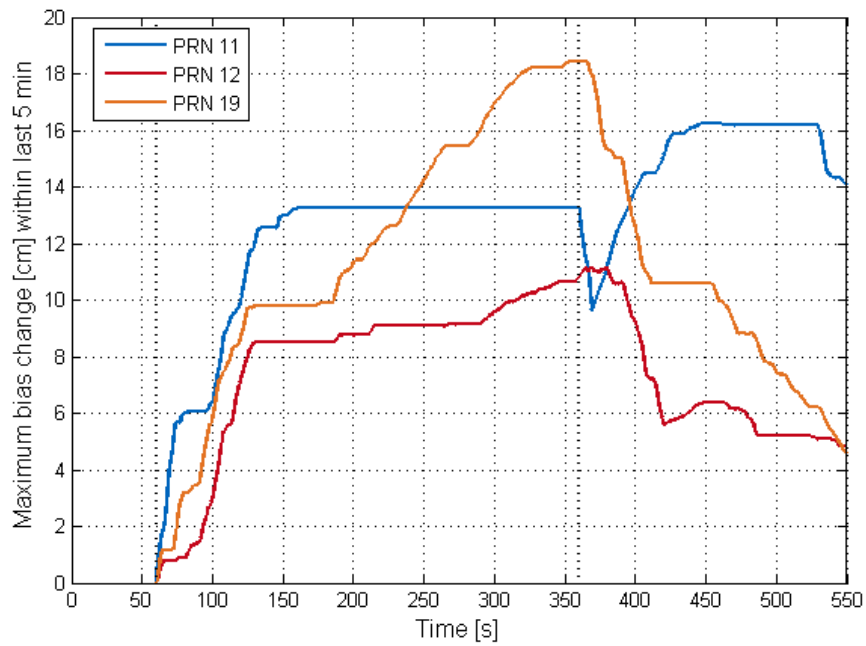


Figure 3.19: Maximum bias change within 5 min

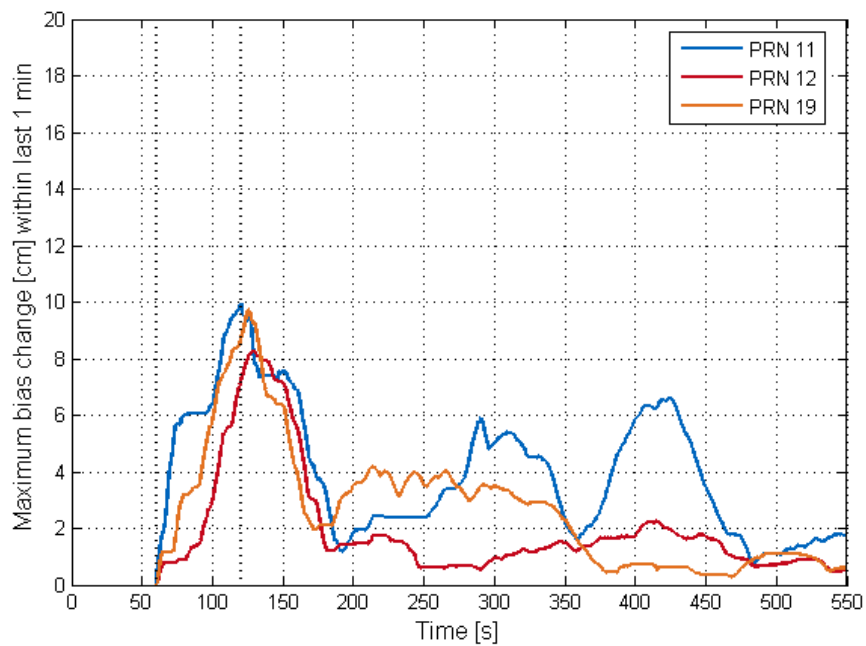


Figure 3.20: Maximum bias change within 1 min

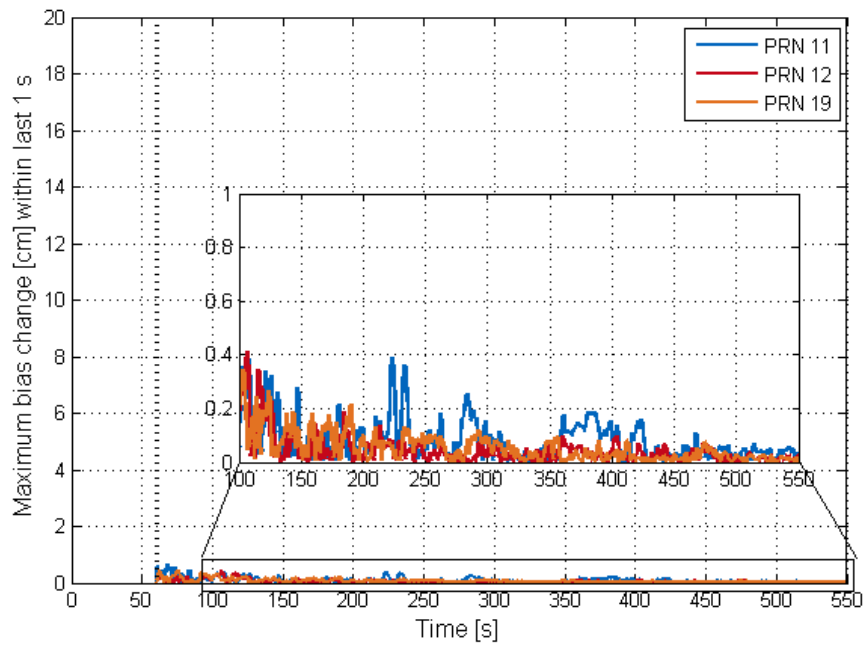


Figure 3.21: Maximum bias change within 1 sec

4. Absolute positioning with a system of low-cost GPS receivers

In this chapter a Virtual Reference Station concept is developed for a network of low-cost single-frequency GPS receivers. First, an introduction into Virtual Reference Station method is given. Then, the precise absolute position of the reference receiver r_1 is estimated using single-difference code and phase measurements in a Kalman filter with additional estimation of ambiguities, combined residual zenith ionospheric delays and corresponding ionospheric delay gradients. Subsequently, the relative position of receiver r_2 is determined using double-difference code and phase measurements (float solution) with consecutive ambiguity fixing with the classical LAMBDA method of Teunissen and least-squares fixed position estimation. The combined single-difference tropospheric and ionospheric errors, satellite biases as well as ambiguities for carrier phase measurements in form of corrections are derived from the single-difference code and phase measurements of both reference receivers and interpolated according to the model proposed. Finally, the method for the determination of the user receiver absolute position from corrected single-difference measurements is introduced.

4.1 The Virtual Reference Station method

The Virtual Reference Station method is based on having a network of GPS reference stations, at least three, connected via data links to a common network server. A computer at the control center continuously gathers the information from all the stations and creates a database of the corrections. These are used to create a Virtual Reference Station, located at the position of the user receiver, together with the reference data, which would have come from it. The user receiver interprets and uses the data just as if it has come from real reference station. The errors cancel out better than by using a more distant reference station, that dramatically improves performance of RTK [23]. This concept is visualized in Fig. 4.1.

The Virtual Reference Stations operation follows the following principles ([3] and [24]):

1. Pseudorange and carrier phase measurements from the reference station network are transferred to the control center, where they undergo quality control procedures.

This step includes station data integrity as well as differential integrity procedures. Station data integrity performs quality control procedures on pseudorange and carrier phase measurements

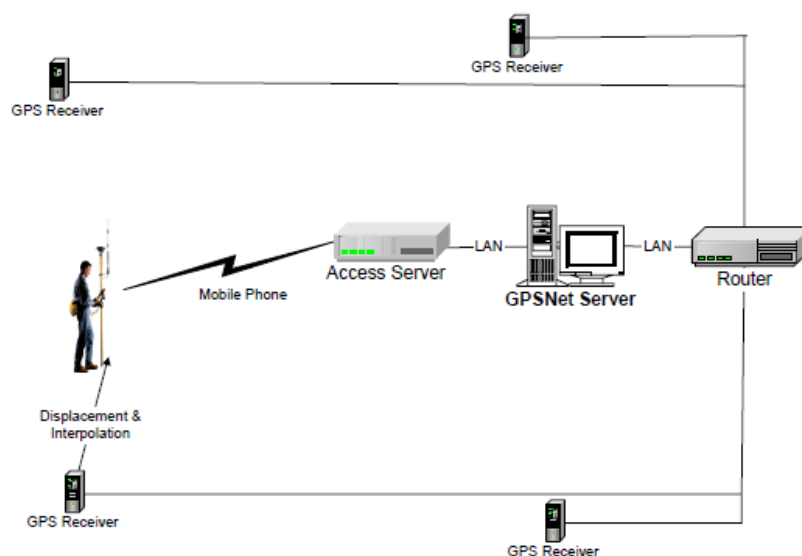


Figure 4.1: Virtual Reference Station set-up [3]

of *separate* stations. The estimator for the receiver clock error is used to identify outliers in the pseudorange observations. Potential cycle slips of carrier phase measurements are detected using the prediction of the observables for the current epoch estimated by especially designed Kalman filters. *Differential* integrity extends these procedures to the *single-difference* observables between two stations. The differential pseudorange observations are treated in the similar way, while carrier phase observations are crosschecked against cycle slips using triple differencing.

2. The undifferenced network data is used to compute models of ionospheric, geometric (tropospheric and orbit), as well as multipath errors. These models serve two purposes:
 - Provide error correction for DGPS users;
 - Reduce the data present in the measurements substantially to enable network ambiguity fixing.

For modeling of the ionospheric delay, a single layer model of the zenith ionospheric delay was chosen, which assumes that all active electron content of the atmosphere is concentrated on a layer with fixed height. The zenith delay at the pierce point and the elevation angle of the satellite define the total ionospheric delay. To model the zenith delay, simple 2-dimensional polynomials over geomagnetic latitude ϕ_{mag} and hour angle of the Sun λ_{sun} are used [24]:

$$TEC(\phi_{mag}, \lambda_{sun}) = \sum_{k=0}^N \sum_{i=0}^k A_{i,k} \phi_{mag}^i \lambda_{sun}^{k-i}, \quad (4.1)$$

where $A_{i,k}$ are polynomial coefficients. Temporary variations are modeled using Kalman filter. An order of 2 gives best result, allowing to remove about 50% of the ionospheric residual.

Tropospheric errors are handled by using models for the zenith delay and a mapping function to obtain a slant delay at a given satellite elevation angle. As existing low-cost tools cannot provide the desired accuracy of the measurements of meteorological conditions at the receiver site, the tropospheric scaling technique is used. All deviations of the atmospheric conditions from the standard conditions are expressed by a scaling factor of the zenith delay, one for each station. This factor is the troposphere model parameter. Zenith delays are estimated using modified Hopfield model. To mitigate orbit errors, precise predicted orbits and satellite clock corrections supplied e.g. by International GNSS service (IGS) are used. These are crosschecked with broadcast orbits. The influence of tropospheric scaling and orbit errors is modeled based on the satellite-receiver geometry as follows [24]:

$$\lambda(\phi_{r,C}^k + N_C^k) = r_r^k + c(\delta\tau_r - \delta\tau^k) + \gamma_r m(\theta_r^k) T_{z,r} + \frac{\Delta\vec{X}^k \cdot \vec{r}_r^k}{r_r^k} + \epsilon_r^k \quad (4.2)$$

with the carrier wavelength λ , ionosphere-free carrier phase observations $\phi_{r,C}^k$ computed according to Eq. (2.17), the integer ambiguity N_C^k , the satellite-receiver geometric range r_r^k , the speed of light in vacuum c , the receiver clock offset $\delta\tau_r$, the satellite clock offset $\delta\tau^k$, the receiver tropospheric scaling factor γ_r , the troposphere model value $m(\theta_r^k)T_{z,r}$, the satellite position error $\Delta\vec{X}^k$, the vector pointing from the satellite to receiver \vec{r}_r^k and the phase noise ϵ_r^k . As the reference station position is known, the tropospheric scaling, the orbit errors as well as the ambiguities for each satellite are estimated with the Kalman filter using ionosphere-free observations. For the multipath error modeling, the repeatability of multipath effects is exploited on a day-to-day basis.

3. In a third step, double-difference measurements are re-considered with the aim of fixing their ambiguities. Two linear combinations of double-differences are considered: the first one is geometry-preserving and ionosphere-free; the second one is geometry-free. The previously determined orbital errors and tropospheric scaling factors are used to correct the first combination (relevant only in case of long baselines). The previously determined ionospheric corrections are used to correct the second combination. The ambiguities N_I of geometry-preserving combination and N_C of geometry-free combination can be related to the ambiguities of the absolute L1-L2 measurements by [24]:

$$\begin{pmatrix} N_C \\ N_I \end{pmatrix} = \underbrace{\begin{pmatrix} \alpha_1 & \alpha_2 \\ -\lambda_1 \cdot \frac{\lambda_2^2 - \lambda_1^2}{\lambda_1^2} & \lambda_2 \cdot \frac{\lambda_2^2 - \lambda_1^2}{\lambda_1^2} \end{pmatrix}}_T \begin{pmatrix} N_{L1} \\ N_{L2} \end{pmatrix} \quad (4.3)$$

Inverting the conversion matrix T leads to the form [24]:

$$\begin{pmatrix} N_{L1} \\ N_{L2} \end{pmatrix} = T^{-1} \begin{pmatrix} N_C \\ N_I \end{pmatrix} \quad (4.4)$$

The covariance matrix of the N_{L1}/N_{L2} ambiguities is given as the function of covariance matrix of the N_I/N_C ambiguities by:

$$\Sigma_{\hat{N}_{L1}, \hat{N}_{L2}} = T^{-1} \Sigma_{(\hat{N}_C, \hat{N}_I)} (T^{-1})^T \quad (4.5)$$

4. In this step, the residuals of the double-difference ambiguity resolution are determined, i.e.

$$C_{12,m}^{kl} = \lambda_m \varphi_m^{kl} - \lambda_m \check{N}_{12,m}^{kl} - \vec{e}_{12}^{*kl} \check{b}_{12} \quad (4.6)$$

where \check{b}_{12} is the baseline vector between two reference stations. It is either known from the absolute positions of the reference stations or determined by the LAMBDA method.

5. In the next step "linear" 2-dimensional error models are used to interpolate the double-difference residuals at the location of the Virtual Reference Station.

Vollath et al. [24] used the three closest reference receivers to set up a linear model for the double-difference residuals within the triangle (Fig. 4.2).

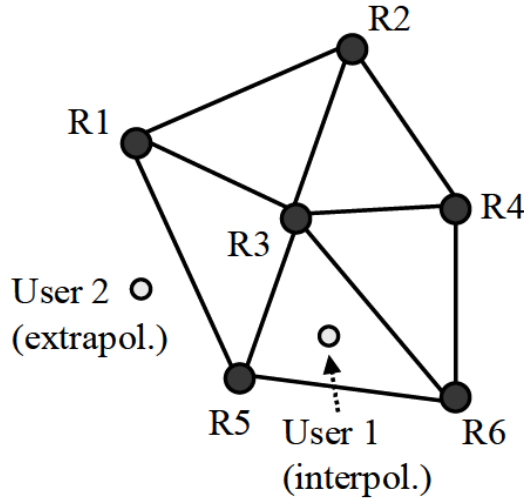


Figure 4.2: Interpolation and extrapolation of the differential residuals [24]

Choosing one station of a triangle as pivotal station with coordinates (ϕ_r, λ_r) , the double-difference residuals between any pair of satellites k and l is interpolated (or extrapolated) to the Virtual Reference Station location with coordinates (ϕ_v, λ_v) as [24]:

$$C_{vr,m}^{kl}(\phi_v, \lambda_v) = \frac{\partial C_m^{kl}}{\partial \phi} (\phi_v - \phi_r) - \frac{\partial C_m^{kl}}{\partial \lambda} (\lambda_v - \lambda_r) \cos(\phi_r) \quad (4.7)$$

The interpolation parameters for the latitude $\frac{\partial C_m^{kl}}{\partial \phi}$ and for the longitude $\frac{\partial C_m^{kl}}{\partial \lambda}$ are uniquely determined by the double-difference corrections/residuals to the other two stations of the triangle (ϕ_1, λ_1) and (ϕ_2, λ_2) , i.e. [24]:

$$C_{1r,m}^{kl}(\phi_1, \lambda_1) = \frac{\partial C_m^{kl}}{\partial \phi}(\phi_1 - \phi_r) - \frac{\partial C_m^{kl}}{\partial \lambda}(\lambda_1 - \lambda_r)\cos(\phi_r) \quad (4.8)$$

$$C_{2r,m}^{kl}(\phi_2, \lambda_2) = \frac{\partial C_m^{kl}}{\partial \phi}(\phi_2 - \phi_r) - \frac{\partial C_m^{kl}}{\partial \lambda}(\lambda_2 - \lambda_r)\cos(\phi_r) \quad (4.9)$$

The trigonometric function $\cos(\phi_r)$ was added to consider the unequal spacing of meridians at the different degrees of latitude. The quality of the interpolated residuals is determined by the actual linearity of the residuals over space.

6. On the sixth step the raw measurements of selected reference station, used by the user receiver in the next step to form double differences, are geometrically displaced to the position of the Virtual Reference Station. Typically the station nearest to the field user is chosen.

All parts of observation equations that depend on the receiver location have to be corrected to the position of the Virtual Reference Station. The geometric range at the reception time t between satellite k and Virtual Reference Station v is approximated as [24]:

$$\tilde{r}_v^k(t) = \sqrt{(\vec{x}^k - \vec{x}_v)^T \cdot (\vec{x}^k - \vec{x}_v)}, \quad (4.10)$$

where \vec{x}^k is the satellite position at the transmission time and \vec{x}_v is the position of the Virtual Reference Station at the reception time. During the calculation of the satellite position the rotation of the Earth during the signal transmission, as well as change of the signal transmission time due to the receiver position change still has to be accounted for. Therefore the geometric range \tilde{r}_v^k is accurate only on a meter level. Using the range approximation (4.10), the approximate pseudorange between the satellite k and Virtual Reference Station v is given by [24]:

$$\tilde{\rho}_v^k = \rho_r^k + (\tilde{r}_v^k - r_r^k), \quad (4.11)$$

where ρ_r^k is the pseudorange between satellite k and the original reference station r , \tilde{r}_v^k is the approximate geometric range between satellite k and the Virtual Reference Station v and r_r^k is the exact geometric range between satellite k and the reference station r . This pseudorange approximation is used to determine the exact satellite position as well as exact geometric range r_v^k . Finally, the change in the geometric range between the original reference station r and Virtual Reference Station v is computed, i.e. [24]:

$$\Delta r_v^k = r_v^k - r_r^k \quad (4.12)$$

It has to be applied to all observables to displace the reference station measurements to the Virtual Reference Station position.

7. Finally, the Virtual Reference Station data in terms of displaced code and phase measurements as well as interpolated double-difference residuals are transferred to the user.

On a typical field session, the following set-up procedure is performed ([3] and [24]):

1. After starting the receiver in real-time positioning mode, the user dials into the Virtual Reference Station Network service via mobile phone and is authenticated.
2. The local receiver sends a navigation solution of its current position as a rough position estimate to the computing center.
3. The computing center creates a Virtual Reference Station at this location.
4. A continuous data stream of reference data generated for the Virtual Reference Station position is sent to the field user receiver, that computes double-difference measurements and applies corrections provided to fix the integer ambiguities and determine its position with a centimeter level accuracy.

4.2 Least-squares float solution of absolute position of a reference receiver

To provide the corrections for the user receiver, first the 3-dimensional position \vec{x}_{r_1} of the first reference receiver r_1 must be estimated. It can be determined using single-frequency precise carrier phase measurements from K satellites visible at a certain epoch. We consider only satellites with elevation angle θ over 20° . Choosing satellite 1 as reference, we can form $K-1$ respective single differences to eliminate unknown receiver clock offset and receiver biases. The single-difference carrier phase measurements modeled according to equation (2.1) are rearranged in such a way that all known parameters (satellite positions and clock offsets, tropospheric delays) are brought on the left side of the equation and unknown parameters on the right side, i.e.

$$\begin{pmatrix} \lambda\varphi_{r_1}^{12} + (\vec{e}_{r_1}^{12})^T \hat{\vec{x}}^{12} + c\delta\hat{\tau}^{12} - \hat{T}_{r_1}^{12} \\ \vdots \\ \lambda\varphi_{r_1}^{1K} + (\vec{e}_{r_1}^{1K})^T \hat{\vec{x}}^{1K} + c\delta\hat{\tau}^{1K} - \hat{T}_{r_1}^{1K} \end{pmatrix} = \begin{pmatrix} (\vec{e}_{r_1}^1)^T \\ \vdots \\ (\vec{e}_{r_1}^K)^T \end{pmatrix} \vec{x}_{r_1} + \begin{pmatrix} I_{r_1}^{12} \\ \vdots \\ I_{r_1}^{1K} \end{pmatrix} + \lambda \begin{pmatrix} N_{r_1}^{12} + \beta^{12} \\ \vdots \\ N_{r_1}^{1K} + \beta^{1K} \end{pmatrix} + \begin{pmatrix} \varepsilon^{12} \\ \vdots \\ \varepsilon^{1K} \end{pmatrix}, \quad (4.13)$$

where phase noise includes multipath.

To reach the desired accuracy of absolute positioning, ultra-rapid satellite orbits and clock offsets (predicted half) provided in a real time by the International GNSS Service are used. The orbits provided have an accuracy of ~ 5 cm, clocks have RMS of ~ 3 ns and standard deviation of ~ 1.5 ns.

The multipath error affects the measurements differently for each satellite and frequency and its estimation is in general not feasible due to singularity problems. However, multipath errors repeat with the satellite geometry in case the receiver is stationary and its environment does not change. The repeatability of multipath can be exploited at the reference stations equipped with geodetic receivers, as it can be separated from all other error terms and estimated from the residuals. Averaging the residuals over N epochs with equal satellite geometries is also called sidereal filtering and yields the multipath estimate as given by [5]:

$$\hat{\delta}_{r,m}^k = \frac{1}{N} \sum_{i=1}^N \left(\tilde{\rho}_{u,m}^k(t_n + i\Delta t) - \Delta \hat{g}_u^k(t_n + i\Delta t) - q_{1m}^2 \hat{I}_u^k(t_n + i\Delta t) \right), \quad (4.14)$$

where $\Delta t = 11 \text{ h } 58 \text{ min}$ for GPS is the time interval between two equal satellite geometries. The estimates of the geometry terms \hat{g}_u and ionospheric delays \hat{I}_u^k can be obtained from a Kalman filter, that jointly processes code $\tilde{\rho}$ and phase $\lambda\tilde{\varphi}$ measurements. In addition, the estimates the phase biases and integer ambiguities as float numbers are obtained. For the low-cost systems multipath estimation and elimination still remains a research problem.

The remaining main error sources are tropospheric and ionospheric delays, which are estimated and mitigated as described in the following subsections.

4.2.1 Modeling of tropospheric delay using the MOPS model

We determine the tropospheric delay in two steps as described by Misra et al. [4]:

1. Estimation of the zenith delay \hat{T}_z in terms of corresponding hydrostatic (dry delay) $\hat{T}_{z,dry}$ and non-hydrostatic (wet delay) $\hat{T}_{z,wet}$ terms, i.e.

$$\hat{T}_z = \hat{T}_{z,dry} + \hat{T}_{z,wet} \quad (4.15)$$

Note that tropospheric zenith delay depends only on receiver's location and are the same for all satellites tracked.

2. Determination of mapping function, the obliquity factor to scale the zenith delay as a function of elevation angle θ of the satellite. Final tropospheric delay is calculated as:

$$\hat{T}_r = \hat{T}_{z,dry} m_{dry}(\theta) + \hat{T}_{z,wet} m_{wet}(\theta) \quad (4.16)$$

Estimation of tropospheric delays from GNSS data requires collection of observations during 1-2 h and therefore cannot be used for kinematic applications. For geodetic applications, more accurate but more complex tropospheric delay models, e.g. Saastamoinen, Hopfield [4], are used. As input they require ground meteorological data, being their accuracy affected by the quality of these data. In navigation applications such data is often not available, and estimation of tropospheric delays is often based upon average meteorological conditions at user's locations obtained from a model of the standard atmosphere (so-called *blind model*) for the day-of-a-year (DOY) and corresponding latitude and altitude. Comparison of different data-driven and blind models was performed by Hornbostel and Hoque [25]. The result is shown in Fig. 4.3.

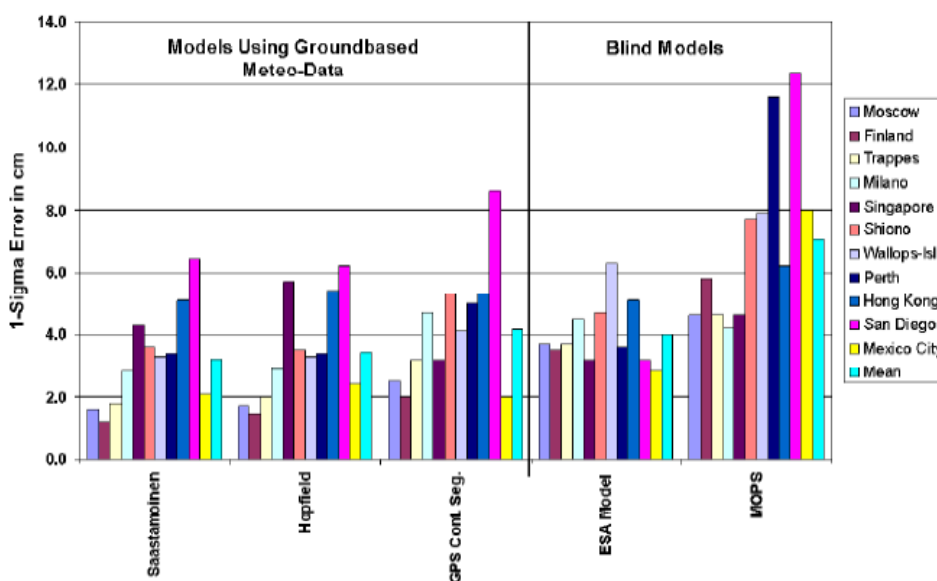


Figure 4.3: Comparison of different models for the tropospheric delay [25]

The Wide Area Augmentation System (WAAS) Minimum Operational Performance Standards (MOPS) blind model for tropospheric delay was chosen as it is computationally simple, which is important for real-time implementation, and delivers a relatively good accuracy with average residual 1- σ error for tropospheric vertical delay estimate of 12 cm [26]. This model provides estimates of the zenith tropospheric dry and wet delays for receiver's latitude ϕ and day-of-a-year D from the annual averages and associated seasonal variations of surface reference values of five meteorological parameters - namely, pressure P , temperature T , temperature lapse rate β , water vapor pressure e and water vapor lapse rate λ . They are derived primarily from North American meteorological data and provided with 15° latitude resolution in a look-up table. For receiver's latitudes $|\phi| \leq 15^\circ$ and $|\phi| \geq 75^\circ$ the average ξ_0 and seasonal variation $\Delta\xi$ values of meteorological parameters are taken directly from the look-up table provided in [26]. For latitudes $15^\circ < |\phi| < 75^\circ$ they are computed by linear interpolation between values of two closest latitudes

ϕ_l and ϕ_{l-1} in order to account for the strong north-south gradient of wet delay [27], i.e.

$$\xi_0(\phi) = \xi_0(\phi_l) + [\xi_0(\phi_{l+1}) - \xi_0(\phi_l)] \frac{(\phi - \phi_l)}{(\phi_{l+1} - \phi_l)} \quad (4.17)$$

$$\Delta\xi(\phi) = \Delta\xi(\phi_l) + [\Delta\xi(\phi_{l+1}) - \Delta\xi(\phi_l)] \frac{(\phi - \phi_l)}{(\phi_{l+1} - \phi_l)} \quad (4.18)$$

Seasonal variation value is multiplied by a cosine function in order to account for harmonic seasonal trend [27]. Thus, each of the five parameters ξ is calculated as follows:

$$\xi(\phi, D) = \xi_0(\phi) - \Delta\xi(\phi) \cos\left(\frac{2\pi(D - D_{min})}{365.25}\right), \quad (4.19)$$

where $D_{min} = 28$ for northern latitudes, $D_{min} = 211$ for southern latitudes.

Zero-altitude zenith dry and wet delay terms are given by:

$$z_{0,dry} = \frac{10^{-6} k_1 R_d P}{g_m} \quad (4.20)$$

$$z_{0,wet} = \frac{10^{-6} k_2 R_d e}{g_m(\lambda + 1) - \beta R_d T}, \quad (4.21)$$

where $k_1 = 77,604$ K/mbar and $k_2 = 382000$ K²/mbar are refractivity constants, $R_d = 287,054$ J/kg/K is gas constant for dry air and $g_m = 9,784$ m/s² is acceleration of gravity at the atmospheric column centroid.

Finally, a height reduction to the the receiver's height H is performed:

$$z_{dry} = \left(1 - \frac{\beta H}{T}\right)^{\frac{g}{R_d \beta}} z_{0,dry} \quad (4.22)$$

$$z_{wet} = \left(1 - \frac{\beta H}{T}\right)^{\frac{(\lambda+1)g}{R_d \beta} - 1} z_{0,wet}, \quad (4.23)$$

where $g = 9.80665$ m/s² is surface acceleration of gravity and H is expressed in units of meters above mean-sea-level.

Once zenith dry and wet delays at receiver's altitude are determined, the mapping function of Niell is applied to scale the zenith delay to the direction of observation. It does not require surface meteorological data as input, but provides precision and accuracy comparable to others that require such measurements. Katsougiannopoulos et al. [28] found out that its accuracy is at millimeter level for elevations above above 30° and better than 2 cm for elevations above 20°.

Niell mapping function is based on three term continued fraction of $\sin(\theta)$ satellite elevation angle as described by Marini [29] and normalized to unity at zenith by Herring [30], i.e.

$$m(\theta, a, b, c) = \frac{1 + \frac{a}{b}}{1 + \frac{a}{1+c}} \frac{1}{\sin(\theta) + \frac{a}{\sin(\theta) + \frac{b}{\sin(\theta) + c}}} \quad (4.24)$$

Niell hydrostatic mapping function m_{dry} depends on the receiver's latitude ϕ and height above the mean-sea-level H (given in units of km), day-of-a-year D and satellite elevation angle θ and is given by [31]:

$$m_{dry}(\theta, H) = m(\theta, a_h, b_h, c_h) - H\left(\frac{1}{\sin(\theta)} - m(\theta, a_{ht}, b_{ht}, c_{ht})\right) \quad (4.25)$$

The hydrostatic coefficients a_h , b_h and c_h are calculated according to Eq. (4.19), where $D_{min} = 28$. Coefficients average ξ_0 and amplitude $\Delta\xi$ values for receiver's latitudes $15^\circ < |\phi| < 75^\circ$ are linearly interpolated between values of two closest latitudes ϕ_l and ϕ_{l-1} provided in the look-up table as shown in Eq. (4.17) and Eq. (4.18). For the other latitudes these values, are taken directly from the table. The height correction coefficients a_{ht} , b_{ht} and c_{ht} are constant over latitude and provided in the same table.

Niell wet mapping function m_{wet} depends only on the receiver's latitude and satellite elevation angle as follows [31]:

$$m_{wet}(\theta) = m(\theta, a_w, b_w, c_w) \quad (4.26)$$

The wet coefficients a_w , b_w and c_w are linearly interpolated between values of two closest latitudes ϕ_l and ϕ_{l-1} provided in the look-up table.

4.2.2 Estimation of a receiver position, carrier phase ambiguities and residual ionospheric delays

Given measurements on at least two frequencies, ionospheric delays can be eliminated by forming ionosphere-free combination or estimated. For the low-cost receivers, that provide measurements only on one frequency, other methods have to be used. Assuming the single layer ionosphere model, we estimate the ionospheric delays \hat{I}^k using Klobuchar model [32] and correct the raw measurements with obtained estimates. As the model can only correct 50-60% RMS of the ionospheric range delay in practice, we proceed by estimating the delays for each satellite along with a 3-dimensional receiver position and single-difference ambiguities in order to achieve desired decimeter-level absolute positioning accuracy. Therefore, there will be $3+2 \cdot (K - 1)$ independent unknowns in a system of equations (4.13), that makes it under-determined. To avoid such a case, carrier phase measurements from N_{ep} multiple epochs are used. However, the residual ionospheric delay for each satellite in this case would have to be estimated for each epoch. To avoid that, the residual delay for each satellite k at the time t_n is represented in terms of the residual zenith delay $\Delta I_{z,r}^k$ at the time t_0 and corresponding gradient $\frac{\partial}{\partial t} \Delta I_{z,r}^k$ at the time t_n , as well as elevation

dependent mapping function m_I^k :

$$\begin{aligned}\Delta I_r^k(t_n) &= m_I^k \cdot (\Delta I_{z,r}^k(t_0) + (t_n - t_0) \cdot \frac{\partial}{\partial t} \Delta I_{z,r}^k) \\ &= m_I^k \cdot (\Delta I_{z,r}^k(t_0) + \Delta t \cdot \frac{\partial}{\partial t} \Delta I_{z,r}^k)\end{aligned}\quad (4.27)$$

Assuming the constant residual ionospheric delay gradient for each satellite, there will be finally $3+3 \cdot (K-1)$ independent unknowns. Note that, as Günther specified in [7], the phase measurements have to be sufficiently spaced in time to ensure linear independence. In order to limit the observation time needed to solve for the reference receiver position, we use more noisy but unambiguous code measurements $\rho_{r_1}^k$ in addition. Taking into account outlined assumptions, the following system of equations can be written for each epoch t_n :

$$\begin{aligned}& \begin{pmatrix} \lambda \varphi_{r_1}^{12} + (\vec{e}_{r_1}^{12})^T \hat{x}^{12} + c\delta\tau^{12} - \hat{T}_{r_1}^{12} + \hat{I}_{r_1}^{12} \\ \vdots \\ \lambda \varphi_{r_1}^{1K} + (\vec{e}_{r_1}^{1K})^T \hat{x}^{1K} + c\delta\tau^{1K} - \hat{T}_{r_1}^{1K} + \hat{I}_{r_1}^{1K} \\ \frac{\rho_{r_1}^{12} + (\vec{e}_{r_1}^{12})^T \hat{x}^{12} + c\delta\tau^{12} - \hat{T}_{r_1}^{12} - \hat{I}_{r_1}^{12} - b_{\text{DCB}}^{12}}{\rho_{r_1}^{12} + (\vec{e}_{r_1}^{12})^T \hat{x}^{12} + c\delta\tau^{12} - \hat{T}_{r_1}^{12} - \hat{I}_{r_1}^{12} - b_{\text{DCB}}^{12}} \\ \vdots \\ \frac{\rho_{r_1}^{1K} + (\vec{e}_{r_1}^{1K})^T \hat{x}^{1K} + c\delta\tau^{1K} - \hat{T}_{r_1}^{1K} - \hat{I}_{r_1}^{1K} - b_{\text{DCB}}^{1K}}{\rho_{r_1}^{1K} + (\vec{e}_{r_1}^{1K})^T \hat{x}^{1K} + c\delta\tau^{1K} - \hat{T}_{r_1}^{1K} - \hat{I}_{r_1}^{1K} - b_{\text{DCB}}^{1K}} \end{pmatrix} = \begin{pmatrix} (\vec{e}_{r_1}^{12})^T \\ \vdots \\ (\vec{e}_{r_1}^{1K})^T \\ (\vec{e}_{r_1}^{12})^T \\ \vdots \\ (\vec{e}_{r_1}^{1K})^T \end{pmatrix} \vec{x}_{r_1} \\ & + \begin{pmatrix} \lambda & 0 & 0 \\ \vdots & \ddots & \vdots \\ 0 & 0 & \lambda \\ 0 & \dots & 0 \\ \vdots & \ddots & \vdots \\ 0 & \dots & 0 \end{pmatrix} \begin{pmatrix} N_{r_1}^{12} + \beta_{r_1}^{12} \\ \vdots \\ N_{r_1}^{1K} + \beta_{r_1}^{1K} \end{pmatrix} + \begin{pmatrix} -m_I^1 & m_I^2 & 0 & 0 & 0 \\ -m_I^1 & 0 & m_I^3 & 0 & 0 \\ \vdots & 0 & 0 & \ddots & 0 \\ -m_I^1 & 0 & 0 & 0 & m_I^K \\ m_I^1 & -m_I^2 & 0 & 0 & 0 \\ m_I^1 & 0 & -m_I^3 & 0 & 0 \\ \vdots & 0 & 0 & \ddots & 0 \\ m_I^1 & 0 & 0 & 0 & -m_I^K \end{pmatrix} \begin{pmatrix} \Delta I_{z,r_1}^1(t_0) \\ \Delta I_{z,r_1}^2(t_0) \\ \vdots \\ \Delta I_{z,r_1}^K(t_0) \end{pmatrix} \\ & + \begin{pmatrix} -\Delta t_n m_I^1 & \Delta t_n m_I^2 & 0 & 0 & 0 \\ -\Delta t_n m_I^1 & 0 & \Delta t_n m_I^3 & 0 & 0 \\ \vdots & 0 & 0 & \ddots & 0 \\ -\Delta t_n m_I^1 & 0 & 0 & 0 & \Delta t_n m_I^K \\ \Delta t_n m_I^1 & -\Delta t_n m_I^2 & 0 & 0 & 0 \\ \Delta t_n m_I^1 & 0 & -\Delta t_n m_I^3 & 0 & 0 \\ \vdots & 0 & 0 & \ddots & 0 \\ \Delta t_n m_I^1 & 0 & 0 & 0 & -\Delta t_n m_I^K \end{pmatrix} \begin{pmatrix} \frac{\partial}{\partial t} \Delta I_{z,r_1}^1 \\ \frac{\partial}{\partial t} \Delta I_{z,r_1}^2 \\ \vdots \\ \frac{\partial}{\partial t} \Delta I_{z,r_1}^K \end{pmatrix} + \begin{pmatrix} \varepsilon_{r_1}^{12} \\ \vdots \\ \frac{\varepsilon_{r_1}^{1K}}{\eta_{r_1}^{12}} \\ \vdots \\ \eta_{r_1}^{1K} \end{pmatrix}, \quad (4.28)\end{aligned}$$

where the mapping function of the following form is used [7]:

$$m_1(\theta) = \frac{1}{\sqrt{1 - \frac{\sin^2 \zeta}{(1+h/R_e)^2}}} \quad (4.29)$$

with ionosphere reference height $h=350$ km above the Earth surface where all electrons are assumed to be accumulated (single layer model), radius of the Earth $R_e= 6378.1$ km and the zenith angle $\zeta = \theta - 90^\circ$ (see Fig. 4.4).

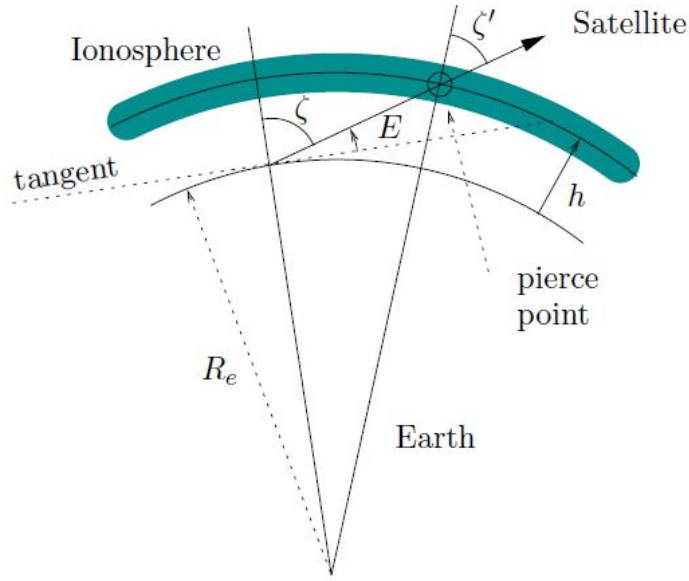


Figure 4.4: Geometry of ionospheric propagation [7]

For single frequency users, the satellites broadcast in their navigation messages the Timing Group Delay or Total Group Delay (TGD), which is proportional to the Differential Code Bias (DCB), or interfrequency bias. The code measurements have to be corrected for the DCB to reach decimeter level positioning accuracy. Among the navigation message, DCBs are also provided by IGS centers. We use the DCBs provided for each satellite by Center for Orbit Determination in Europe (CODE) on a monthly basis.

In this system of equations one column is linearly dependent on the others. Therefore it's not possible to solve for all zenith ionospheric delays and gradients independently using only single-frequency measurements. To be able to still estimate the residuals delays, we combine the residual zenith ionospheric delay $\Delta I_{z,r_1}^2$ with the other delays as follows:

$$\begin{pmatrix} -m_I^1 & m_I^2 & 0 & 0 & 0 \\ -m_I^1 & 0 & m_I^3 & 0 & 0 \\ \vdots & 0 & 0 & \ddots & 0 \\ -m_I^1 & 0 & 0 & 0 & m_I^K \\ \hline m_I^1 & -m_I^2 & 0 & 0 & 0 \\ m_I^1 & 0 & -m_I^3 & 0 & 0 \\ \vdots & 0 & 0 & \ddots & 0 \\ m_I^1 & 0 & 0 & 0 & -m_I^K \end{pmatrix} \begin{pmatrix} \Delta I_{z,r_1}^1(t_0) \\ \Delta I_{z,r_1}^2(t_0) \\ \vdots \\ \Delta I_{z,r_1}^K(t_0) \end{pmatrix} = \underbrace{\begin{pmatrix} -m_I^1 & 0 & 0 & 0 \\ -m_I^1 & -m_I^3 & 0 & 0 \\ \vdots & 0 & \ddots & 0 \\ -m_I^1 & 0 & 0 & -m_I^K \\ \hline m_I^1 & 0 & 0 & 0 \\ m_I^1 & m_I^3 & 0 & 0 \\ \vdots & 0 & \ddots & 0 \\ m_I^1 & 0 & 0 & m_I^K \end{pmatrix}}_{M_{I,c}} \begin{pmatrix} \Delta I_{z,r_1}^1(t_0) - \frac{m_I^2}{m_I^1} \Delta I_{z,r_1}^2(t_0) \\ \frac{m_I^2}{m_I^3} \Delta I_{z,r_1}^2(t_0) - \Delta I_{z,r_1}^3(t_0) \\ \vdots \\ \frac{m_I^2}{m_I^K} \Delta I_{z,r_1}^2(t_0) - \Delta I_{z,r_1}^K(t_0) \end{pmatrix}$$

where $M_{I,c} = \begin{pmatrix} M_{I,\varphi} \\ M_{I,\rho} \end{pmatrix}$ is the mapping matrix of the residual combined zenith ionospheric delays. The same is valid for the corresponding gradients $\frac{\partial}{\partial t} \Delta I_{z,r_1}^K$. In addition, we introduce the vector of single-difference measurements $\tilde{\Psi}(t_n)$ for every epoch t_n :

$$\tilde{\Psi}(t_n) = \begin{pmatrix} \lambda \tilde{\varphi}_{r_1}^{12}(t_n) \\ \vdots \\ \lambda \tilde{\varphi}_{r_1}^{1K}(t_n) \\ \tilde{\rho}_{r_1}^{12}(t_n) \\ \vdots \\ \tilde{\rho}_{r_1}^{1K}(t_n) \end{pmatrix} = \begin{pmatrix} \lambda \varphi_{r_1}^{12} + (\tilde{e}_{r_1}^{12})^T \hat{x}^{12} + c\delta\tau^{12} - \hat{T}_{r_1}^{12} + \hat{I}_{r_1}^{12} \\ \vdots \\ \lambda \varphi_{r_1}^{1K} + (\tilde{e}_{r_1}^{1K})^T \hat{x}^{1K} + c\delta\tau^{1K} - \hat{T}_{r_1}^{1K} + \hat{I}_{r_1}^{1K} \\ \rho_{r_1}^{12} + (\tilde{e}_{r_1}^{12})^T \hat{x}^{12} + c\delta\tau^{12} - \hat{T}_{r_1}^{12} - \hat{I}_{r_1}^{12} - b_{\text{DCB}}^{12} \\ \vdots \\ \rho_{r_1}^{1K} + (\tilde{e}_{r_1}^{1K})^T \hat{x}^{1K} + c\delta\tau^{1K} - \hat{T}_{r_1}^{1K} - \hat{I}_{r_1}^{1K} - b_{\text{DCB}}^{1K} \end{pmatrix} \quad (4.30)$$

However, the residual combined zenith ionospheric delays and gradients can be resolved only using the observations sufficiently spaced in time. The soft constraints are imposed on the residual combined zenith ionospheric delays and corresponding gradients by setting their standard deviations to prior values. This allows us to improve the conditioning and reduce the observation

time needed to estimate all unknown parameters. Therefore the system of equations (4.28) becomes:

$$\begin{pmatrix} \lambda \tilde{\varphi}_{r_1}^{12}(t_n) \\ \vdots \\ \lambda \tilde{\varphi}_{r_1}^{1K}(t_n) \\ \tilde{\rho}_{r_1}^{12}(t_n) \\ \vdots \\ \tilde{\rho}_{r_1}^{1K}(t_n) \\ 0 \\ 0 \end{pmatrix} = \begin{pmatrix} (\tilde{e}_{r_1}^{12}(t_n))^T \\ \vdots \\ (\tilde{e}_{r_1}^{1K}(t_n))^T \\ (\tilde{e}_{r_1}^{12}(t_n))^T \\ \vdots \\ (\tilde{e}_{r_1}^{1K}(t_n))^T \\ 0 \\ 0 \end{pmatrix} \vec{x}_{r_1} + \begin{pmatrix} \lambda \cdot 1 \\ 0 \\ 0 \\ 0 \end{pmatrix} \begin{pmatrix} N_{r_1}^{12} + \beta^{12} \\ \vdots \\ N_{r_1}^{1K} + \beta^{1K} \end{pmatrix} + \\
 \begin{pmatrix} M_{I,\varphi}(t_n) \\ M_{I,\rho}(t_n) \\ 1 \\ 0 \end{pmatrix} \begin{pmatrix} \Delta I_{z,r_1}^1(t_0) - \frac{m_1^2}{m_1^3} \Delta I_{z,r_1}^2(t_0) \\ \frac{m_1^2}{m_1^3} \Delta I_{z,r_1}^2(t_0) - \Delta I_{z,r_1}^3(t_0) \\ \vdots \\ \frac{m_1^2}{m_1^K} \Delta I_{z,r_1}^2(t_0) - \Delta I_{z,r_1}^K(t_0) \end{pmatrix} \\
 + \begin{pmatrix} \Delta t_n \cdot M_{I,\varphi}(t_n) \\ \Delta t_n \cdot M_{I,\rho}(t_n) \\ 0 \\ 1 \end{pmatrix} \begin{pmatrix} \frac{\partial}{\partial t} \Delta I_{z,r_1}^1 - \frac{m_1^2}{m_1^3} \cdot \frac{\partial}{\partial t} \Delta I_{z,r_1}^2 \\ \frac{m_1^2}{m_1^3} \cdot \frac{\partial}{\partial t} \Delta I_{z,r_1}^2 - \frac{\partial}{\partial t} \Delta I_{z,r_1}^3 \\ \vdots \\ \frac{m_1^2}{m_1^K} \cdot \frac{\partial}{\partial t} \Delta I_{z,r_1}^2 - \frac{\partial}{\partial t} \Delta I_{z,r_1}^K \end{pmatrix} + \begin{pmatrix} \epsilon_{r_1}^{12} \\ \vdots \\ \epsilon_{r_1}^{1K} \\ \eta_{r_1}^{12} \\ \vdots \\ \eta_{r_1}^{1K} \\ \epsilon_{I,r_1}^{12} \\ \vdots \\ \epsilon_{I,r_1}^{1K} \\ \epsilon_{I,r_1}^{12} \\ \vdots \\ \epsilon_{I,r_1}^{1K} \end{pmatrix}, \quad (4.31)$$

Introducing the vector single-difference measurements for all epochs $\tilde{\Psi}$, of ambiguities N and the mapping matrix A which maps the ambiguity to its measurement, residual combined zenith ionospheric delays ΔI at time t_0 and corresponding mapping matrix M_I , residual combined zenith ionospheric delay gradients $\Delta \dot{I}$ with mapping matrix $M_{\dot{I}}$, the geometry matrix H_{geo} as well as the

matrix of the measurement noise η we can further simplify the notation of Eq. (4.28) to

$$\tilde{\Psi} = H_{geo}\vec{x}_{r_1} + AN + M_I\Delta I + M_{\dot{I}}\Delta\dot{I} + \eta = H\xi + \eta, \quad (4.32)$$

where

$$\xi = \begin{pmatrix} \vec{x}_{r_1} \\ N \\ \Delta I \\ \Delta\dot{I} \end{pmatrix}, \quad H = \begin{pmatrix} H_{geo} & A & M_I & M_{\dot{I}} \end{pmatrix},$$

$$A = \begin{pmatrix} \lambda \cdot \mathbf{1}_{N_{ep} \times (K-1)} & \mathbf{0}_{N_{ep} \times (K-1)} & \mathbf{0}_{2 \cdot (K-1) \times (K-1)} \end{pmatrix}^T,$$

$$M_I = \begin{pmatrix} M_{I,\varphi} \mathbf{1}_{N_{ep} \times (K-1)} & M_{I,\rho} \mathbf{1}_{N_{ep} \times (K-1)} & \mathbf{1}_{(K-1) \times (K-1)} & \mathbf{0}_{(K-1) \times (K-1)} \end{pmatrix}^T,$$

$$M_{\dot{I}} = \begin{pmatrix} \Delta t \cdot M_{I,\varphi} \mathbf{1}_{N_{ep} \times (K-1)} & \Delta t \cdot M_{I,\rho} \mathbf{1}_{N_{ep} \times (K-1)} & \mathbf{0}_{(K-1) \times (K-1)} & \mathbf{1}_{(K-1) \times (K-1)} \end{pmatrix}^T$$

$$\eta \sim N(0, \Sigma_{\tilde{\Psi}}^{-1}),$$

where the weighting matrix $\Sigma_{\tilde{\Psi}}^{-1}$ that incorporates the knowledge about quality of our measurements into solution is computed as an inverse of the covariance matrix given by:

$$\Sigma_{\tilde{\Psi}}^{-1} = \begin{pmatrix} \Sigma_{sd,\varphi}(t_n) & 0 & 0 & 0 \\ 0 & \Sigma_{sd,\rho}(t_n) & 0 & 0 \\ 0 & 0 & \Sigma_I & 0 \\ 0 & 0 & 0 & \Sigma_{\dot{I}} \end{pmatrix}^{-1} \quad (4.33)$$

Estimation of 3-dimensional receiver position \vec{x}_{r_1} , single-difference ambiguities N , residual combined zenith ionospheric ΔI delays as well as gradients $\Delta\dot{I}$ was performed by the means of Kalman filter according to the Algorithm 2 using observations from multiple epochs in blocks of size $N_{ep, block}$. It is recursive least-squares estimator, which includes a prediction (state estimates noted by \hat{x}_n^-) and an update step (state estimates noted by \hat{x}_n^+) at each epoch. For the initialization of the Kalman filter (*Lines 3-4*) the over-determined system of equations (4.28) is solved in least-squares sense (see e.g. [4]), i.e.:

$$\hat{\xi} = \min_{\vec{x}_r, N, \Delta I, \Delta\dot{I}} \left\| \tilde{\Psi} - H\xi \right\|_{\Sigma_{\tilde{\Psi}}^{-1}}^2 \quad (4.34)$$

according to procedure described in the Algorithm 1.

The Algorithm 1 uses the iterative Gauss-Newton method which requires the initialization of unknown parameters. We initialize receiver position, ambiguities, residual combined zenith iono-

spheric delays and corresponding gradients with zeros (*Line 1* to *Line 4*). The number of epochs $N_{ep} = 300$ was chosen to allow the measurements to be sufficiently spaced in time in order to ensure a better resolution of all unknowns. In *Lines 8* and *9*, mapping functions for ionospheric zenith delays are calculated based on the estimated satellite elevation angles. The latter ones were obtained with the least-squares single-epoch float solution. Total tropospheric delay for each satellite is estimated in *Line 10* according to Eq. (4.18) - (4.26). Total ionospheric delay for each satellite is estimated in *Line 11* according to Klobuchar model [32]. The code and phase residuals defined as difference between measured and calculated pseudoranges are determined in *Line 12* and *Line 13*. The satellite-receiver unit-vectors are calculated in *Line 14*. Subsequently, single-difference code and phase residuals are calculated in *Line 19* and *Line 20* as the differences between code and phase residuals of reference satellite *1* and any other satellite *k*, as well as unknown parameters. The single-difference residuals of the residual combined zenith ionospheric delays and gradients are calculated in *Line 23* and *Line 24* assuming zero-value measurements. The calculated single-difference residuals are then stacked in a vector (*Line 26*). In the similar manner, in *Line 21* differential unit-vectors for the differential geometry matrix H_{geo} are determined. The residuals are then used to determine the receiver position, single-difference ambiguities, combined zenith ionospheric delays and gradients (*Line 27*).

The residuals of the least-squares multi-epoch float solution are presented in Fig. 4.5 for code measurements and Fig. 4.6 for phase measurements. The data set was collected at 11 a.m., that corresponds to the rather active ionosphere. However, the increased number of satellites help us to efficiently solve for all parameters in a reduced time period. The code residuals are in the order of ± 2 m, that is accurate enough for initialization of Kalman filter and its faster convergence.

Algorithm 1 Iterative least-squares float multi-epoch solution**Input:** $\rho(t)$, $\varphi(t)$, $\vec{x}^k(t)$, $\delta\tau^k(t)$, $\theta^k(t)$, W , DOY , $\lambda \quad \forall k, \forall t$ **Output:** \vec{x}_{r_1} , N , ΔI , $\Delta \dot{I}$

- 1: $\vec{x}_{r_1}^{(0)} = 0_{3 \times 1}$ ▷ Initialization of unknowns
- 2: $N^{(0)} = 0_{(K-1) \times 1}$
- 3: $\Delta I^{(0)} = 0_{(K-1) \times 1}$
- 4: $\Delta \dot{I}^{(0)} = 0_{(K-1) \times 1}$

- 5: **for** $i = 1 \rightarrow 5$ **do** ▷ Newton iterations

- 6: **for** $t = 1 \rightarrow N_{\text{ep}}$ **do**
- 7: **for** $k = 1 \rightarrow K$ **do**
- 8: $\zeta^k(t) = \theta^k(t) - 90^\circ$ ▷ Calculation of mapping functions of zenith ionospheric delays
- 9: $m_I^k(t) = \frac{1}{\sqrt{1 - \frac{\sin^2 \zeta^k(t)}{(1+h/R_e)^2}}}$
- 10: $\hat{T}_{r_1}^{k,(i)}(t) = \hat{T}_{z,dry}^k(t)m_{dry}^k(t) + \hat{T}_{z,wet}^k(t)m_{wet}^k(t)$ ▷ Estimation of tropospheric delays
- 11: Estimation of slant ionospheric delays $\hat{I}_{r_1}^{k,(i)}(t)$ with Klobuchar model ▷ Calculation of code and phase residuals
- 12: $r_{r_1,\rho}^{k,(i)}(t) = \rho_{r_1}^k(t) - \|\hat{x}^k(t) - \hat{x}_{r_1}^{(i-1)}\| + c\delta\tau^k - \hat{T}_{r_1}^{k,(i)}(t) - \hat{I}_{r_1}^{k,(i)}(t) - b_{\text{DCB}}^k$
- 13: $r_{r_1,\varphi}^k(t) = \varphi_{r_1}^k(t) - \|\hat{x}^k(t) - \hat{x}_{r_1}^{(i-1)}\| + c\delta\tau^k - \hat{T}_{r_1}^{k,(i)}(t) + \hat{I}_{r_1}^{k,(i)}(t)$
- 14: $\vec{e}_{r_1}^{k,(i)}(t) = \frac{\hat{x}_{r_1}^{(i-1)} - \hat{x}^k(t)}{\|\hat{x}_{r_1}^{(i-1)} - \hat{x}^k(t)\|}$ ▷ Calculation of satellite-receiver unit-vectors
- 15: **end for**
- 16: **end for**

- 17: **for** $t = 1 \rightarrow N_{\text{ep}}$ **do**
- 18: **for** $k = 1 \rightarrow (K - 1)$ **do** ▷ Calculation of SD code and phase residuals
- 19: $r_{r_1,\rho}^{1k,(i)}(t) = r_{r_1,\rho}^{1,(i)}(t) - r_{r_1,\rho}^{k,(i)}(t) - M_{I,\rho}^{2k}(t)\Delta \hat{I}_{r_1}^{k,(i)} - M_{I,\rho}^{2k}(t)\Delta \hat{I}_{r_1}^{k,(i)}$
- 20: $r_{r_1,\varphi}^{1k,(i)}(t) = r_{r_1,\varphi}^{1,(i)}(t) - r_{r_1,\varphi}^{k,(i)}(t) - M_{I,\varphi}^{2k}(t)\Delta \hat{I}_{r_1}^{k,(i)} - M_{I,\varphi}^{2k}(t)\Delta \hat{I}_{r_1}^{k,(i)} - \lambda N^{1k,(i)}$
- 21: $\vec{e}_{r_1}^{1k,(i)}(t) = \vec{e}_{r_1}^{1,(i)}(t) - \vec{e}_{r_1}^{k,(i)}(t)$ ▷ Calculation of differential unit-vectors
- 22: **end for** ▷ Calculation of SD residual combined zenith ionospheric delays and gradients residuals
- 23: $r_{r_1,I}^{1k,(i)} = 0 - \Delta \hat{I}_{r_1}^{k,(i)}$
- 24: $r_{r_1,\dot{I}}^{1k,(i)} = 0 - \Delta \dot{\hat{I}}_{r_1}^{k,(i)}$
- 25: **end for**

- 26: $r_{\text{sd}}^{(i)} = \left(r_{r_1,\rho}^{1k,(i)}(t) \mid r_{r_1,\varphi}^{1k,(i)}(t) \mid r_{r_1,I}^{1k,(i)} \mid r_{r_1,\dot{I}}^{1k,(i)} \right)^T \quad \forall t, \forall k \in (1 : K - 1)$ ▷ Residuals vector

- 27:
$$\begin{pmatrix} \hat{x}_{r_1}^{(i)} \\ \hat{N}_{r_1}^{(i)} \\ \Delta \hat{I}_{r_1}^{(i)} \\ \Delta \dot{\hat{I}}_{r_1}^{(i)} \end{pmatrix} = \begin{pmatrix} \hat{x}_{r_1}^{(i-1)} \\ \hat{N}_{r_1}^{(i-1)} \\ \Delta \hat{I}_{r_1}^{(i-1)} \\ \Delta \dot{\hat{I}}_{r_1}^{(i-1)} \end{pmatrix} + (H^T \Sigma_{\vec{\psi}}^{-1} H)^{-1} H^T \Sigma_{\vec{\psi}}^{-1} r_{\text{sd}}^{(i)}$$
- 28: **end for**

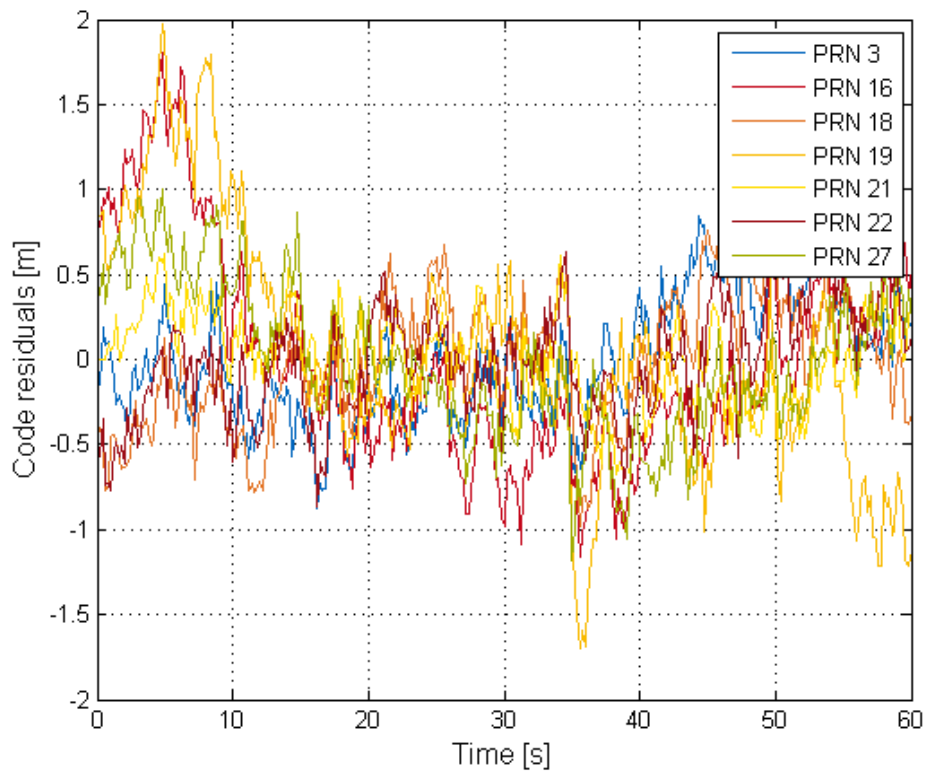


Figure 4.5: Code residuals of floating least-squares estimation according to Alg. 1

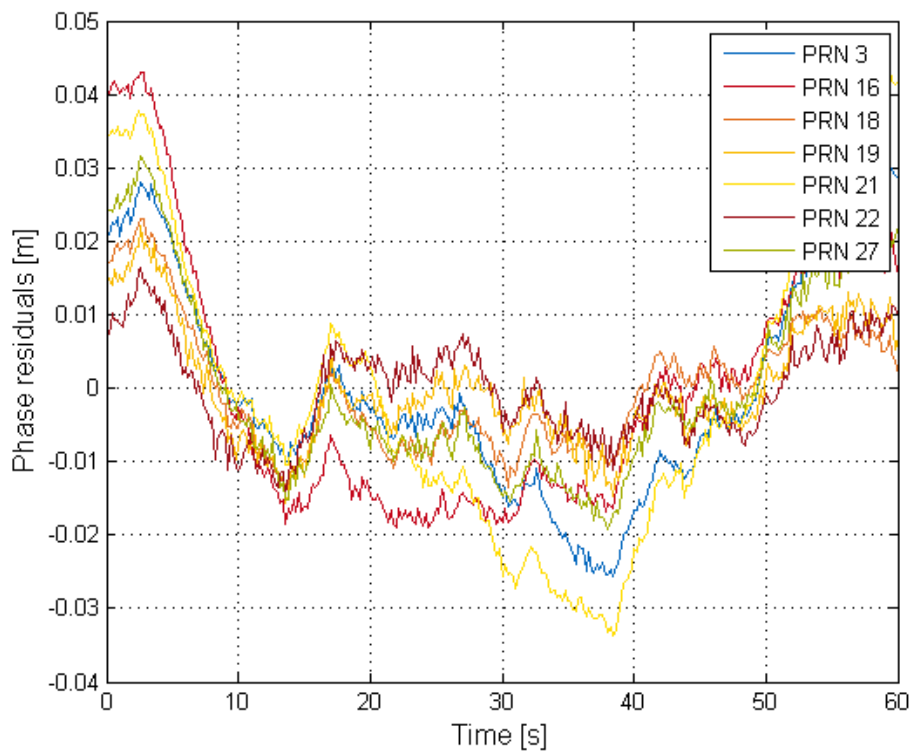


Figure 4.6: Phase residuals of floating least-squares estimation according to Alg. 1

After the initialization phase of the Algorithm 2, in *Lines 6-7* the prediction of the state estimates \hat{x}_n^- based on the state space model is calculated together with its covariance matrix ([5]). Once the measurements of all block are available, they are corrected by the estimated tropospheric and ionospheric zenith delays (*Lines 10-12*) and the single-difference code and phase measurements are computed in *Line 20* according to Eq. (2.3) and Eq. (2.5). In *Line 21* the differential unit-vectors are computed for the geometry matrix H_{geo} In the way described in Algorithm 1. The predicted state estimate is updated using these measurements to get \hat{x}_n^+ in *Lines 25-27*. The covariance matrix of observation noise R_n is computed according to the model in (4.33). The procedure is repeated till the convergence of estimates is achieved. The size of measurement block $N_{ep, block}$ was chosen as a trade-off between accuracy of estimates and the time needed to receive the next state estimate, which is important for a real-time system.

Assuming the last estimate provided by Kalman filter as reference, the errors of the estimates of receiver coordinates were calculated for three values of the standard deviation of the residual combined zenith ionospheric delays $\sigma_{\Delta I} = 10$ m, 1 m and 0.1 m (Fig. 4.7-4.9). Given that the temporal variation of the ionospheric delay is 10 cm/min on the average [33], the standard deviation for gradients $\sigma_{\frac{\partial}{\partial t} \Delta I} = 0.001$ m was chosen. Analyzing the convergence behavior of the receiver coordinates, $\sigma_{\Delta I} = 1$ m was used for further analysis. The corresponding estimates of receiver coordinates are presented in Fig. 4.10-4.12. The standard deviations of estimates were computed over the periods 20 min and depicted in the form of error bars (two standard deviations). For all coordinates they decrease with time, indicating the convergence. Y coordinate converges in 15 min to the error of less than 30 cm, X coordinate of around 60 cm, and Z coordinate of around 3 m. The ambiguities of 4 highest elevation satellites converges to the error of less than 1 cycle in 70 min (Fig. 4.13). However, they still cannot be fixed to the floating values due to uncorrected satellite biases.

Algorithm 2 Estimation of 3-D receiver position, ambiguities, residual combined zenith ionospheric delays and gradients with Kalman filter

Input: $\rho(t), \varphi(t), \vec{x}^k(t), \delta\tau^k(t), \theta^k(t), W, DOY, \lambda \quad \forall k, \forall t$

Output: $\vec{x}_{r_1}, N, \Delta I, \Delta \dot{I}$

```

1: for  $n = 1 \rightarrow N_{\text{blocks}}$  do
2:   if  $n = 1$  then
3:      $\hat{x}_n^+ = \left( \vec{x}_{r_1, n} \ N_n \ \Delta I_n \ \Delta \dot{I}_n \right)^T$   $\triangleright$  Initialization of apriori information according to Alg. 1
4:      $P_{\hat{x}_n^+} = (H^T \Sigma_{\vec{y}}^{-1} H)^{-1}$ 

5:   else
6:      $\hat{x}_n^- = \Phi_{n-1} \hat{x}_{n-1}^+$ 
7:      $P_{\hat{x}_n^-} = \Phi_{n-1} P_{\hat{x}_{n-1}^+} \Phi_{n-1}^T + Q_n$   $\triangleright$  Computation of the state prediction and its covariance matrix

8:   for  $t = 1 \rightarrow N_{\text{ep, block}}$  do
9:     for  $k = 1 \rightarrow K$  do
10:      Calculation of mapping functions of zenith ionospheric delays  $m_{I,n}^k(t)$ 
11:      Estimation of tropospheric delays  $\hat{T}_{r_1, n}^k(t)$ 
12:      Estimation of slant ionospheric delays with Klobuchar model  $\hat{I}_{r_1, n}^k(t)$ 
13:       $\vec{e}_n^k(t) = \frac{\hat{x}_{r_1, n}^- - \hat{x}^k(t)}{\|\hat{x}_{r_1, n}^- - \hat{x}^k(t)\|}$   $\triangleright$  Calculation of satellite-receiver unit-vectors
14:       $\tilde{\rho}_{r_1, n}^k(t) = \rho_{r_1}^k(t) - \vec{e}_n^k(t) \hat{x}^k(t) + c\delta\tau^k - \hat{T}_{r_1, n}^k(t) - \hat{I}_{r_1, n}^k(t) - b_{\text{DCB}}^k$ 
15:       $\tilde{\varphi}_{r_1, n}^k(t) = \varphi_{r_1}^k(t) - \vec{e}_n^k(t) \hat{x}^k(t) + c\delta\tau^k - \hat{T}_{r_1, n}^k(t) + \hat{I}_{r_1, n}^k(t)$ 
16:    end for
17:  end for

18:  for  $t = 1 \rightarrow N_{\text{ep, block}}$  do
19:    for  $k = 1 \rightarrow (K - 1)$  do
20:      Calculation of SD corrected code  $\tilde{\rho}_{r_1, n}^{1k}(t)$  and phase  $\tilde{\varphi}_{r_1, n}^{1k}(t)$  measurement
21:      Calculation of differential unit-vectors  $\vec{e}_{r_1, n}^{1k}(t)$ 
22:    end for
23:  end for

24:   $z_{\text{sd}, n} = \left( \varphi_{r_1, n}^{1k}(t) \mid \rho_{r_1, n}^{1k}(t) \mid 0_{2 \cdot (K-1) \times 1} \right)^T \quad \forall t \in (1 : N_{\text{ep, block}}), \forall k \in (1 : K - 1)$   $\triangleright$  Observation vector

25:   $K_n = P_{\hat{x}_n^-} H_n^T (H_n P_{\hat{x}_n^-} H_n^T + R_n)^{-1}$   $\triangleright$  Calculation of Kalman gain
26:   $\hat{x}_n^+ = \hat{x}_n^- + K(z_n - H_n \hat{x}_n^-)$ 
27:   $P_{\hat{x}_n^+} = (1 - K_n H_n) P_{\hat{x}_n^-}$   $\triangleright$  Calculation of the state update and covariance matrix

28: end if
29: end for

```

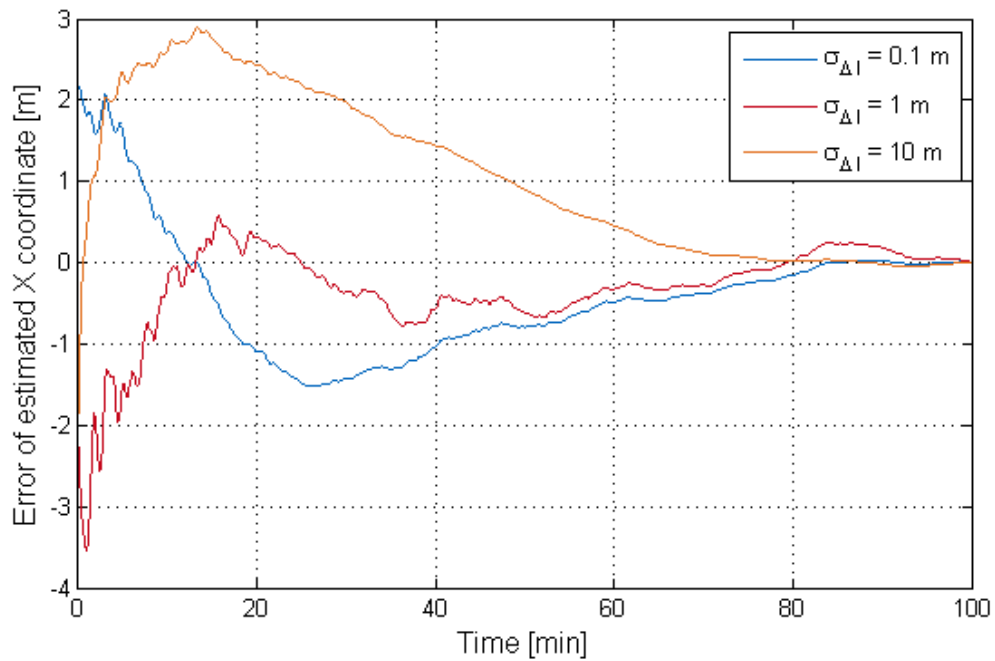


Figure 4.7: Error of the estimate of receiver X coordinate for different $\sigma_{\Delta I}$

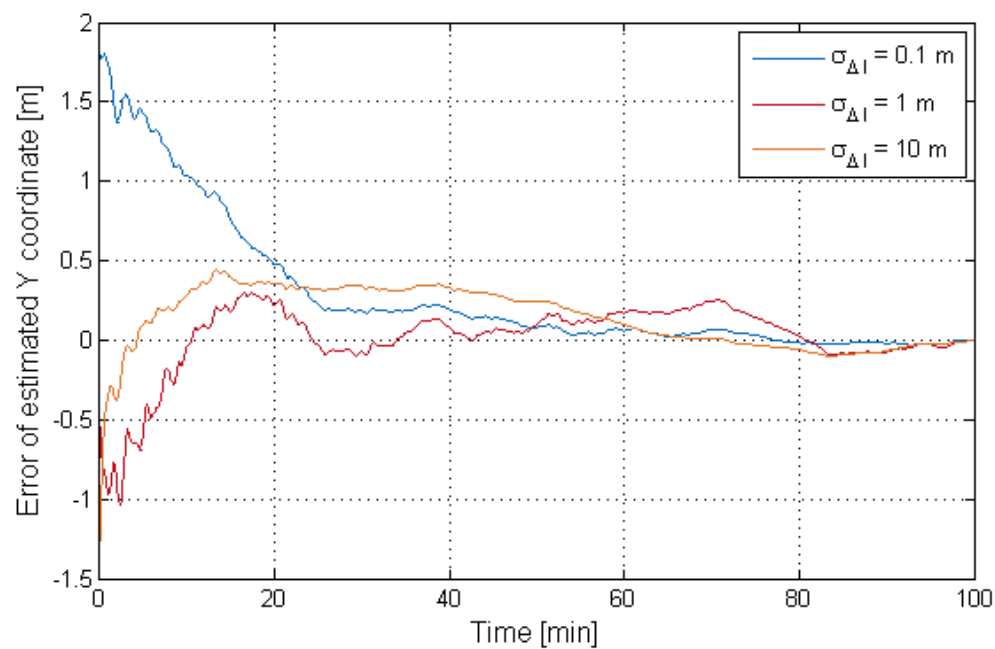


Figure 4.8: Error of the estimate of receiver Y coordinate for different $\sigma_{\Delta I}$

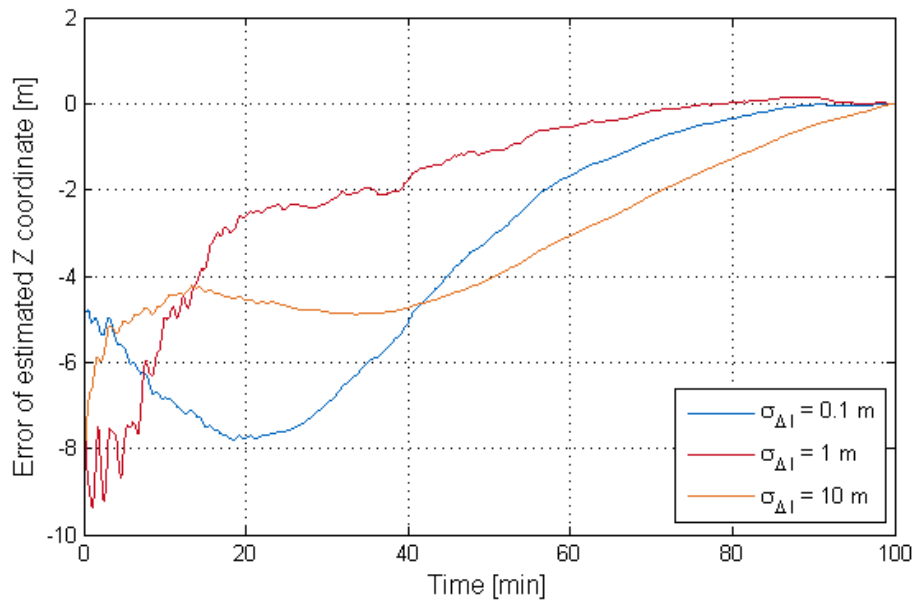


Figure 4.9: Error of the estimate of receiver Z coordinate for different $\sigma_{\Delta I}$

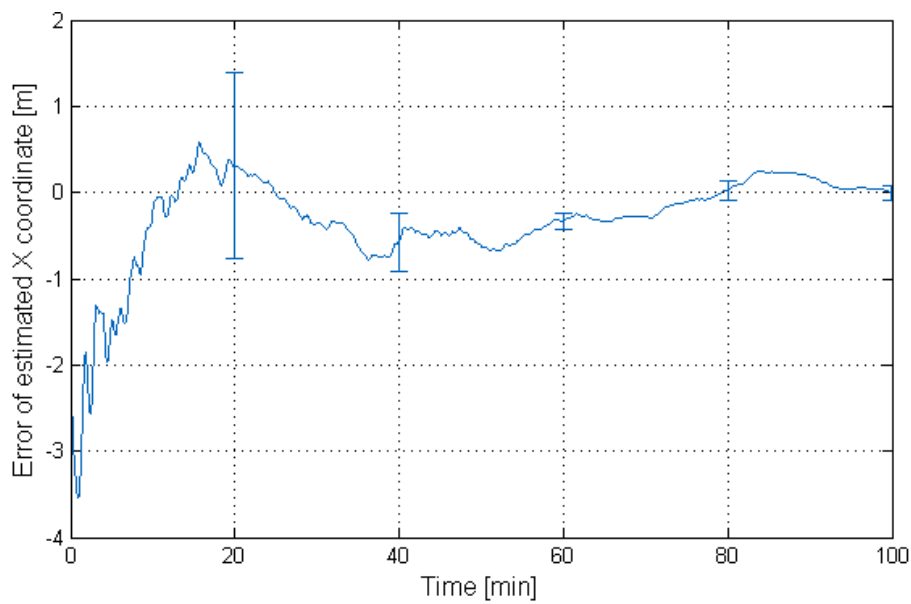


Figure 4.10: Error of the estimate of receiver X coordinate assuming $\sigma_{\Delta I} = 1$ m

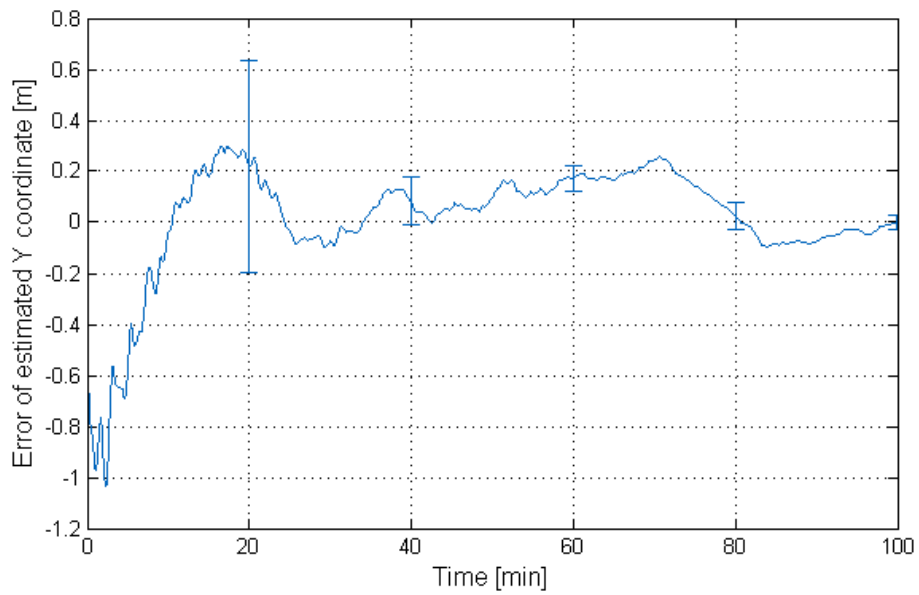


Figure 4.11: Error of the estimate of receiver Y coordinate assuming $\sigma_{\Delta I}=1$ m

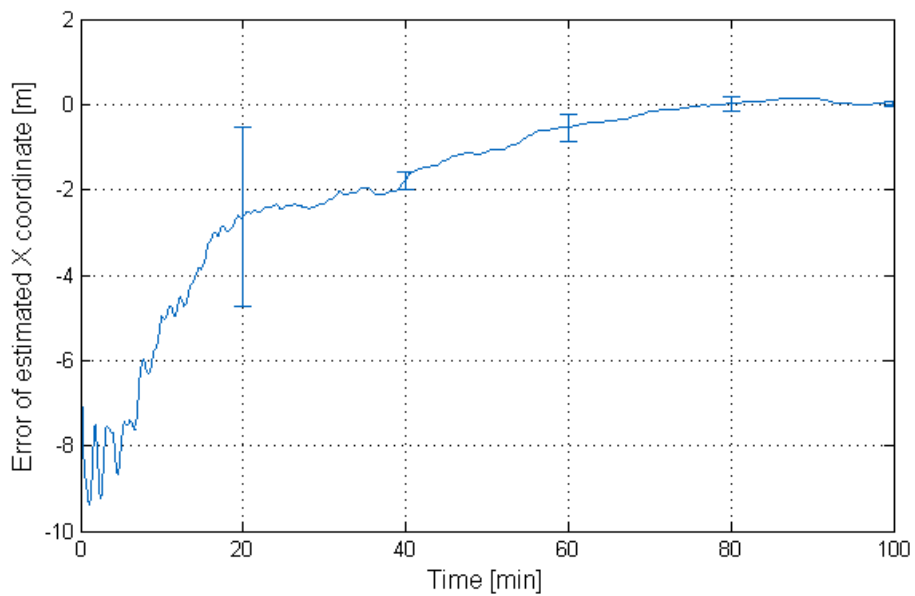


Figure 4.12: Error of the estimate of receiver Z coordinate assuming $\sigma_{\Delta I}=1$ m

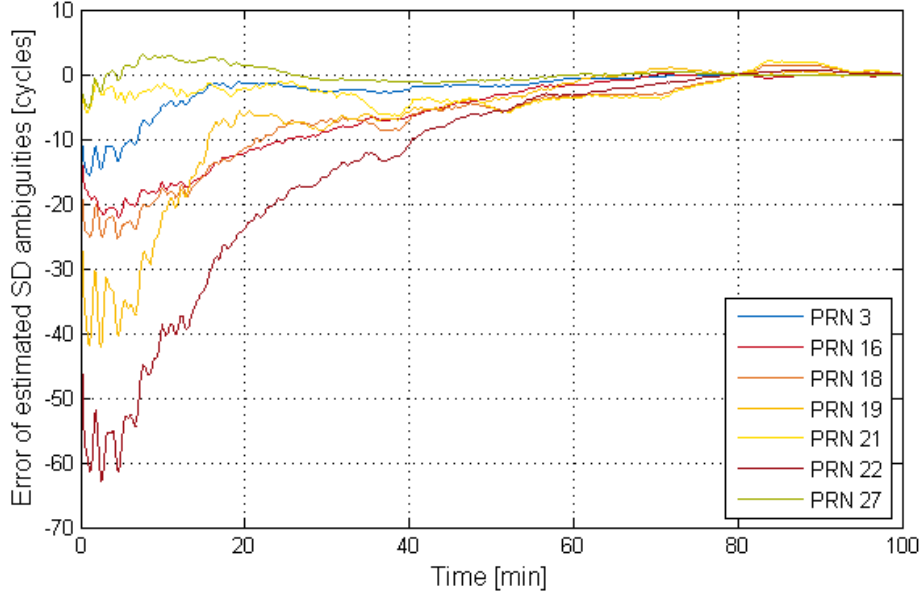


Figure 4.13: Error of the estimate of single-difference ambiguities assuming $\sigma_{\Delta I}=1$ m

4.3 Corrections for single-difference code and phase measurements

Once absolute position of the first reference receiver r_1 is determined, the sum of errors in form of correction for single-difference carrier phase measurements between reference satellite l and any other satellite k at the reference receiver r_1 is calculated as follows [34]:

$$\begin{aligned}
 c_{r_1, \varphi}^{1k}(t) &= \varphi_{r_1}^{1k}(t) - \left(\vec{e}_{r_1}^1(t)(\hat{\vec{x}}_{r_1} - \hat{\vec{x}}^1(t)) - (\vec{e}_{r_1}^k(t)(\hat{\vec{x}}_{r_1}(t) - \hat{\vec{x}}^k(t))) \right) + c\delta\hat{\tau}^{1k}(t) \\
 &= \vec{e}_{r_1}^1(t)(\delta\vec{x}_{r_1} - \delta\vec{x}^1(t)) - \vec{e}_{r_1}^k(t)(\delta\vec{x}_{r_1}(t) - \delta\vec{x}^k(t)) \\
 &\quad - I_{r_1}^{1k}(t) + T_{r_1}^{1k}(t) + \lambda N_{r_1}^{1k} + \beta_{\varphi}^{1k}(t) + \varepsilon_{r_1}^{1k}(t)
 \end{aligned} \tag{4.35}$$

with single-difference carrier phase measurements $\varphi_{r_1}^{1k}$ of the reference receiver r_1 determined according to Eq. (2.5), unit-vector $\vec{e}_{r_1}^1(t)$ pointing from satellite l to reference receiver r_1 , estimation of absolute position $\hat{\vec{x}}_{r_1}$ of reference receiver r_1 , estimation of absolute position $\hat{\vec{x}}^1$ of satellite l , speed of light c , estimation of clock offsets difference $\delta\hat{\tau}^{1k}$ between satellites l and k , error of estimation of absolute position $\delta\vec{x}_{r_1}$ of reference receiver r_1 , error of estimation of absolute position $\delta\vec{x}^1$ of satellite l , difference of ionospheric delays $I_{r_1}^{1k}$ between satellites l and k in the direction of reference receiver r_1 , difference of tropospheric delays $T_{r_1}^{1k}$ between satellites l and k in the direction of reference receiver r_1 , wavelength λ , carrier phase ambiguities difference $N_{r_1}^{1k}$ between satellites l and k , difference of phase biases β_{φ}^{1k} between satellites l and k and difference of phase noise and multipath errors $\varepsilon_{r_1}^{1k}$ between satellites l and k at the reference receiver r_1 .

The correction for single-difference code measurements between reference satellite l and any other satellite k at the reference receiver r_1 is given by:

$$\begin{aligned} c_{r_1,\rho}^{1k}(t) &= \rho_{r_1}^1(t) - \left((\vec{e}_{r_1}^1(t))^T (\hat{\vec{x}}_{r_1} - \hat{\vec{x}}^1(t)) - (\vec{e}_{r_1}^k(t))^T (\hat{\vec{x}}_{r_1}(t) - \hat{\vec{x}}^k(t)) \right) + c\delta\hat{\tau}^{1k}(t) \\ &= (\vec{e}_{r_1}^1(t))^T (\delta\vec{x}_{r_1} - \delta\vec{x}^1(t)) - (\vec{e}_{r_1}^k(t))^T (\delta\vec{x}_{r_1}(t) - \delta\vec{x}^k(t)) \\ &\quad + I_{r_1}^{1k}(t) + T_{r_1}^{1k}(t) + \beta_\rho^{1k}(t) + \eta_{r_1}^{1k}(t) \end{aligned} \quad (4.36)$$

with single-difference code measurements $\varphi_{r_1}^{1k}$ of the reference receiver r_1 determined according to Eq. (2.3), difference of code biases β_ρ^{1k} between satellites l and k and difference of code noise and multipath errors $\eta_{r_1}^{1k}$ between satellites l and k at the reference receiver r_1 as additional terms.

The absolute position of reference receiver r_2 is represented as a function of estimated absolute position of reference receiver r_1 and a priori baseline vector:

$$\hat{\vec{x}}_{r_2} = \hat{\vec{x}}_{r_1} - \hat{\vec{b}}_{r_1,r_2} \quad (4.37)$$

The same applies to single-difference carrier phase ambiguities between satellites l and k at the reference receiver r_2 , which can be represented as a function of single-difference carrier phase ambiguities between the same satellites at the reference receiver r_1 and a priori double-difference phase ambiguities:

$$\hat{N}_{r_2}^{1k} = \hat{N}_{r_1}^{1k} - \hat{N}_{r_1,r_2}^{1k} \quad (4.38)$$

A priori baseline vector $\hat{\vec{b}}_{r_1,r_2}$ and double-difference ambiguities \hat{N}_{r_1,r_2}^{1k} were determined according to the following algorithm:

- Computation of the double-difference code and phase measurements over at least 800 epochs;
- Determination of the floating least-squares solution for the baseline vector components and double-difference ambiguities;
- Integer phase ambiguity search with the unconstrained LAMBDA method of Teunissen ([20] and [19]);
- Fixing of the double-difference phase ambiguities and computation of fixed least-squares solution for the baseline vector components.

Taking into account Eq. (4.37) and Eq. (4.38), the correction for single-difference carrier phase measurements $\varphi_{r_2}^{1k}$ at the reference receiver r_2 is given by [34]:

$$\begin{aligned} c_{r_2,\varphi}^{1k}(t) &= \varphi_{r_2}^{1k}(t) - \left(\vec{e}_{r_2}^1(t) (\hat{\vec{x}}_{r_2}(t) - \hat{\vec{x}}^1(t)) - \vec{e}_{r_2}^k(t) (\hat{\vec{x}}_{r_2}(t) - \hat{\vec{x}}^k(t)) \right) + c\delta\hat{\tau}^{1k}(t) + \lambda\tilde{N}_{r_1r_2}^{1k} \\ &= \vec{e}_{r_2}^1(t) (\delta\vec{x}_{r_1}(t) - \delta\vec{x}^1(t)) - \vec{e}_{r_2}^k(t) (\delta\vec{x}_{r_1}(t) - \delta\vec{x}^k(t)) \\ &\quad - I_{r_2}^{1k}(t) + T_{r_2}^{1k}(t) + \lambda N_{r_1}^{1k} + \beta_\varphi^{kl}(t) + \varepsilon_{r_2}^{1k}(t) \end{aligned} \quad (4.39)$$

The single-difference carrier phase corrections $c_{r_1,\varphi}(t)$ and $c_{r_2,\varphi}(t)$ show common location-independent offsets $\lambda N_{r_1}^{1k}$ and $\beta_\varphi^{1k}(t)$. It allows us to be able to estimate the double-difference integer ambiguities between reference receiver r_1 and user receiver as the final user receiver positioning step.

In the similar manner, the single-difference code correction is calculated, i.e.

$$\begin{aligned} c_{r_2,\rho}^{1k}(t) &= \rho_{r_2}^{1k}(t) - \left(\vec{e}_{r_2}^1(t)(\hat{x}_{r_2}(t) - \hat{x}^1(t)) - \vec{e}_{r_2}^k(t)(\hat{x}_{r_2}(t) - \hat{x}^k(t)) \right) + c\delta\hat{\tau}^{1k}(t) \\ &= \vec{e}_{r_2}^1(t)(\delta\vec{x}_{r_1}(t) - \delta\vec{x}^1(t)) - \vec{e}_{r_2}^k(t)(\delta\vec{x}_{r_1}(t) - \delta\vec{x}^k(t)) \\ &\quad - I_{r_2}^{1k}(t) + T_{r_2}^{1k}(t) + \beta_\rho^{kl}(t) + \varepsilon_{r_2}^{1k}(t) \end{aligned} \quad (4.40)$$

The single-difference code corrections $c_{r_1,\rho}(t)$ and $c_{r_2,\rho}(t)$ show common location-independent offset $\beta_\rho^{1k}(t)$.

The single-difference code and phase corrections calculated over the period of 30 min. from the observations of the receiver r_1 are presented in Fig. 4.14 and Fig. 4.15. Only the measurements from the satellites with elevation over 20° are used as the ones less affected by cycle slips. The corrections were calculated provided precise orbits from IGS to reduce the impact of orbital error. For the plotting of phase correction, that includes single-difference ambiguities, the initial value was subtracted to better see short-term variations. The code correction reaches as much as 20 m for low elevation satellite (PRN 19). Due to the short baseline the code correction of the reference receiver r_2 is very similar in magnitude to corrections of r_1 , while phase correction is only different by the integer number of cycles. Both show similar behavior over time.

Thus single-difference code and carrier phase corrections contain in addition to errors of satellite and reference receiver positions estimation, as well as differences of atmospheric delays, the location-independent errors. Therefore single-difference corrections for any location with latitude ϕ_r and longitude λ_r at the epoch t_n can be modeled as:

$$\begin{aligned} c_r^{1k}(\phi_r, \lambda_r, t_n) &= c_0^{1k}(t_0) + \frac{\partial}{\partial t} c_0^{1k} \cdot (t_n - t_0) + \left(\frac{\partial}{\partial \lambda} c^{1k}(t_0) + \frac{\partial^2}{\partial t \partial \lambda} c^{1k} \cdot (t_n - t_0) \right) \cdot (\lambda_r - \lambda_0) \\ &\quad + \left(\frac{\partial}{\partial \phi} c^{1k}(t_0) + \frac{\partial^2}{\partial t \partial \phi} c^{1k} \cdot (t_n - t_0) \right) \cdot (\phi_r - \phi_0) \end{aligned} \quad (4.41)$$

where $c_0^{1k}(t_0)$ is the offset from the location with longitude λ_0 and latitude ϕ_0 at the time t_0 , $\frac{\partial}{\partial \lambda} c^{1k}(t_0)$ and $\frac{\partial}{\partial \phi} c^{1k}(t_0)$ are the spatial gradients at the time t_0 , $\frac{\partial}{\partial t} c_0^{1k}$ is the time gradient of the offset, $\frac{\partial^2}{\partial t \partial \lambda} c^{1k}$ and $\frac{\partial^2}{\partial t \partial \phi} c^{1k}$ are the time gradients of the corresponding spatial gradients. Having the measurements from three or more reference receivers over multiple epochs, the offset and the gradients can be resolved.

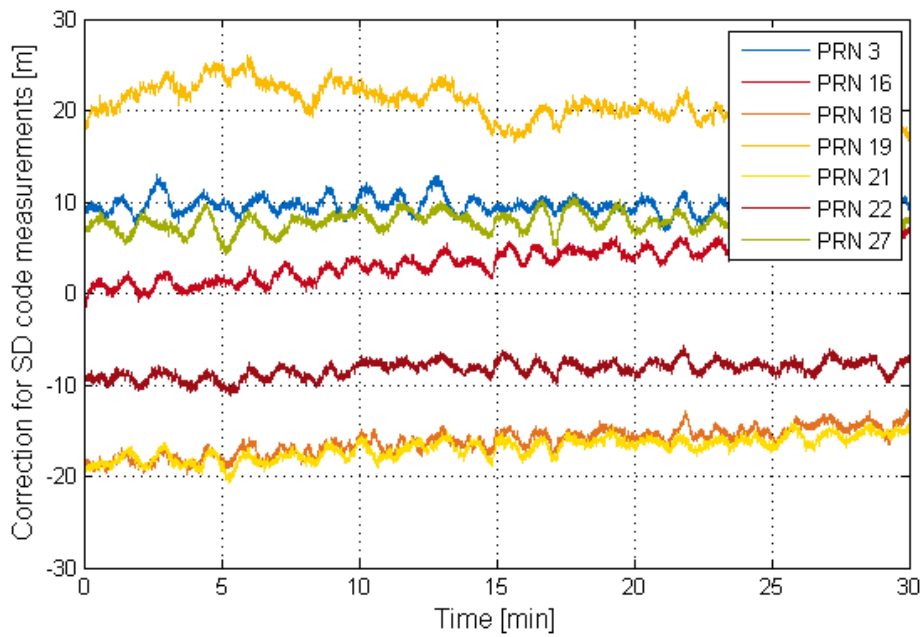


Figure 4.14: Correction for single-difference code measurements

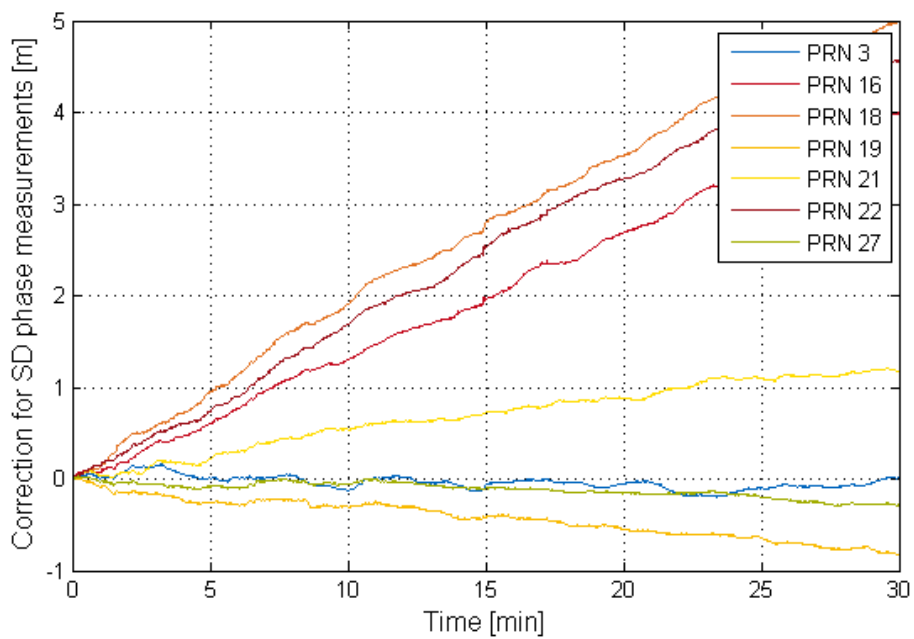


Figure 4.15: Correction for single-difference phase measurements

Single-difference corrections from N multiple epochs for R reference receivers can be written in the matrix notation as:

$$\underbrace{\begin{pmatrix} c_{r_1}^{1k}(\lambda_{r_1}, \phi_{r_1}, t_0) \\ \vdots \\ c_{r_R}^{1k}(\lambda_{r_R}, \phi_{r_R}, t_0) \\ \vdots \\ c_{r_1}^{1k}(\lambda_{r_1}, \phi_{r_1}, t_n) \\ \vdots \\ c_{r_R}^{1k}(\lambda_{r_R}, \phi_{r_R}, t_n) \\ \vdots \\ c_{r_1}^{1k}(\lambda_{r_1}, \phi_{r_1}, t_N) \\ \vdots \\ c_{r_R}^{1k}(\lambda_{r_R}, \phi_{r_R}, t_N) \end{pmatrix}}_{\tilde{\Psi}} = \underbrace{\begin{pmatrix} \tilde{H} & (t_0 - t_0)\tilde{H} \\ \vdots & \vdots \\ \tilde{H} & (t_n - t_0)\tilde{H} \\ \vdots & \vdots \\ \tilde{H} & (t_N - t_0)\tilde{H} \end{pmatrix}}_{\tilde{H}_{geo}} \begin{pmatrix} c_0^{1k}(t_0) \\ \frac{\partial}{\partial \lambda} c^{1k}(t_0) \\ \frac{\partial}{\partial \phi} c^{1k}(t_0) \\ \frac{\partial}{\partial t} c_0^{1k} \\ \frac{\partial^2}{\partial t \partial \lambda} c^{1k} \\ \frac{\partial^2}{\partial t \partial \phi} c^{1k} \end{pmatrix} + \begin{pmatrix} \eta_{r_1}^{1k}(t_0) \\ \vdots \\ \eta_{r_R}^{1k}(t_0) \\ \vdots \\ \eta_{r_1}^{1k}(t_n) \\ \vdots \\ \eta_{r_R}^{1k}(t_n) \\ \vdots \\ \eta_{r_1}^{1k}(t_N) \\ \vdots \\ \eta_{r_R}^{1k}(t_N) \end{pmatrix} \quad (4.42)$$

where the geometry matrix \tilde{H}_{geo} is given by:

$$\tilde{H}_{geo} = \begin{pmatrix} 1 & \lambda_{r_1} - \lambda_0 & \phi_{r_1} - \phi_0 \\ \vdots & \vdots & \vdots \\ 1 & \lambda_{r_R} - \lambda_0 & \phi_{r_R} - \phi_0 \end{pmatrix} \quad (4.43)$$

The offset and spatial gradients, as well as corresponding time gradients, are resolved by using least-squares method:

$$\begin{pmatrix} c_0^{1k}(t_0) \\ \frac{\partial}{\partial \lambda} c^{1k}(t_0) \\ \frac{\partial}{\partial \phi} c^{1k}(t_0) \\ \frac{\partial}{\partial t} c_0^{1k} \\ \frac{\partial^2}{\partial t \partial \lambda} c^{1k} \\ \frac{\partial^2}{\partial t \partial \phi} c^{1k} \end{pmatrix} = (\tilde{H}_{geo}^T W \tilde{H}_{geo})^{-1} \tilde{H}_{geo}^T W \tilde{\Psi} \quad (4.44)$$

For the short baselines, it can be assumed that $\lambda_{r_R} \approx \lambda_{r_0}$ and $\phi_{r_R} \approx \phi_{r_0}$. Thus Eq. (4.42) and Eq. (4.44) can be simplified as follows:

$$\underbrace{\begin{pmatrix} c_{r_1}^{1k}(\lambda_{r_1}, \phi_{r_1}, t_0) \\ \vdots \\ c_{r_R}^{1k}(\lambda_{r_R}, \phi_{r_R}, t_0) \\ \vdots \\ c_{r_1}^{1k}(\lambda_{r_1}, \phi_{r_1}, t_n) \\ \vdots \\ c_{r_R}^{1k}(\lambda_{r_R}, \phi_{r_R}, t_n) \\ \vdots \\ c_{r_1}^{1k}(\lambda_{r_1}, \phi_{r_1}, t_N) \\ \vdots \\ c_{r_R}^{1k}(\lambda_{r_R}, \phi_{r_R}, t_N) \end{pmatrix}}_{\tilde{\Psi}} = \underbrace{\begin{pmatrix} 1 & (t_0 - t_0) \\ \vdots & \vdots \\ 1 & (t_0 - t_0) \\ \vdots & \vdots \\ 1 & (t_n - t_0) \\ \vdots & \vdots \\ 1 & (t_n - t_0) \\ \vdots & \vdots \\ 1 & (t_N - t_0) \\ \vdots & \vdots \\ 1 & (t_N - t_0) \end{pmatrix}}_{\tilde{H}_{geo}} \left(\begin{pmatrix} c_0^{1k}(t_0) \\ \frac{\partial}{\partial t} c_0^{1k} \end{pmatrix} \right) + \begin{pmatrix} \eta_{r_1}^{1k}(t_0) \\ \vdots \\ \eta_{r_R}^{1k}(t_0) \\ \vdots \\ \eta_{r_1}^{1k}(t_n) \\ \vdots \\ \eta_{r_R}^{1k}(t_n) \\ \vdots \\ \eta_{r_1}^{1k}(t_N) \\ \vdots \\ \eta_{r_R}^{1k}(t_N) \end{pmatrix} \quad (4.45)$$

$$\begin{pmatrix} c_0^{1k}(t_0) \\ \frac{\partial}{\partial t} c_0^{1k} \end{pmatrix} = (\tilde{H}_{geo}^T W \tilde{H}_{geo})^{-1} \tilde{H}_{geo}^T W \tilde{\Psi} \quad (4.46)$$

On the short baselines, at least two reference receivers are necessary to perform interpolation. For the weighting matrix W , the identity matrix was used, as all corrections are given with comparable accuracies. The interpolated code and carrier phase corrections are presented in Fig. 4.16 and Fig. 4.17.

4.4 Estimation of absolute position of a user receiver

The values of the gradients and offsets shall be used to correct single-difference code and carrier phase measurements, and consequently determine the absolute position of the user receiver. First single-difference code and carrier phase measurements between satellites l and k at the user receiver r_u shall be computed according to Eq. (2.3) and Eq. (2.5). Then, the single-difference carrier phase corrections shall be interpolated to the position of rover r_u determined with the least-squares

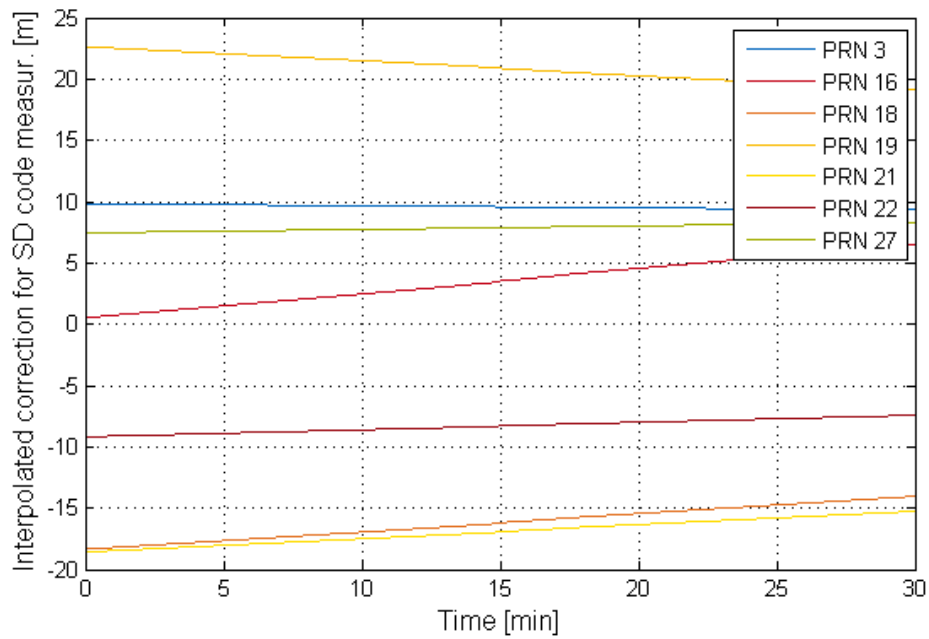


Figure 4.16: Interpolated correction for single-difference code measurements

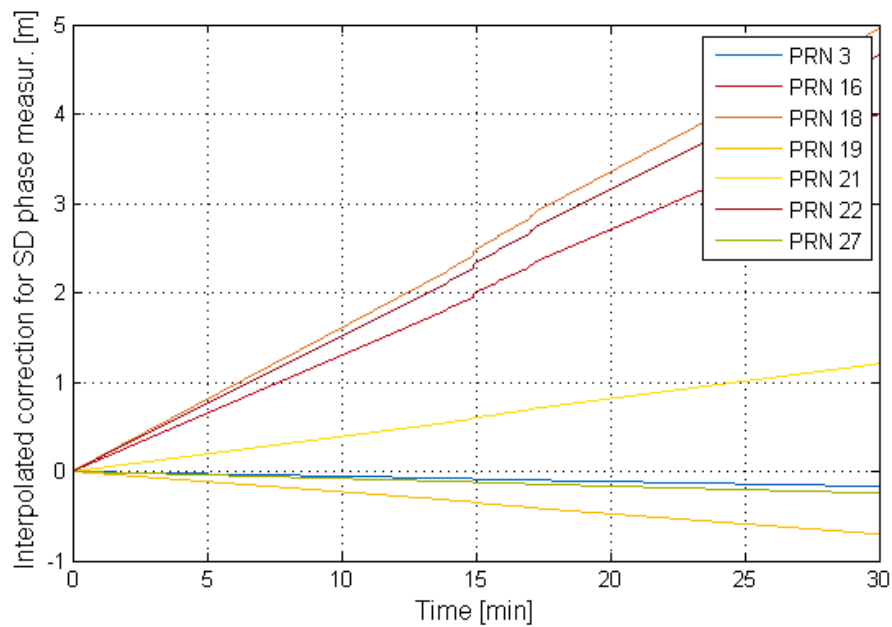


Figure 4.17: Interpolated correction for single-difference phase measurements

method. Finally, the corrections shall be applied as follows:

$$\begin{aligned}
\lambda \hat{\varphi}_u^{1k}(t) &= \lambda \varphi_u^{1k}(t) - c_{u,\varphi}^{1k}(\lambda_u, \phi_u, t) \\
&= \lambda \varphi_u^{1k}(t) - \hat{c}_{\lambda,\phi}^{1k}(t) \lambda_u(t) - \hat{c}_{\phi,\varphi}^{1k}(t) \phi_u(t) \\
&\approx (\bar{e}_u^1(t)(\vec{x}_u(t) - \vec{x}^1(t)) + c\delta\hat{\tau}^{1k}(t) + \lambda \underbrace{(N_u^{1k} - N_{r_1}^{1k})}_{N_{u,r_1}^{1k}}) + \varepsilon_{u,r_1}^{1k}(t) \quad (4.47)
\end{aligned}$$

For the code we obtain in the similar way:

$$\begin{aligned}
\hat{\rho}_u^{1k}(t) &= \rho_u^{1k}(t) - c_{u,\rho}^{1k}(\lambda_u, \phi_u, t) \\
&= \rho_u^{1k}(t) - \hat{c}_{\lambda,\rho}^{1k}(t) \lambda_u(t) - \hat{c}_{\phi,\rho}^{1k}(t) \phi_u(t) \\
&\approx (\bar{e}_u^1(t)(\vec{x}_u(t) - \vec{x}^1(t)) + c\delta\hat{\tau}^{1k}(t) + \eta_{u,r_1}^{1k}(t) \quad (4.48)
\end{aligned}$$

From the corrected code and carrier phase measurements the absolute position of the user receiver $\hat{\vec{x}}_u(t)$ and double- difference carrier phase ambiguities N_{u,r_1}^{1k} shall be determined by the Sequential Best Integer-Equivariant Estimator [35]. Best Integer-Equivariant estimation method minimizes the mean square error and is in this sense better than the widely used LAMBDA method. However, it implies a complex ambiguity search and therefore comparatively rarely used.

5. Conclusions

In this thesis, the capability of the Galileo system for precise relative and absolute positioning was evaluated. In addition, the Virtual Reference Station concept for a network of low-cost receivers was developed.

For the precise positioning with single- and multi-frequency receivers, errors such as code tracking error as well as multipath remain the main limiting factors. However, the Galileo system will provide the signals to overcome these shortcomings, as it was demonstrated in Chapter 3 by processing the Galileo and GPS data with a few positioning algorithms. The code noise of Galileo E5 signal was found to be in the range of 2 cm. The considerable improvement of the reliability of widelane integer ambiguity resolution with the classical LAMBDA method was demonstrated. The ratio of the squared measurement residuals reaches values of 100 for Galileo. Moreover, the higher stability of the Galileo float ambiguity estimates in long-range RTK was demonstrated. In addition, the improved accuracy of Galileo-based PPP was shown in terms of the fixed phase residuals of an order of 1 cm compared to 4 cm of GPS. Once the Galileo system is fully operational, more test campaigns involving a number of static, as well as dynamic receivers can be carried out to evaluate its performance not only jointly, but also fully independent of GPS.

The Virtual Reference Station method, used in differential positioning to increase the distance between user receiver and reference station without loss of final positioning accuracy, was adapted for the system of low-cost GPS receivers in Chapter 4. The precise positioning of the reference receiver, necessary to derive corrections, was successfully performed with decimeter level accuracy using a Kalman filter. To improve the conditioning and convergence of the estimates, the ionospheric a priori information was added as a Gaussian distribution. The relative positioning of the second reference receiver was performed with the classical unconstrained LAMBDA method of Teunissen. Knowing the positions, the combined errors were determined from the single-difference code and phase measurements of both receivers and interpolated according to the model described. The algorithm of the user receiver position calculation using the derived corrections was proposed. For the final validation of the developed absolute positioning concept based on corrected raw measurements, the short and long-baseline test campaigns involving at least three static receivers as well as a user receiver (static and dynamic) shall be carried out.

List of Abbreviations

AltBOC	Alternate BOC modulation, constant envelope modulation scheme for combining two Galileo signals E5a and E5b in order to generate broadband E5 signal
ANAVS	Advanced Navigation Solutions - ANAVS GmbH
BOC	Binary Offset Carrier modulation
BPSK	Binary Phasen Shift Keying modulation
CBOC	Composite Binary Offset Carrier modulation
CDMA	Code Division Multiple Access
CODE	Center for Orbit Determination in Europe
DD	Double-difference
DCB	Differential Code Bias
DGPS	Differential GPS
DOY	Day-of-a-year
ECEF	Earth-Centered, Earth-Fixed coordinate frame
EGNOS	European Geostationary Navigation Overlay Service
ENU	East-North-Up coordinate frame
ESA	European Space Agency
GPS	Global Positioning System
IF	Ionosphere-free
IGS	International GNSS Service
LAMBDA	Least-squares AMBiguity Decorrelation Adjustment
MEO	Medium Earth Orbit
MOPS	Minimum Operational Performance Standards
NL	Narrowlane
OS	Open Service
PAD	Position and Attitude Determination
PPP	Precise Point Positioning

PRS	Public Regulated Service
RTK	Real-Time Kinematic
SD	Single-difference
SoL	Safety of Life
SSE	Sum of Squared Errors
TUM	Technische Universität München
VRS	Virtual Reference Station
WAAS	Wide Area Augmentation System
WL	Widelane

List of Figures

3.1	Static short-baseline test set-up. Crosses mark the positions of the test receivers . . .	13
3.2	Skyplot Roof Laboratory of the Institute for Communications and Navigation of TUM	13
3.3	Double-difference E1 Galileo code measurements	18
3.4	Double-difference E5 Galileo code measurements	18
3.5	Error norm ratio of integer LAMBDA search	19
3.6	Phase residuals of E1-E5 constrained fixed solution	20
3.7	Mobile long-baseline test set-up	21
3.8	Skyplot Roof Laboratory of the Institute for Communications and Navigation of TUM	21
3.9	GPS L1-L2 double-difference widelane ambiguities	22
3.10	Galileo E1-E5 double-difference widelane ambiguities	23
3.11	Residuals of integer-fixed E1-E5 widelane code-carrier combination	25
3.12	Residuals of real-fixed E1-E5 narrowlane phase-only combination	25
3.13	GPS fixed phase residuals with ambiguities averaged over all epochs	27
3.14	GPS fixed phase residuals with ambiguities averaged over last 200 epochs	27
3.15	Galileo fixed phase residuals with ambiguities averaged over last 200 epochs	28
3.16	Probability of a wrong fixing over all subsets	30
3.17	Probability of a wrong subset selection for two types of search	32
3.18	Galileo IF ambiguities and biases	32
3.19	Maximum bias change within 5 min	33
3.20	Maximum bias change within 1 min	33
3.21	Maximum bias change within 1 sec	34
4.1	Virtual Reference Station set-up [3]	36
4.2	Interpolation and extrapolation of the differential residuals [24]	38
4.3	Comparison of different models for the tropospheric delay [25]	42
4.4	Geometry of ionospheric propagation [7]	46
4.5	Code residuals of floating least-squares estimation according to Alg. 1	52
4.6	Phase residuals of floating least-squares estimation according to Alg. 1	52
4.7	Error of the estimate of receiver X coordinate for different $\sigma_{\Delta I}$	55
4.8	Error of the estimate of receiver Y coordinate for different $\sigma_{\Delta I}$	55

4.9	Error of the estimate of receiver Z coordinate for different $\sigma_{\Delta I}$	56
4.10	Error of the estimate of receiver X coordinate assuming $\sigma_{\Delta I}=1$ m	56
4.11	Error of the estimate of receiver Y coordinate assuming $\sigma_{\Delta I}=1$ m	57
4.12	Error of the estimate of receiver Z coordinate assuming $\sigma_{\Delta I}=1$ m	57
4.13	Error of the estimate of single-difference ambiguities assuming $\sigma_{\Delta I}=1$ m	58
4.14	Correction for single-difference code measurements	61
4.15	Correction for single-difference phase measurements	61
4.16	Interpolated correction for single-difference code measurements	64
4.17	Interpolated correction for single-difference phase measurements	64

List of Tables

3.1	Innovations of Galileo [2]	11
3.2	Galileo carrier signals [1]	12

Bibliography

- [1] European Union, *European GNSS (Galileo) Open Service Signal In Space Interface Control Document*, 1.1 ed., September 2010.
- [2] P. Henkel, *Reliable Carrier Phase Positioning*. Dissertation, Technische Universität München, July 2010.
- [3] U. Vollath, A. Deking, H. Landau, and C. Pagels, “Long-Range RTK Positioning Using Virtual Reference Stations,” in *Proceedings of the International Symposium on Kinematic Systems in Geodesy, Geomatics and Navigation, Banf, Canada*, June 2001.
- [4] P. Misra and P. Enge, *Global Positioning System: Signals, Measurements and Performance*. Ganga-Jamuna Press, 2nd ed., 2006.
- [5] P. Henkel, “Lecture notes for Precise Point Positioning with GPS and Galileo.” Technische Universität München, 2013.
- [6] P. Heroux and J. Kouba, “GPS precise point positioning using IGS orbit products,” *Physics and Chemistry of the Earth, Part A: Solid Earth and Geodesy*, vol. 26, no. 6-8, pp. 573–578, 2001.
- [7] C. Günther, “Lecture notes for Satellite Navigation.” Technische Universität München, 2013.
- [8] W. G. Melbourne, “The Case for Ranging in GPS Based Geodetic Systems,” in *Proceedings 1st International Symposium on Precise Positioning with the Global Positioning System*, pp. 373–386, U.S. Department of Commerce, April 1985.
- [9] G. Wübbena, “Software Developments for Geodetic Positioning with GPS Using TI 4100 Code and Carrier Measurements,” in *Proceedings 1st International Symposium on Precise Positioning with the Global Positioning System*, pp. 403–412, U.S. Department of Commerce, April 1985.
- [10] P. Henkel and C. Günther, “Reliable carrier phase positioning with multi-frequency code carrier linear combinations,” in *Proceedings of 23rd ION International Technical Meeting*, pp. 185–195, US Institute of Navigation, Sep 2010.
- [11] P. Henkel and C. Günther, “Reliable Integer Ambiguity Resolution with Multi-Frequency Code Carrier Linear Combinations,” *Journal of Global Positioning Systems*, vol. 9, no. 2, pp. 90–103, 2010.

-
- [12] P. Henkel and C. Günther, “Reliable Integer Ambiguity Resolution: Multi-Frequency Code Carrier Linear Combinations and Statistical A Priori Knowledge of Attitude,” *Navigation, Journal of the Institute of Navigation*, vol. 59, pp. 61–75, Spring 2012.
- [13] G. Hein, J. Godet, J. Issler, J. Martin, P. Erhard, R. Lucas-Rodriguez, and T. Pratt, “Status of Galileo frequency and signal design,” in *Proceedings of ION GPS*, 2002.
- [14] M. Falcone, E. B. S. Binda, E. S. J. Hahn, G. L. R. F. Gonzalez, R. S. P. Giordano, and A. H. G. Galluzzo, “Galileo on its own first position fix,” *Inside GNSS*, pp. 51–53, March/April 2013.
- [15] J. Avila-Rodriguez, G. Hein, S. Wallner, J. Issler, L. Ries, L. Lestarquit, A. de Latour, J. Godet, F. Bastide, T. Pratt, and J. Owen, “The MBOC Modulation: The Final Touch to the Galileo Frequency and Signal Plan,” *Navigation, Journal of the Institute of Navigation*, pp. 14–28, 2008.
- [16] G. A. McGraw, T. Murphy, M. Brenner, S. Pullen, and A. J. V. Dierendonck, “Development of the LAAS Accuracy Models,” in *Proceedings of ION GNSS 2000, Salt Lake City, UT, USA*, pp. 1212–1223, September 2000.
- [17] J. J. Kiam, “Low-cost GPS-based Compass with Reliable Ambiguity Resolution and Cycle Slip Correction,” Master’s thesis, Technische Universität München, March 2013.
- [18] P. Henkel, J. Cardenas, G. Giorgi, and C. Günther, “Precise Attitude Determination with Low-cost Satellite Navigation Receivers,” in *Submitted for publication in IEEE Transactions on Vehicular Technology*, 2013.
- [19] P. J. G. Teunissen, “Integer least-squares theory for the GNSS compass,” *Journal of Geodesy*, pp. 433–447, July 2010.
- [20] P. J. G. Teunissen, “GNSS Integer Ambiguity Validation: Overview of Theory and Methods,” in *Proceedings of the Institute of Navigation Pacific PNT 2013, Honolulu, Hawaii*, April 2013.
- [21] D. Laurichesse, F. Mercier, J. Berthias, P. Broca, and L. Cerri, “Integer ambiguity resolution on undifferenced GPS phase measurements and its application to PPP and satellite precise orbit determination,” *Navigation, Journal of the Institute of Navigation*, vol. 56, September 2009.
- [22] P. J. G. Teunissen, “The least-squares ambiguity decorrelation adjustment: a method for fast GPS ambiguity estimation,” *Journal of Geodesy*, pp. 65–82, 1995.
- [23] H. Landau, U. Vollath, and X. Chen, “Virtual Reference Station Systems,” *Journal of Global Positioning Systems*, pp. 137–143, 2002.
- [24] U. Vollath, A. Buecherl, H. Landau, C. Pagels, and B. Wagner, “Multi-Base RTK Positioning Using Virtual Reference Stations,” in *Proceedings of ION GPS 2000, Salt Lake City, Utah*,

- USA, pp. 123–131, September 2000.
- [25] A. Hornbostel and M. Hoque, “Analysis of Tropospheric Correction Models for Local Events within the GSTB Test Case APAF,” in *Proceedings of ION GNSS 2004, Long Beach, CA, USA*, pp. 902–914, September 2004.
- [26] Radio Technical Commission for Aeronautics (RTCA), *Minimum Operational Performance Standards for Global Positioning System/Wide Area Augmentation System Airborne Equipment*, DO-229D ed., December 2006.
- [27] T. Schüler, G. W. Hein, and B. Eissfeller, “A New Tropospheric Correction Model for GNSS Navigation,” in *Proceedings of V GNSS International Symposium, Spanish Institute of Navigation, Seville, Spain*, May 2001.
- [28] S. Katsougiannopoulos, C. Pikridas, D. Rossikopoulos, I. Ifadis, and A. Fotiou, “Tropospheric Refraction Estimation Using Various Models, Radiosonde Measurements and Permanent GPS Data,” in *Proceedings of XXIII FIG Congress, Munich, Germany*, October 2006.
- [29] J. Marini, “Correction of Satellite Tracking Data for an Arbitrary Tropospheric Profile,” *Radio Science*, pp. 223–231, February 1972.
- [30] T. A. Herring, “Modelling atmospheric delays in the analysis of space geodetic data,” in *Proceedings of the Symposium on Refraction of Transatmospheric Signals in Geodesy*, pp. 157–164, May 1992.
- [31] A. Niell, “Global mapping functions for the atmosphere delay at radio wavelengths,” *Journal of Geophysical Research*, pp. 3227–3246, February 1996.
- [32] J. Klobuchar, “Ionospheric Time-Delay Algorithms for Single-Frequency GPS Users,” *IEEE Transactions on Aerospace and Electronic Systems*, vol. AES-23(3), pp. 325–331, 1987.
- [33] P. H. Doherty, P. J. Gendron, R. Loh, and D. N. Anderson, “The Spatial and Temporal Variations in Ionospheric Range Delay,” in *Proceedings of ION GPS 1997, Kansas City, Missouri, USA*, pp. 231–240, September 1997.
- [34] P. Henkel, “Zuverlässige Navigation für die Binnenschifffahrt. Detaillierte Vorhabensbeschreibung zum Förderantrag bei der bayerischen Forschungsstiftung.” September 2013.
- [35] A. Brack, P. Henkel, and C. Günther, “Sequential Best Integer-Equivariant Estimation for Geodetic Network Solutions,” in *Proceedings of ION GNSS 2013, San Diego, California, USA*, pp. 310–317, January 2013.